UNIVERSIDAD DE CHILE

FACULTAD DE CIENCIAS FÍSICAS Y MATEMÁTICAS

DEPARTAMENTO DE GEOLOGÍA

GEOQUÍMICA DE METALES PRECIOSOS Y METALOIDES EN DEPÓSITOS DE SÍNTER SILÍCEO: IMPLICANCIAS EN LA INCORPORACIÓN DE ELEMENTOS A FASES SILÍCEAS.

TESIS PARA OPTAR AL GRADO DE MAGÍSTER EN CIENCIAS, MENCIÓN GEOLOGÍA
MEMORIA PARA OPTAR AL TÍTULO DE GEÓLOGO

CAMILO EMMANUEL SÁNCHEZ YÁÑEZ

PROFESOR GUÍA

MARTIN REICH MORALES

MIEMBROS DE LA COMISIÓN

DIEGO MORATA CÉSPEDES

FERNANDO BARRA PANTOJA

SANTIAGO DE CHILE

2016

Resumen de la memoria para optar al título de: Geólogo y grado de Magíster en Ciencias, mención geología.
Por: Camilo Sánchez Yáñez
Fecha: Julio 2016
Profesor guía: Martin Reich

"Geoquímica de metales preciosos y metaloides en depósitos de sínter silíceo: Implicancias en la incorporación de elementos a fases silíceas"

Los depósitos de sínter silíceo están compuestos por rocas sedimentarias químicas ricas en sílice, formadas por el sobre enfriamiento de un fluido alcalino clorurado de pH neutro. Su ocurrencia está asociada a zonas de *up-flow* de sistemas geotermales y a los niveles superficiales de depósitos epitermales de oro-plata de baja sulfuración. En el sínter se reconocen diferentes grados de cristalinidad de la sílice, junto con variados minerales accesorios que co-precipitan a partir del fluido hidrotermal. Además, especies metálicas pueden ser incorporadas a la matriz silícea. A pesar de que se han registrado concentraciones geoquímicas anómalas en el sínter, la relación entre los grados de cristalinidad de la sílice y los enriquecimientos/empobrecimientos en metales preciosos y metaloides no ha sido bien estudiada. Para estudiar la posible relación entre las fases silíceas y las concentraciones de especies metálicas a nivel traza, se investigó el depósito de sínter del campo geotermal de Puchuldiza en el Altiplano del norte de Chile, el cual presenta concentraciones metálicas en el fluido hidrotermal y en los depósitos de sínter y paleo sínter (asociado a fuentes termales inactivas).

En esta investigación se combinaron análisis de difracción de rayos X, de microscopía electrónica de barrido (SEM) y de espectrometría de masas por plasma inductivamente acoplado utilizando ablación láser (LA-ICP-MS), para determinar los grados de cristalinidad y minerales accesorios, definir las micro-morfologías de cada fase de sílice y cuantificar la geoquímica en cada fase; respectivamente.

En el depósito de sínter de Puchuldiza se reconoce una secuencia diagenética completa para las fases de sílice (ópalo A, ópalo A/CT, ópalo CT y cuarzo), entre fases amorfas hasta micro cristales de cuarzo, con valores del *Full Width at Half Maximum* (FWHM) variables entre 9.52-0.11 º2Θ. Las fases amorfas exhiben morfologías formadas por micro esferas de sílice de 1 a 6 μm, con superficies lisas y concentraciones promedio de Au de 0.23 ppm, Ag 0.74 ppm, As 133-10809 ppm y B 328-3015 ppm; las fases intermedias presentan micro esferas de superficies rugosas-hojosas de 5 a 20 μm con concentraciones promedio de Au de 13.47 ppm, Ag 46 ppm, As 274 ppm y B 65.6 ppm. Finalmente, las fases cristalinas se caracterizan morfológicamente por micro cristales de cuarzo sin orientación, con concentraciones promedio de 22 ppm de Au, 46 ppm de Ag, 11.2-28.4 ppm de As y 58 ppm de B.

El grado de cristalinidad de las fases silíceas presenta una marcada correlación con el enriquecimiento en metales, las fases amorfas están enriquecidas en metaloides y las fases cristalinas en metales preciosos. Factores deposicionales durante la formación del sínter como la aglomeración de nano-micro esferas de sílice y la co-precipitación de minerales accesorios favorecerían la incorporación de especies metálicas a las fases amorfas. Posteriormente, factores post deposicionales como los cambios morfo-cristalográficos de las fases de sílice promoverían la incorporación de metales preciosos como oro y plata, y su aglomeración en fases maduras; por lo que la transición diagenética de la sílice se considera preponderante en el tipo de enriquecimiento de metales en depósitos de sínter silíceo.

El bajo orden cristalográfico de la fase amorfa de ópalo A en el sínter de Puchuldiza coincide con los valores previamente publicados para El Tatio. Esta característica sería una propiedad común de los sínter emplazados en el Altiplano, producto de la posible influencia ambiental en la precipitación de sílice y de la incorporación de especies metálicas a nano escala.

Agradecimientos

Este trabajo plasma en parte la contribución de muchas personas, de las más diversas áreas, las que directa o indirectamente han participado en su gestación, desarrollo y finalización. Es por esto, que a las primeras personas que deseo reconocer son a mis padres que siempre creyeron en mí y me inculcaron que la mejor herramienta de progreso personal es el conocimiento, a mi hermano quien ha sido siempre quien me ilumina el camino con el ejemplo, y a mi abuelita (Adriana) que creyó que lo mejor que se puede transmitir es la enseñanza.

Además, quiero agradecer el inmenso apoyo del proyecto CONICYT-FONDAP 15090013, Centro de Excelencia en Geotermia de los Andes (CEGA) por haber financiado íntegramente el desarrollo de mi investigación de postgrado tanto en terrenos, análisis y beca. También, agradezco la contribución del proyecto Núcleo Milenio NC 130065 Trazadores de Metales en Zonas de Subducción, por financiar mi estadía en diversos congresos a nivel nacional e internacional.

Hago un especial reconocimiento a los responsables de los laboratorios en donde se realizaron los análisis micro-morfológicos, de difracción de rayos X, de geoquímica de aguas y de geoquímica de las muestras de sínter. Verónica Rodríguez encargada del laboratorio de geoquímica de fluidos del CEGA, quien siempre tuvo la disposición y voluntad de contribuir y apoyar el proceso de aprendizaje y la generación de datos, a Christian Nievas encargado del laboratorio de microscopía electrónica de barrido del departamento de Geología de la Universidad de Chile, a Andrés Ibáñez responsable del laboratorio de difracción de rayos X del departamento de física, y a Mathieu Leisen, investigador del laboratorio de espectrometría de masas – CEGA, del departamento de Geología de la Universidad de Chile; por involucrarse de lleno en esta investigación.

Agradezco especialmente a mi profesor guía Martin Reich, por haber confiado en mí para llevar a cabo varias investigaciones desde pregrado hasta esta investigación en postgrado, dando sus certeras contribuciones en los momentos en que más lo necesité. Además, agradezco a los profesores Diego Morata y Fernando Barra por sus aportes y críticas en el desarrollo de la publicación de esta investigación. También, al grupo de estudiantes de Martin, especialmente a Daniele Tardani, Pablo Sánchez, Fernanda Álvarez, Vladimir Vicencio y Laura Lagos, con quienes compartí en el plano profesional y personal, quienes con su ayuda, comentarios y preguntas aportaron al avance de este trabajo el cual no sería el mismo sin ellos. A los investigadores Mathieu Leisen y Lucy McGee quienes tuvieron la paciencia y disposición de compartir sus experiencias en el desarrollo de investigaciones, especialmente a Lucy que siempre estuvo dispuesta a solucionar miles de dudas de inglés. También, a mis compañeros de pregrado (Leo, Alones, Nico, Manu), de la oficina de postgrado, muy afectuosamente a Gruna, Boyce, Tardani y Angello quienes podrían ser co-autores de este trabajo; y a quienes trabajaron en las campañas de terreno a Puchuldiza: Exequiel Varela, Bernardita Alvear y Daniele.

Para Finalizar, deseo hacer un sentido reconocimiento a Alexandra Elbakyan por su infinita contribución al desarrollo científico, promoviendo el acceso democrático al conocimiento interdisciplinario generado a nivel mundial. Además, agradezco en lo más profundo a Claudia *negrucha* Cuevas por su inconmensurable apoyo emocional y material, dándome palabras de ánimos y sueños, junto a su mano cariñosa.

Tabla de contenido

Índice de figuras

Índice de tablas

CAPÍTULO 1

INTRODUCCIÓN

1.1 Estructura de la Tesis

En esta investigación se estudiaron las características mineralógicas, micro-morfológicas y geoquímicas de diversas muestras de paleo-sínter y sínter asociadas a fuentes hidrotermales activas del campo geotermal de Puchuldiza, en el Altiplano del norte de Chile. Además, se cotejaron las principales características del depósito con otros depósitos de sínter previamente reportados en la literatura científica.

En el capítulo 2 de este trabajo se presentan las principales características geológicas del lugar, con la recopilación de los últimos trabajos que discuten la litológica, estratigráfica y características estructurales de Puchuldiza y sus alrededores. Además, se presenta una caracterización geoquímica de las aguas termales analizadas durante esta investigación.

El manuscrito sometido a la revista *Geochimica et Cosmochimica Acta,* se presenta íntegramente en el capítulo 3. Finalmente, las principales conclusiones del trabajo se exponen en el capítulo 4.

1.2 Motivación

Los depósitos de sínter silíceo son rocas sedimentarias químicas ricas en sílice formadas por procesos de precipitación, principalmente abióticos, gatillados por el sobre enfriamiento en superficie de un fluido hidrotermal alcalino clorurado de pH neutro (Fournier and Rowe, 1966; Rodgers et al., 2004; Lynne et al., 2007). Estos depósitos se consideran expresiones superficiales de sistemas geotermales profundos y de sistemas epitermales de oro-plata de baja sulfuración; y han sido considerados marcadores paleo ambientales (Parker and Nicholson, 1990; Rodgers et al., 2004; Lynne et al., 2007; Lynne et al., 2008; Sillitoe, 2015).

Al formarse estos depósitos, la sílice precipita adoptando diversos grados de cristalinidad o fases silíceas, cada una con morfologías características. Inicialmente precipita como una fase amorfa de ópalo A, para re-ordenase estructuralmente y formar las fases para-cristalinas ópalo CT y ópalo C, y finalmente formar microcristales de cuarzo (Lynne et al., 2007). Estas variaciones estructurales son promovidas por cambios termodinámicos durante la transición diagenética de la sílice (Rodgers et al., 2004; Lynne et al., 2007). Junto con la precipitación de sílice, co-precipitan diversos minerales accesorios desde el fluido hidrotermal, los que se alojan en el sinter. Además, se han reportado contenidos variables de Au, Ag, Ti, B, Li, Hg, As, Sb, Pb entre otros metales, que se han asociado a la matríz silícea en el sinter y a minerales accesorios (Ichikuni, 1970; Parker and Nicholson, 1990; Saunders, 1990; McKenzie et al., 2001; Guido et al., 2002; Guidry and Chafetz, 2003; Pope and Brown, 2014; Sillitoe, 2015).

A pesar de que se reconoce ampliamente la diversidad cristalográfica en las fases de sílice y la gran presencia de especies metálicas que pueden incorporarse en los depósitos de sínter, la especiación de metales y su relación con los diversos grados de cristalinidad de la sílice no se ha constreñido adecuadamente. Particularmente, se desconoce la relación entre el grado de cristalinidad y la presencia o concentración de metales y metaloides. Es por esto que en esta investigación se pretenden responder las siguientes preguntas científicas: ¿existen variaciones geoquímicas a nivel traza entre diferentes fases silíceas para un mismo depósito de sinter?, ¿cómo se podrían enriquecer ciertas fases silíceas con respecto a una fase previa de la secuencia diagenética en sistemas geotermales activos? y ¿qué impacto tiene la precipitación de sílice en la captura de metales a nivel traza en sistemas geotermales activos?

Para responder las preguntas planteadas en esta investigación, se estudió el depósito de sínter silíceo del campo geotermal activo de Puchuldiza (4.200 m s.n.m), en el Altiplano del norte de Chile. En el Altiplano se han descrito caraterísticas texturales y geoquímicas únicas para depósitos de sínter como en El Tatio, resultado de las extremas condiciones climáticas (Garcia-Valles et al., 2008; Nicolau et al., 2014). El depósito de sínter de Puchuldiza ha sido caracterizado como un depósito con concentraciones anómalas de especies metálicas en superficie (ej.: Cusicanqui y Mahon, 1980; Amberg, 2011), es por esto que representa un lugar idóneo para abordar y responder las preguntar científicas planteadas.

1.3 Trabajos Anteriores

Los depósitos de sínter silíceo han sido objeto de estudios multidisciplinarios por parte de la comunidad científica, al representar expresiones superficiales de sistemas hidrotermales activos e inactivos, por lo que se han investigado para caracterizar e identificar campos geotérmicos, depósitos epitermales, condiciones paleoambientales, presencia y proliferación de microorganismos termófilos y su relación con procesos de precipitación, y en búsqueda de evidencias de los primeros organismos terrestres (Cady and Farmer, 1996; Konhauser and Ferris, 1996; Herdianita et al., 2000et al., 2000; Guido et al., 2002; Pancost et al., 2005; Phoenix et al., 2005; Lynne et al., 2007; Lynne et al., 2008; Uysal et al., 2011; Orange et al., 2013; Campbell et al., 2015). Esta diversidad de investigadores ha propiciado el desarrollo de metodologías estándares de caracterización de las muestras de roca, cuyos protocolos son ampliamente utilizados. Es por esto que se ha propuesto como línea base de caracterización de muestras de sínter, el reconocimiento y clasificación de las fases silíceas mediante difracción de rayos X, según el valor del ancho medio del peak de difracción (*Full Width at Half Maximum* - FWHM) (Smith, 1998; Herdianita, et al., 2000; Lynne et al., 2005; Lynne et al., 2007). Lynne et al. (2005), proponen rangos de valores del FWHM característicos a cada fase silícea, al estudiar muestras de sínter del campo *Opal Mound* en Estados Unidos. Es por esto que se considera que valores mayores a ~ 2.8 corresponderían a ópalo A, ~5.8-2.5 a ópalo A/CT, ~2.5-1 a ópalo CT, ~1-0.5 a ópalo C, y valores bajo ~0.5 a cuarzo (Lynne et al., 2005). En los casos en que las morfologías de los polimorfos de sílice sean menores a 10 mm, Herdianita et al. (2000) sugieren el uso de espectrometría de dispersión Raman para definir las fases silíceas. A pesar de que cada fase silícea posee una morfología particular (Herdianita et al., 2000; Lynne et al., 2008), Lynne et al. (2007) estudiaron la relación entre la morfología y los grados de cristalinidad en muestras de sínter de los campos *Steamboat Geysers*, *Opal Mound* y *Steamboat Springs* en Estados Unidos, y del campo *Sinter Island* en Nueva Zelanda, proponiendo que los cambios de cristalinidad de la sílice precede a las variaciones morfológicas.

Además de las características cristalográficas de la sílice, se ha investigado el desarrollo morfológico de los campos de sínter. Según Boudreau y Lynne (2012), la modelación morfológica de los depósitos sería dependiente, principalmente, de la tasa de precipitación de sílice y de los grados de evaporación del fluido hidrotermal; siendo más eficiente en zonas de

evaporación completa. Boudreau y Lynne (2012), proponen tres ambientes principales de formación de sínter, definidos como: áreas que permanecen continuamente bajo el agua, zonas mojadas esporádicamente como las zonas que bordean un *geyser*, y regiones subaéreas que son inundadas por sobre flujos. Otra problemática asociada a los depósitos, es la definición areal y mapeo en forma remota, basado en esta problemática autores como Vaughan et al. (2005) y Preston et al. (2005) caracterizaron las mineralógicas del sínter de los campos *Steamboat Spring* (Estados Unidos) y en las provincias geotermales de *Waiotapu* (Nueva Zelanda) y *Haukadalur* (Islandia), respectivamente; mediante el estudio de imágenes multiespectrales.

El desarrollo y tipo de texturas de las muestras de sínter se consideran vestigios característicos de la actividad biológica e hidrológica del sistema hidrotermal, permitiendo generar mapas de paleo flujos, estableciendo de forma certera las zonas de up-flow de los sistemas (Lynne, 2012a; Lynne, 2012b). El desarrollo textural en los depósitos de sínter fue documentado en detalle por Lynne et al. (2012a), quienes estudiaron las macro texturas, relacionándolas a propiedades hidrodinámicas, rangos de temperatura e influencia biológica. Estos autores propusieron una clasificación textural asociada a bajas temperaturas con influencia biótica, texturas bióticas de mediana temperatura, texturas abióticas de alta temperatura y texturas de flujo. Además de las condiciones ambientales asociadas a factores bióticos y de temperatura del fluido que condicionan los estilos texturales desarrollados, Lynne et al. (2012b) plantea que diferentes condiciones ambientales propias de sistemas emplazados en distintas topografías, podrían influir en el desarrollo textural, al considerar las características de depósitos de sínter a baja altura como *Orakei Korako* en Nueva Zelanda y el sínter del campo geotérmico de El Tatio en el Altiplano del norte de Chile. Para abordar esta problemática, Nicolau et al. (2014), estudiaron los posibles controles ambientales del Altiplano en la formación de sínter en El Tatio y propusieron que las bajas temperaturas entre el día y la noche sumado a la alta tasa de evaporación, gatillarían el desarrollo de texturas asociadas a congelamiento (fragmentos silíceos o *silica platelets* y micro *columns/ridges*) y promoverían una alta tasa de precipitación de sílice (2.5 kg/m^2 por año). Según Lynne (2015), los factores ambientales influirían no solo en los procesos de precipitación y formación del sínter, sino que en la variación post-deposicional de las fases silíceas, acelerando o retardando los cambios diagenéticos. Específicamente, Lynne (2015) estudió de forma experimental la transición cristalográfica de muestras de sínter durante ocho años, en tres ambientes diferentes, concluyendo que la diagénesis de la sílice es acelerada en

depósitos de sínter expuestos a vapor, materia orgánica y abundante agua meteórica. Además de los factores abióticos, Orange et al. (2013) proponen que los factores bióticos como la presencia de microorganismos, afectarían la precipitación de sílice al proveer superficies de nucleación, lo que se evidenciaría en el desarrollo de texturas altamente porosas.

A nivel geoquímico, los depósitos de sínter están conformados principalmente por sílice, sin embargo pueden contener altas concentraciones de metales, lo que ha promovido su caracterización geoquímica como herramienta de exploración de depósitos epitermales de baja sulfuración (Guido et al., 2002; Uysal et al., 2011; Sillitoe, 2015). En este sentido, Uysal et al. (2011) estudiaron la geoquímica del depósito de sínter asociado a *Drummond Basin* en Australia, utilizando espectrometría de masas por plasma inductivamente acoplado (ICP-MS), estableciendo que las muestras de sínter que se emplazan cercanas a las zonas mineralizadas por oro están enriquecidas en elementos móviles (Cs, Li, Rb y Be). A nivel superficial, la geoquímica de las distintas facies que se desarrollan desde la fuente hasta los canales de descarga ha sido caracterizada por Hamilton et al. (2016), en el depósito de sínter de *Kohuamuri* en Nueva Zelanda; utilizando una combinación analítica de Absorción atómica (AAS), espectrometría de masas con plasma inductivamente acoplado (ICP-MS) y espectrometría de emisión atómica con plasma inductivamente acoplado (ICP-AES), estos autores proponen que las facies de sínter más cercanas a la fuente de emisión del fluido hidrotermal, y por ende en ambientes de alta temperatura, estarían enriquecidas en Pb, Cu, Zn, As, Sb y metales preciosos como Au y Ag. En general, la incorporación de especies metálicas a los depósitos de sínter ha sido relacionada a la precipitación de minerales accesorios y a la incorporación de cationes a la estructura silícea, lo que en el caso del sínter de El Tatio genera un alto grado de desorden estructural en la fase de ópalo A (Pope et al., 2005; Nicolau et al., 2014). Esta incorporación se asociaría, según McKenzie et al. (2001) a factores abióticos, descartando una posible influencia biológica en los procesos de fijación e incorporación metálica al sínter. No obstante, otros autores como Johnson et al. (2013) sugieren que los microorganismos que proliferan en ambiente termales como en el sínter, tendrían una cierta influencia en la fijación de metales y en la formación de nano-partículas durante la formación del sínter.

Investigaciones recientes como las de Geilert et al. (2015) y (2016) han estudiado las variaciones isotópicas de silíceo en depósitos de sínter, con el fin de caracterizar las condiciones

paleo-climáticas de depósitos de paloe-sínter. Geilert et al. (2016), al estudiar muestras de sínter del depósito *Geysir*, en Islandia, sugieren que el fraccionamiento de isótopos estables de silíceo decrece con tasas de precipitación de sílice altas, y varía durante la transición diagenética en un 1.3‰ entre cada fase. Estos cambios serían producidos por procesos de disolución, reprecipitación, por cambios químicos y de temperatura ocurridos en el sínter producto de la transición diagenética.

1.4 Hipótesis de trabajo

Las variaciones cristalográficas y micro-morfológicas de la sílice durante la transición diagenética, promueven el enriquecimiento y/o empobrecimiento en metales preciosos y metaloides de las fases silíceas en depósitos de sínter.

1.5 Objetivos

1.5.1 Objetivo general

Determinar la relación entre los grados de cristalinidad y micro-morfología de las fases silíceas en sínter con la concentración de elementos trazas.

1.5.2 Objetivos específicos

- Caracterizar las micro-morfologías presentes en las muestras de sínter mediante microscopía electrónica de barrido, tanto de las fases silíceas, como de los minerales accesorios y microorganismos presentes.
- Establecer las morfologías mejor preservadas para realizar análisis geoquímicos.
- Definir grados de cristalinidad de las muestras de sínter mediante difracción de rayos X.
- Cuantificar la composición química en cada fase silícea mediante ablación láser conectada a un espectrómetro de masas con plasma inductivamente acoplado (LA-ICP-MS).
- Describir los posibles mecanismos de enriquecimiento en metales preciosos y metaloides de las fases silíceas.

CAPITULO 2

GEOLOGÍA SECTOR PUCHULDIZA

2.1 Generalidades

El campo geotérmico de Puchuldiza está ubicado en la ragión de Tarapacá, a ~ 200 km al noreste de la ciudad de Iquique (19.412925ºS, 68.959900ºW) y a una altura de 2.400 m s.n.m. Climáticamente, se caracteriza por bajas precipitaciones, con temporadas lluviosas entre los meses de Noviembre y Marzo producto del Monzón sudamericano (Zhou and Lau, 1998), y por variaciones de temperatura entre el día y la noche que alcanzan los 35°C (Fernandez-Turiel et al., 2005). A nivel regional se emplaza en la unidad morfoestructural denominada cordillera occidental, correspondiente al borde oeste del *plateau* altiplánico (Montenegro et al., 2008; Ortiz, Lciano Achurra, et al., 2008). Localmente, se encuentra en una depresión volcano-tectónica controlada por un sistema de fallas de rumbo-normal NNE-SSW (Lahsen et al., 2005; Tassi et al., 2010; Amberg, 2011). Las litologías se caracterizan por secuencias continentales Cretácicas y secuencias volcánicas miocénicas a pliocénicas, junto a depósitos holocénicos de ceniza, glaciales, coluviales y aluviales (Lahsen, 1970; Lahsen et al., 2005).

La actividad geotermal de Puchuldiza presenta diversas expresiones superficiales tales como alteraciones hidrotermales, depósitos de sínter silíceo, fumarolas, *geysers* y fuentes termales, actividad que ha sido asociada al volcanismo del Cuaternario - Pleistoceno (Amberg, 2011). La zona central del área presenta una intensa silicificación caracterizada por un depósito de sínter silíceo de ~1 km^2 y ~25 m de espesor (Ortiz et al., 2008), alrededor del depósito de sínter se presenta un extenso halo de alteración caracterizado por asociaciones minerales de baja sulfuración, tipo sericita y adularia (JICA, 1979; Urzúa, 1999; Amberg, 2011).

2.2 Estratigrafía

La estratigrafía del campo geotérmico de Puchuldiza está constituida principalmente por unidades volcánicas, volcanoclásticas, aluviales, coluviales y galciales, con edades que varían

entre el Oligoceno superior hasta el Holoceno. El conjunto de principales unidades está representado en el mapa geológico de la Figura 1.

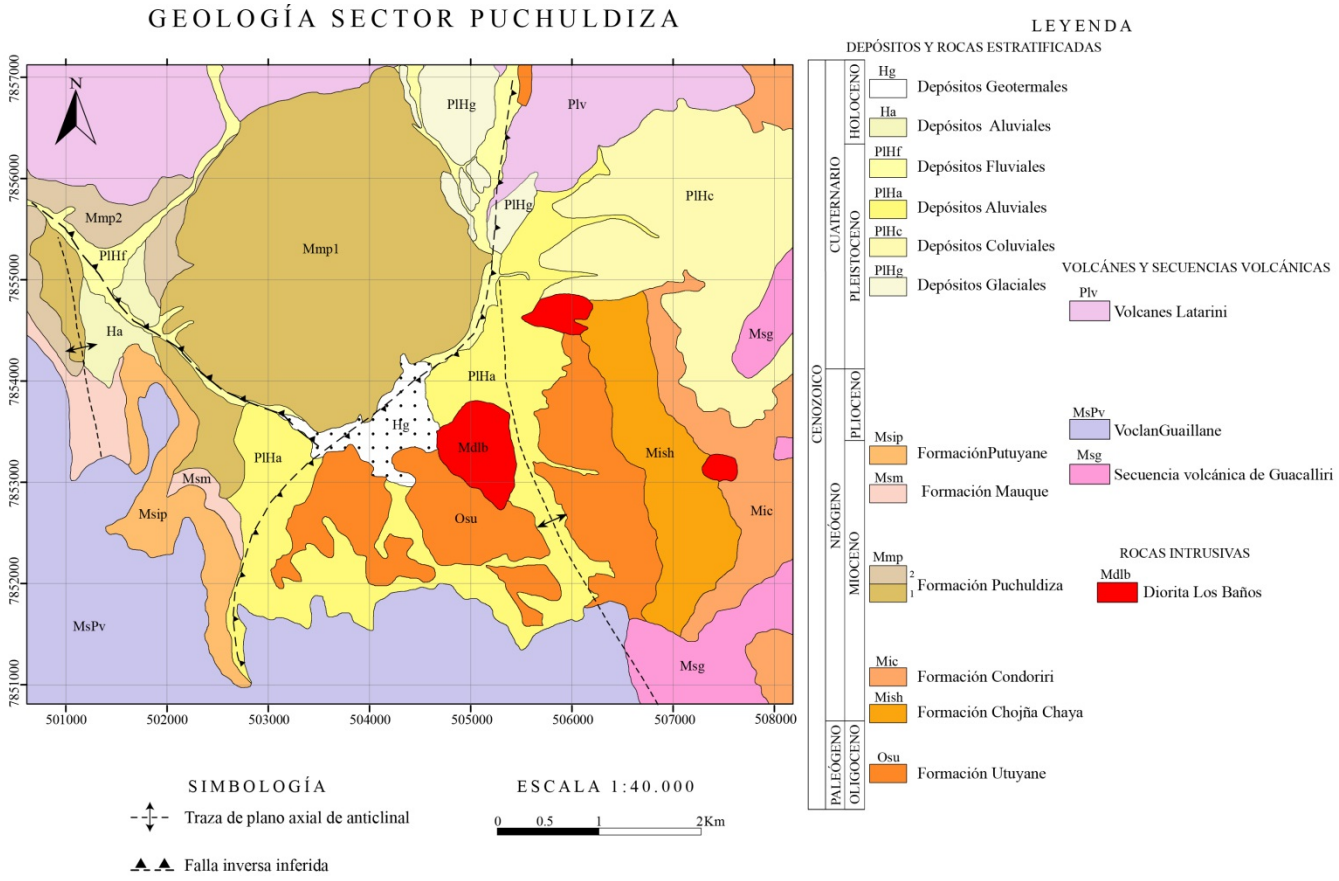

Figura 1. Mapa geológico del sector de Puchuldiza. Adaptado de Ortiz et al. 2008 y Cortés et al. 2014.

2.2.1 Depósitos y Rocas Estratificadas

2.2.1.1 Formación Utayane - Osu (Oligoceno superior – Mioceno inferior**)**

Representa la unidad más antigua aflorante en el sector (Lahsen, 1970). Litológicamente está constituida por una sucesión de 600 m de tobas de lapilli y ceniza de composición intermedia a ácida, con una intercalación de 100 m de rocas sedimentarias. La unidad sedimentaria presenta rocas de origen continental, como areniscas medias a gruesas, conglomerados y areniscas conglomerádicas (Ortiz et al., 2008; Cortés et al., 2014). Las rocas de esta formación se encuentran altamente plegadas y en contacto tectónico con la formación Puchuldiza por medio de la Falla Mulluri-Grande (Ortiz et al., 2008; Cortés et al., 2014).

Dataciones U-Pb en circones realizadas por Cortés et al. (2014) en las tobas, sugieren edades de base a techo en el primer miembro de rocas volcánicas entre los 26±0.4 y 22.5±0.4 Ma. respectivamente, mientras que para las tobas sobre el miembro sedimentario se determinaron edades U-Pb en circones de 22.7±0.8 Ma. y 19.3±0.3 Ma.; restringiendo al miembro sedimentario de 22 a 23 Ma. Tanto Cortés et al. (2014) como Ortiz et al. (2008), sugieren que esta formación se generó en un ambiente continental de cuencas de intra-arco con volcanismo ácido explosivo, con un escaso transporte de sedimentos asociado a ambientes aluviales.

2.2.1.2 Formación Chojña Chaya - Mich (Mioceno inferior)

Formación compuesta por una sucesión de rocas epiclásticas de origen continental. Posee una potencia estimada de 400 m de areniscas medias con lentes de conglomerados y pómez en el techo. Sobreyace a la formación Utayane por medio de un contacto erosivo discordante, y subyace por una discordancia angular de erosión a la formación Condoriri, lo que sugiere una edad Miocénica inferior (Cortés et al., 2014). Se habría generado en un ambiente sin-tectónico de intra-arco, asociada probablemente al desarrollo del anticlinal Baños de Puchuldiza; y representaría una sucesión de depósitos fluviales y aluviales tanto proximales como distales (Ortiz et al., 2008; Cortés et al., 2014).

2.2.1.3 Formación Condoriri - Mic (Mioceno inferior)

Posee una potencia estimada de 600 m, compuesta por tobas de ceniza y lapilli masivas, con líticos alterados hidrotermalmente y pómez intercaladas. Hacia el techo presenta estratos de areniscas epiclásticas gruesas con paleocanales. Subyace a la formación Guacalliri y a la formación Puchuldiza. Es intruida por un stock diorítico y diques andesíticos. Se restringe su edad al Mioceno inferior, según dataciones por U-Pb en circones que arrojaron edades de 18.6±0.2, 19.7±0.5, 19.2±0.2 Ma. de base a techo respectivamente (Cortés et al., 2014).

Esta formación se ha interpretado como una sucesión de ignimbritas y en menor medida, oleadas piroclásticas producto del volcanismo riolítico explosivo en un ambiente de intra-arco (Ortiz et al., 2008; Cortés et al., 2014).

2.2.1.4 Formación Puchuldiza - Mmp (Mioceno medio)

Formada por secuencias volcánicas con una potencia total de 400 m, posee un miembro inferior de lavas andesíticas autobrechizadas y uno superior de tobas de cenizas y lapilli (Ortiz et al., 2008). Dataciones K/Ar en biotitas de tobas del miembro superior, arrojaron edades de 14.2±0.5 y 15.7±0.6 Ma., siendo asignada al Mioceno medio (Ortiz et al., 2008).

Esta formación presenta una gran deformación en un anticlinal y sinclinal, limitada al este por la falla Mulluri-grande (Cortés et al., 2014). Las rocas de esta formación habrían sido formadas en un ambiente volcánico inicialmente efusivo y posteriormente explosivo (Cortés et al., 2014).

2.2.1.5 Formación Mauque - Msm (Mioceno superior)

Esta formación está constituida por areniscas epiclásticas, clastos volcánicos y conglomerados formados por gravas aluviales, con una potencia de 200 m (Cortés et al., 2014). Sobreyace en discordancia angular a la formación Condoriri, a volcanes del mioceno inferior, a la formación Puchuldiza, a lavas dacíticas del Mioceno y a la secuencia volcánica de Guacalliri. Se encuentra en contacto por falla con rocas de la formación Utayane (Ortiz et al., 2008; Cortés et al., 2014). Dataciones por K-Ar ubican a esta formación en el Mioceno superior, con 11.6±0.9 Ma. como edad máxima (Ortiz et al., 2008). Esta formación habría sido el resultado de procesos de depositación aluvial y fluvial próximos a las unidades adyacentes (Cortés et al., 2014).

2.2.1.6 Ignimbrita Putuyane - Msip (Mioceno superior)

Caracterizada por Tobas de lapilli, tobas de lapilli líticas y depósitos de remoción en masa con bloques angulosos, llegando a un espesor de 40 m en total. Dispuesta de forma subhorizontal y discordanate sobre lavas de la formación Puchuldiza y concordante con formación Mauque, posee una edad asignada al Mioceno superior, con 6.99±0.33 Ma. por K-Ar en biotitas (Ortiz et al., 2008; Cortés et al., 2014).

2.2.1.7 Depósitos Glaciales PlHg (Pleistoceno-Holoceno)

Depósitos polimícticos tipo gravas y bloques angulosos, de composición andesítica, provenientes del volcanismo plio-pleistoceno (Ortiz et al., 2008). Presentan morfologías

morrénicas laterales y de centro, y en menor medida frontales y basales (Ortiz et al., 2008; Cortés et al., 2014).

2.2.1.8 Depósitos Coluviales PlHc (Peistoceno – Holoceno)

Depósitos no consolidados formados principalmente por bloques y gravas angulosas monocomposicionales, generados por efectos gravitacionales en las laderas (Cortés et al., 2014).

2.2.1.9 Depósitos Aluviales PlHa (Pleistoceno - Holoceno)

Depósitos pobremente consolidados formados por gravas, arenas de mala selección, limos y bloques, se disponen en terrazas y abanicos aluviales sobrepuestos (Ortiz et al., 2008; Cortés et al., 2014). Se encuentran cubiertos por depósitos aluviales recientes (Ortiz et al., 2008).

2.2.1.10 Depósitos Fluviales- PlHf (Pleistoceno – Holoceno)

Depósitos compuestos por material clástico heterocomposicional, subanguloso a redondeado, con distintos tipos de estratificación (Cortés et al., 2014). Depósitos heterogéneos en bancos de arenas y gravas, formados por conglomerados de clastos redondeados de origen volcánico. Se asocian a cursos fluviales continuos e intermitentes (Ortiz et al., 2008).

2.2.1.11 Depósitos Aluviales Ha (Holoceno)

Depósitos no consolidados a medianamente consolidados, conformados por ripio, grava, arena y limo. Morfológicamente forman abanicos aluviales (Ortiz et al., 2008).

2.2.1.12 Depósitos Geotermales de sínter silíceo - Hg (Holoceno)

Depósitos de ~1 km^2, con una potencia estimada de 25 m (Ortiz et al., 2008). Está formado por diferentes polimorfos de sílice y minerales accesorios como halita, estibnita, entre otros; junto con variados microorganismos termófilos. Su formación es producto del afloramiento de aguas termales a alta temperatura (54-87ºC). Cubre parcialmente a la formación Puchuldiza y a las rocas más antiguas de la formación Utayane. Los depósitos asociados tanto a fuentes termales activas como a inactivas poseen diferentes texturas asociadas a actividad biológica, zonas de alta a baja temperatura; y zonas de alta y baja velocidad de flujo.

2.2.2 Volcanes y Secuencias Volcánicas

2.2.2.1 Secuencia volcánica de Guacallire - Msg (Mioceno superior)

Formada por basaltos y andesitas basálticas, posee una potencia estimada de 150 m y una edad de 10.6 ±1 M.a., según Ortiz et al. (2008), por medio de análisis K-Ar en roca total. Se dispone de forma discordante sobre el miembro inferior de la formación Condoriri y por discordancia de erosión bajo rocas de la formación Mauque (Ortiz et al., 2008).

2.2.2.2 Volcán Guaillane - MsPv (Mioceno superior - Plioceno)

Estratovolcán de 4.952 m s.n.m, fuertemente erosionado formado por secuencias lávicas de afinidad dacítica (Ortiz et al., 2008). Las coladas poseen morfologías *aa*, junto con *levées* y lóbulos de avance. Análisis K/Ar en biotitas de las coladas arrojaron edades de 3.5±0.2, 4.6±0.3 y 4-8±0.3 M.a, asignándolo una edad pliocénica (Ortiz et al., 2008; Cortés et al., 2014).

2.2.2.3 Volcán Latarani (Pleistoceno) - Plv

Estratovolcán altamente erosionado por acción glacial, caracterizado por coladas andesíticas y domos dacíticos (Ortiz et al., 2008; Cortés et al., 2014). Se le ha asignado una edad Plioceno-Pleistoceno inferior, con 2±0.4 y 0.9±0.3. M.a. por K/Ar en biotitas de un domo dacítico.

2.2.3 Rocas Intrusivas

2.2.3.1 Diorita Los Baños - Mdlb (Mioceno medio-superior)

Cuerpo diorítico de grano fino de carácter hipabisal. Intruye a la formación Condoriri y Chojña Chaya. Se asigna una edad miocénica, aunque sin exactitud ya que no existen edades radiométricas reportadas (Cortés et al., 2014).

2.3 Geología estructural

Según Cortés et al. (2014), en el sector prevalecen dos dominios estructurales asociados a regímenes compresivos tales como anticlinales, flexuras y fallas de escala regional y local, con orientación NNO-SSE, que afectan principalmente a unidades del Oligoceno superior – Mioceno superior. Los dominios estructurales comprenden el dominio Occidental formado por el anticlinal Baños de Puchuldiza, el anticlinal de Chilani y las fallas Arabilla y Mulluri-grande, y el dominio Oriental conformado por los anticlinales Chío y Huailla.

El sector de Baños de Puchuldiza se emplaza en el dominio estructural Occidental y ha sido afectado por diversas fases tectónicas distensivas y compresivas, entre las que se considera la fase compresiva durante el Mioceno superior (Lahsen, 1978) que habría formado el anticlinal de Puchuldiza. Este anticlinal se caracteriza regionalmente por poseer una orientación NNO-SSE con vergencia hacia el este afectando a las formaciones Utayane y Puchuldiza, se encuentra disectado por estructuras locales como la falla Mulluri-Grande y aflora parte del núcleo y del limbo frontal del pliegue, formando los cerros Condoriri y Guacalliri. Seguida de esta fase compresiva, se habría producido una fase distensiva que generó diversos sistemas de fallas, gatillando el movimiento diferencial de bloques Plioceno-Cuaternarios, moldeando una configuración tectónica de graben de origen tectónico limitado por fallas (Urzúa, 1999; Lahsen, 1978). Otras estructuras reconocibles en este dominio estructural son la flexura Queñiza y Paica, correspondientes a monoclinales bien marcados, que afectan a rocas del miembro inferior de la formación Condoriri, y en menor medida a rocas de la secuencia volcánica Guacalliri y conglomerados de la formación Mauque.

A nivel local se distinguen las falla inversa Mulluri-Gande y la falla Puchuldiza, posiblemente de alto ángulo y rumbo NNE-SSO y NO-SE, respectivamente. La falla Mulluri-Grande rompe el limbo trasero del anticlinal Baños de Puchuldiza y se acota su actividad al Mioceno superior al encontrarse sellada por coladas no deformadas de los volcanes Latarani y Guaillane (Cortés et al., 2014).

2.4 Hidrogeoquímica

En el campo geotérmico de Puchuldiza se han reconocido diversas expresiones geotérmicas en superficie, tales como *geysers* y manantiales termales. Es por esto que, de forma complementaria, en esta investigación se muestrearon nueve fuentes de aguas asociadas a los depósitos de sínter estudiados (Fig. 2), con el fin de reportar las concentraciones químicas de las especies en el fluido hidrotermal.

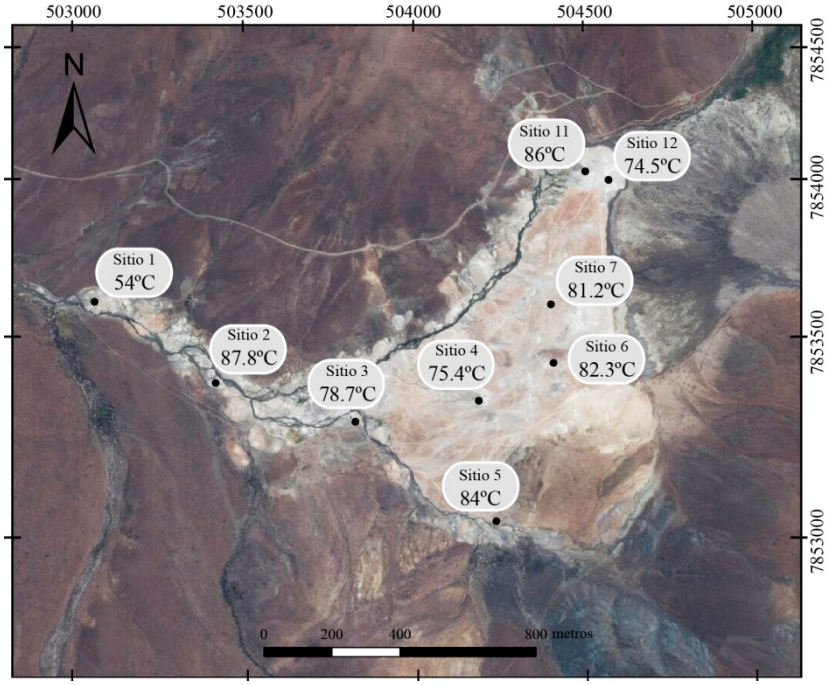

Figura 2. Campo geotérmico de Puchuldiza. Se presenta la distribución de las fuentes termales muestreadas junto con las temperaturas medidas.

2.4.1 Metodología

Las aguas muestreadas fueron filtradas con filtros de 0.45 µm de acetato de celulosa. Además de registrar la temperatura y pH en terreno. Una vez obtenida el agua, ésta fue almacenada en botellas de polipropileno, previamente limpiadas. Este procedimiento fue empleado tanto para análisis de cationes como de aniones. Además, las muestras para cationes mayores y metales trazas fueron acidificadas con HNO_3 (0.65 ml en 150 ml de agua) en una concentración de 4N.

Las muestras para cationes y aniones mayores fueron analizadas en el laboratorio de geoquímica de fluidos del CEGA. Las concentraciones de Cl^-, SO_4^{-2}, F^-, Br^-, y NO_3^- fueron determinadas por cromatografía iónica (IC, Thermo Scientific Dionex ICS 2100), mientras que las concentraciones de Na^+, Ca^{+2}, Mg^{+2} y SiO_2 se determinaron mediante espectrofotometría de absorción atómica (AAS, Perkin Elmer PinAAcle 900F). La concentración de K^+ se determinó mediante espectrometría de masas con plasma inductivamente acoplado (ICP-MS, Thermo iCAP Q con celda de colisión), y la alcalinidad se determinó por volumetría ácido-base siguiendo el método de Giggenbach y Goguel (1989). Finalmente, las concentraciones de elementos a nivel traza en el agua geotermal fueron analizadas utilizando espectrometría de masas de alta resolución con plasma inductivamente acoplado (HR-ICP-MS) en el laboratorio *Activation Laboratories* Ltd. (Actlabs), Canadá.

2.4.2 Geoquímica de aguas termales

La temperatura, pH y composición química de las muestras de aguas termales se presentan en la Tabla 3. El pH de las muestras varía entre 6.2 y 8.8 y la temperatura varía principalmente entre 75.4 y 87.8ºC, aunque se reportó una temperatura menor, de 54.4ºC en el sitio 1. Las aguas presentan un total de sólidos disueltos en el rango de 4000 a 4500 mg/l, siendo mayor al promedio de fuentes termales del norte de Chile de 3770 mg/l (Tassi et al., 2010). Las concentraciones de aniones y cationes principales de las muestras se presentan en un diagrama Piper en la Figura 3, en donde resalta el dominio composicional de Cl^- y Na^+ caracterizando a las muestras de agua como aguas cloruradas sódicas. Las concentraciones de cloruro varían entre 2389 y 2616 mg/l, correspondientes a los sitios 1 y 6 respectivamente y su proveniencia se asocia a la desgasificación magmática que libera HCl y como resultado de la interacción con la roca circundante, su alta concentración se relacionaría a un rápido ascenso del fluido geotermal (ej., Ellis and Mahon, 1977; Pope and Brown, 2014). Las concentraciones de sodio están en el rango 1405-1625 mg/l en los sitios de muestreo 3 y 7, y su incorporación, al igual que el Cl^-, sería el resultado de la interacción agua-roca (Giggenback, 1991).

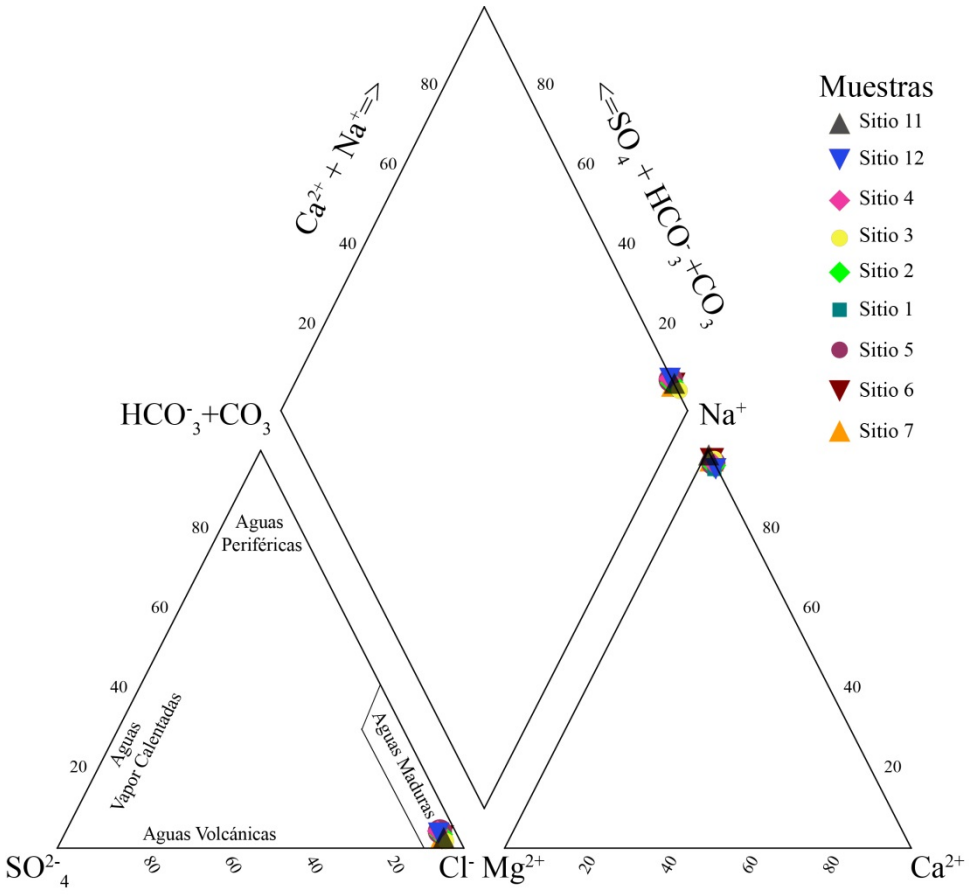

Figura 3 Diagrama Piper con datos analíticos medidos, mostrando que las aguas de Puchuldiza son aguas maduras clorurado sódicas.

Según el diagrama ternario SO^{2-}_4, Cl^-, CO_3 (Fig. 3), las aguas presentan una tipología de aguas maduras debido a la prolongada interacción agua-roca, lo que promueve el equilibrio químico entre las soluciones termales y la roca circundante (Montenegro et al., 2008). Este tipo de aguas representa una característica común entre fuentes termales provenientes de reservorios geotérmicos (Tassi et al., 2010) y se asociarían a estratovolcanes de cámaras magmáticas someras (Montenegro et al., 2008) como el volcanismo pleistocénico del Volcán Latarani, cercano al campo geotérmico de Puchuldiza (Amberg, 2011).

Adicionalmente, las aguas termales presentan una variada composición, reportándose una concentración de SiO_2 entre 105 y 187 mg/l en los sitios 1 y 4, concentraciones de bromo entre 4.27 y 7.58 mg/l para los sitios 1 y 7; junto con concentraciones de boro variable entre 75.8 y 88.6 mg/l. A nivel traza las aguas se caracterizan por el enriquecimiento en metales. Es así que se determinaron concentraciones de oro mayores a 0.4 ng/l, llegando a 1.8 ng/l en el sitio 5.

También se registró una concentración de cobre de 6.94 a 18.4 µg/l, junto a concentraciones relativamente homogéneas de arsénico entre 11 y 12.8 mg/l. Otras especies determinadas fueron mercurio entre 0.039 y 0.1 mg/l en los sitios 1 y 3 respectivamente, además de antimonio entre 0.028 mg/l en el sitio 1 y 0.91 mg/l en el sitio 5.

2.4.5 Geotermometría

La temperatura del reservorio geotérmico se estimó utilizando el geotermómetro de cationes Na-K-Mg basado en (Giggenbach, 1988). Las muestras ploteadas en la Figura 4, recaen en el campo de equilibrio parcial y sugieren una temperaturas entre los 240 a 270ºC. Las muestras que presentan la menor temperatura se localizan en los sitios 1 y 2, lo que podría asociarse a una posible mezcla con aguas meteóricas en subsuperficie (Urzúa, 1999). Esta estimación coincide con las reportadas previamente por Lahsen (1970) y Tassi et al. (2010), quienes sugieren temperaturas aproximada de equilibrio entre 200 - 270ºC. A pesar de esto, los rangos de temperaturas propuestos no son consistentes con las mediciones hechas en pozos por parte de JICA, 1979, quienes reportaron una temperatura máxima medida cercada a 170ºC a una profundidad de 1100 m aproximadamente. Esto sugiere que los pozos no alcanzaron los acuíferos de mayor temperatura ubicados probablemente a mayor profundidad (Urzúa, 1999).

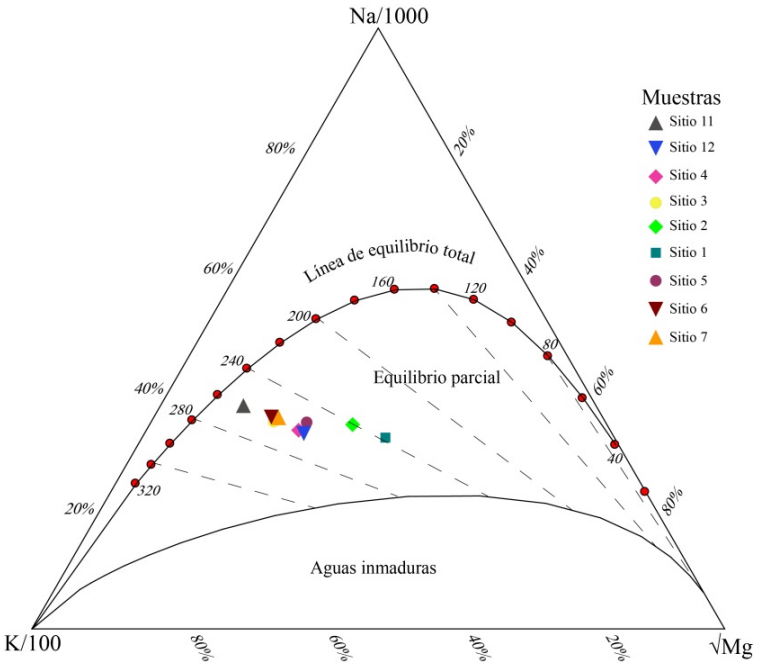

Figura 4. Diagrama de cationes (K, Na y Mg), basado en Giggenbach, 1988. Según el gráfico la temperatura del sistema hidrotermal fluctuaría entre 240 a 270ºC.

La fuente de calor del sistema geotérmico se ha relacionado a calor relicto de cuerpos subvolcánicos ligados a la actividad volcánica Pleistocénica del complejo Latarani-Macurquima (Ortiz et al., 2008), que disiparía el calor de forma conductiva a las rocas y a los fluidos hidrotermales (Lahsen, 1978).

La recarga del sistema hidrológico se ha relacionado a un sistema mixto pluvio-nival cuyas zonas de recarga se localizarían en las cumbres de los volcanes de la hoya hidrográfica tanto al norte como noreste del campo geotérmico (Urzúa, 1999; Ortiz et al., 20808, Amberg, 2011). El reservorio en profundidad se correlaciona a capas permeables de las formaciones Condoriri, Chojña Chaya o Utayane (Lahsen, 1978; Urzúa, 1999; Montenegro et al., 2008; Ortiz, et al., 2008), cuyas litologías se caracterizan por composiciones intermedias (Mahon and Cusicanqui, 1980). Los fluidos permanecerían confinados en acuíferos subhorizontales y pseudoconcordanes a la estratificación, hasta alcanzar estructuras preferentes como la falla Puchuldiza y Mulluri-grande por donde ascenderían a la superficie formando las manifestaciones reconocibles en Puchuldiza (Ortiz et al., 2008).

CAPITULO 3

GEOCHEMISTRY OF METALS AND METALLOIDS IN SILICEOUS SINTER DEPOSITS: IMPLICATIONS FOR ELEMENTAL PARTITIONING INTO SILICA PHASES

CAMILO SÁNCHEZ-YÁÑEZ[1*], MARTIN REICH[1], MATHIEU LEISEN[1], DIEGO MORATA[1], FERNANDO BARRA[1].

[1] Department of Geology and Andean Geothermal Center of Excellence (CEGA), Universidad de Chile, Plaza Ercilla, 803, Santiago, Chile.

Corresponding author: * casanche@ing.uchile.cl

Abstract

Sinter deposits are formed by precipitation of silica from hydrothermal fluids that have reached the surface environment. They are commonly found around hot springs and represent surface expressions of underlying geothermal systems and/or low sulfidation, epithermal gold-silver hydrothermal deposits. Several studies have reported ppm to weight percent concentrations of metals (e.g., Au, Ag, Cu) and metalloids (e.g., As, Sb, B) in sinters capping geothermal systems and epithermal gold-silver deposits. However, the relation between the maturity of the siliceous sinter and its metal enrichment remains unknown. Here we use geochemical and mineralogical data that links the silica crystallinity degree with trace metal and metalloid contents in sinter. In this paper, we provide in situ trace element data in metal-rich silica sinter samples from the Puchuldiza geothermal field in the Altiplano of northern Chile that record the complete diagenetic sequence from non-crystalline opal A to microcrystalline quartz. Combined SEM, XRD and LA-ICP-MS data show that the concentration of metals and metalloids in sinters from Puchuldiza display a strong correspondence with silica crystallinity. While arsenic and boron are predominantly enriched in the more amorphous silica phases (opal A/CT), gold and silver show higher concentrations in the more crystalline phases (opal C/quartz). Silica structural, morphological and geochemical transformations from its initial precipitation to its final maturation after diagenesis are the responsible for this differential enrichment. During the initial stages, gold and silver are incorporated into silica spheres either as cationic species and/or metal

nanoparticles or colloids, while arsenic and boron incorporation is controlled by As-bearing accessory minerals and Fe-oxyhydroxides. As diagenesis progresses and the crystallinity of silica increases, diffusion-driven processes such as Ostwald ripening progressively enrich gold and silver in the sinter, while metalloids are depleted owing to the low retention of arsenic by silica. These findings indicate that the diagenetic transitions of silica, defined by significant structural changes that involve generation of surface defects and the creation of reactive sites, may play an important role in elemental uptake by silica in near surface environments.

Keywords: Puchuldiza, Altiplano, high-altitude, siliceous sinter, silica crystallinity, precious metals, metalloids, nanoparticle, Ostwald ripening

3.1 Introduction

Siliceous sinters (or sinters) are natural chemical sedimentary deposits formed at or near the surface by abiotic precipitation from silica-rich, near neutral hydrothermal fluids as they discharge and cool at the surface (Fournier and Rowe, 1966; Rodgers et al., 2004; Lynne et al., 2007). Sinter deposits are commonly found around hot springs and represent surface expressions of underlying geothermal systems and/or low sulfidation, epithermal gold-silver deposits (Parker and Nicholson, 1990; Guido et al., 2002; Rodgers et al., 2004; Lynne et al., 2007; Sillitoe, 2015). Since sinter deposits form above the water table and close to the surface, they are commonly used to identify the paleoenvironmental conditions of extinct hot spring systems (Lynne et al., 2008). Furthermore, the identification and geomorphic interpretation of these paleosurface products can be used as guides for the exploration of concealed geothermal resources and epithermal precious metal deposits (Parker and Nicholson, 1990; Guido et al., 2002; Rodgers et al., 2004; Lynne et al., 2007; Sillitoe, 2015). Additionally, recent studies on silica sinter deposits have revealed preservation pathways of environmentally controlled, microbe-dominated sedimentary facies and biosignatures that are relevant to astrobiological investigation (Konhauser et al., 2001; Konhauser et al., 2003; Handley et al., 2005; Gibson et al., 2014; Campbell et al., 2015).

Sinter deposits are texturally complex and are predominantly composed of metastable silica phases ($SiO_{2*}nH_2O$) that include amorphous opal A, para-crystalline opal CT, opal C, and stable microcrystals of silica (SiO_2) including quartz and moganite (Smith, 1998; Rodgers et al., 2004; Lynne et al., 2007). In geothermal hot springs, silica precipitation is strongly controlled by the

undercooling of thermal water, evaporation rate, and changes in the pH and ionic strength of the hydrothermal fluid (Ichikuni, 1970; Rimstidt and Cole, 1983; Campbell et al., 2003; Rodgers et al., 2004; Tobler et al., 2008; Tobler and Benning, 2013; Nicolau et al., 2014). The first stage of sinter formation comprises the nucleation and polymerization of $Si(OH)_4$ monomers in the silica-saturated fluid. This promotes aggregation by coagulation and/or floculation of colloidal silica particles, with coarser grains formed by Ostwald ripening (Iler, 1979; Smith, 1998; Tobler et al., 2008; Tobler et al., 2009; Tobler and Benning, 2013). The first silica phases precipitated from the hydrothermal fluid have very low structural order and their morphologies result from aggregations of porous nano- to micro-sized silica spheres (Rodgers et al., 2004; Lynne et al., 2007). Silica undergoes further morphological and structural transitions as a result of changes in the thermodynamic equilibrium conditions, such as variable exposure to weathering, fluid re-circulation, and changes in the degree of silica saturation, temperature, pH, and evaporation rate, among others (Williams et al., 1985; Herdianita et al., 2000; Konhauser et al., 2001; Lynne and Campbell, 2004; Rodgers et al., 2004; Nicolau et al., 2014). Each silica phase displays particular morphologies as expressions of their internal structure. A higher structural order or maturation grade is reached during diagenesis as a result of increased density and a decrease in porosity and water content (Herdianita et al., 2000; Rodgers et al., 2004; Lynne et al., 2008).

Several recent mineralogical studies have focused on the texture, morphology, degree of crystallinity, and biogeochemical signatures of silica sinters (e.g., Herdianita et al., 2000; Rodgers et al., 2004; Fernandez-Turiel et al., 2005; Lynne et al., 2007; Garcia-Valles et al., 2008; Lynne, 2012b; Orange et al., 2013; Tobler and Benning, 2013; Nicolau et al., 2014), whereas other studies have centered on the presence of metals and metalloids in sinters that form common accessory minerals in low sulfidation gold-silver epithermal deposits (Ichikuni, 1970; Parker and Nicholson, 1990; Saunders, 1990; McKenzie et al., 2001; Guido et al., 2002; Guidry and Chafetz, 2003; Pope et al., 2005; Sillitoe, 2015). Common accesory minerals reported in different sinter deposits include, pyrite, stibnite, realgar, orpiment, and cinnabar. Additionally, amorphous arsenic and antimony sulfides have been identified in the Waiotapu sinter, New Zealand (Jones et al., 2001), and halite, sylvite, realgar, gypsum and cahnite have been reported at the El Tatio sinter deposits, in northern Chile (Nicolau et al., 2014). Sinter deposits can contain several elements at the ppm level (i.e., Au, Ag, Li, B, As, Mo, Hg, Cu, Pb, Sb, and W). In the Waiotapu geothermal field, New Zealand, reported gold and silver values range from 9.2 to 543 ppm and 3.7-33 ppm, respectively (Pope et al., 2005; Jones et al., 2001). Guido et al. (2002) have

documented 18-530 ppm of Ag and 3.8-8.1 ppm of Cu in paleo sinters from the El Deseado massif, Argentina, and Uysal et al. (2011) have shown that sinter samples from the Drummond Basin in Queensland, Australia, have up to 7.98 ppm of Cu. Despite these works, no studies have combined the sinter trace element geochemistry with the silica crystallinity degree. This is critical in order to determine the possible mineralogical controls on the abundance of trace metals in the sinter. Further, there is no published information regarding the form of these metals in the sinter, i.e., structurally bound into particular silica phases, or if they are incorporated as nano- to micro-sized mineral particles into sinter. This information is not only relevant to evaluate the partition of dissolved metal species into silica phases during sinter formation, but it is also crucial to better understand metal transport and precipitation in near surface hydrothermal systems, and to assess the potential impacts of silica precipitation on toxic metal uptake and release in the local environment.

This study provides new in situ trace element data in natural silica sinter samples that record the complete diagenetic sequence from non-crystalline opal A to microcrystalline quartz. The metal-rich silica sinter samples were obtained in the Puchuldiza geothermal field located in the Altiplano of northern Chile. This geothermal system has been previously evaluated for both high-enthalpy geothermal resources and as a potential epithermal gold-silver prospect (JICA, 1979). The purpose of this study is to determine the relation between the degree of silica crystallinity, the micro-morphology and the trace metal/metalloid content. We use a combination of techniques including scanning electron microscopy (SEM) observations, X-ray diffraction (XRD) structural characterization and laser-ablation inductively-coupled plasma mass spectrometry (LA-ICP-MS).

The high-altitude (>4.000 m a.s.l) silica sinter deposits of the Chilean Altiplano exhibit unique textural and mineralogical characteristics resulting from the extreme climatic conditions. These include a high degree of structural disorder, which is probably related to cation incorporation into the silica structure and/or the occurrence of micro- to nano-scale accesory minerals (Garcia-Valles et al., 2008; Nicolau et al., 2014). Our data indicates that the degree of silica crystallinity plays a fundamental role in the metal and metalloid uptake in geothermal systems.

3.2 Geological background and samples

The Puchuldiza geothermal field is located in the Altiplano Plateau of northern Chile (19.412925ºS, 68.959900ºW) at an elevation of 4200 meters above sea level (m a.s.l.), and 200 km east of the city of Iquique, Tarapacá region (Fig. 5). The geothermal field covers an area of ~1 km^2 (Fig. 6A) and the sinter deposits occur in a volcano-tectonic depression that is structurally controlled by a NW-SE reverse fault system and a NNE-SSW normal – strike-slip fault system (Lahsen et al., 2005; Tassi et al., 2010; Amberg, 2011). The geology of the area is represented by a Cretaceous continental sequence overlain by Miocene to Pliocene andesitic and dacitic lavas. Ash-flow tuffs, and glacial and alluvial deposits of Holocene age cover an important part of the area (Lahsen, 1970; Lahsen et al., 2005). The hydrothermal alteration is characterized by typical low sulfidation alteration assemblages, that is mainly sericite and adularia (JICA, 1979).

The Puchuldiza field has more than 100 surface expressions of geothermal activity that are related to the intersection of the fault systems described above. The area comprises an extensive paleo-sinter deposit (Fig 6 C,E), active siliceous sinters (Fig 6 F,G) and surface manifestations including hot, bubbling and thermal springs, fumaroles, geysers and mud pools (Fig 6 B,-D). The near boiling (87.6ºC at ~4.200 m a.s.l.) spring waters are characterized by a near-neutral pH and are rich in alkalis and chlorine (alkali-chloride type). Previous geothermometrical determinations indicate a geothermal reservoir temperature at depth in the range of 180º to 240ºC (JICA, 1979; Mahon and Cusicanqui, 1980; Lahsen et al., 2005).

The silica sinter deposits in Puchuldiza have a thickness of up to 25 m (Ortiz, Luciano Achurra, et al., 2008) and exhibit textures related to fast to intermittent flow of hot water. Siliceous sinters are characterized by different colorations that form bands, nodules or surface precipitates (Fig. 6 C,-E,-F,-G), probably related to changes in their chemical content and the incorporation of bio-materials such as thermophilic cyanobacteria and algae (Mahon and Cusicanqui, 1980).

Thirteen silica sinter deposits associated with active and inactive geothermal manifestations were selected for sampling based on their coloration and textures (Fig. 6A). The sinters were deposited on pool margins (Fig. 6B), and discharge channels (Fig. 6 D), with mature phases in deep pool and proximal vent facies. Textures such as geyseritic, lily-pad, palisade and streamer (Guidry and Chafetz, 2003; Lynne, 2012b) were recognized in various samples containing different silica phases. In active vents, the sinter samples were collected in both subaqueous and

subaerial settings. All sinter samples exhibited significant color variations in bands 0.2-0.5 cm wide. For each sample, fragments of consecutive bands related to a specific color were extracted to determine their mineralogy, crystallinity, micro-morphology and geochemical characteristics. Additionally, water samples were collected for chemical analysis and the pH and the water were measured on site.

3.3 Analytical Methods

Thirty-seven siliceous sinter samples were analyzed using X-ray powder diffraction (XRD) methods as a means of identifying microcrystalline silica phases and accessory minerals according to established protocols (Smith, 1998; N. Herdianita et al., 2000; Lynne et al., 2007; Nicolau et al., 2014). The XRD analyses were carried out using a Siemens D-5000 diffractometer in the Physics Department at the Universidad de Chile, Santiago. The untreated powder samples (<200 μm) were scanned at a rate of 0.6º2Θ/min, with a step size of 0.01º, from 0-80º2Θ, and operating conditions of 40 kV and 30mA. Accessory minerals were identified using the XPowder12 software. In all diffractograms, the value of the Full Width at Half Maximum (FWHM) was measured by fitting the curve and base line manually (Lynne et al., 2007). The FWHM is the main parameter used to determine the degree of structural disorder in different non-crystalline silica. This parameter was then used to assess the mineralogical maturation of silica (Smith, 1998; Lynne et al., 2007). The range of FWHM values that define silica phases are above ~5.8 for opal A, ~5.8-2.5 for opal A/CT, ~2.5-1 for opal CT, ~1-0.5 for opal C, and below ~0.5 for quartz (Lynne et al., 2005).

The samples analyzed by XRD were also studied by scanning electron microscopy (SEM) in order to determine the morphological characteristics of silica and the presence of accessory minerals. Clean silica sinter samples were coated with a thin carbon film, and later mounted on a sample holder with carbon tape. The analyses were performed at the Andean Geothermal Centre of Excellence (CEGA), Universidad de Chile, using a FEI Quanta 250 SEM equipped with secondary electron (SE), energy-dispersive X-ray spectrometry (EDS), backscattered electron (BSE) and cathodoluminescence (CL) detectors. The analyses were performed using a spot size of 1-3 μm, an accelerating voltage of 10-20 keV, a beam intensity of 80 μA, and a working distance of 10 mm.

Semi-quantitative EDS analyses were used to constrain major elements in individual mineral phases. The EDS operating conditions were 20 keV, a spot size of 1-3 μm and a working distance of 10 to 18 mm.

Eight representative sinter samples previously studied under the SEM and structurally-characterized by XRD were selected for major and trace element analyses in specific silica sinter phases (opal A, opal A/CT, opal CT, opal CT/C and opal C/quartz). The measurements were carried out in the Isotope Geochemistry Laboratory at CEGA, Universidad de Chile, using a Thermo Scientific™ iCAP™ quadrupole inductively coupled plasma mass spectrometer (Q-ICP-MS) coupled with a 193 nm ArF excimer laser (Photon Machines Analyte G2). The following isotopes were analyzed: ^{7}Li, ^{11}B, ^{23}Na, ^{24}Mg, ^{27}Al, ^{39}K, ^{44}Ca, ^{48}Ti, ^{54}Fe, ^{55}Mn, ^{63}Cu, ^{75}As, ^{79}Br, ^{107}Ag, ^{121}Sb, and ^{197}Au. The ICP-MS operates with a RF power of 1550 W and a vacuum pump with a capacity of $<1x10^{9}$ l/min with an acquisition time of 1.049 s for one cycle. Ablation was performed within a HelEx 2 cell, with two different spot sizes (20 and 30 μm) according to the grain size of silica in the samples. A repetition rate of 7 Hz and a constant fluency of 4.64 J/cm^2 were used with a 0.3 L/min flow of He as carrier gas. The calibration was performed using NIST 610 and 612 standards (National Institute of Standards and Technology). The samples were analyzed using a standard-sample-standard bracketing methodology. An Excel macro was developed for off-line data reduction. The data considered representative displayed a signal that is three times higher than the standard deviation of the background. Elemental quantification was carried out based on the normalization of the sum of all metal oxides to 100 wt.%. and the use of an ablation yield correction factor (AYCF) (Liu et al., 2008).

The concept behind this methodology can be developed as follows (equation 1 to 6)

$$C^{i}_{sam} = C^{i}_{rm} \times \left(\frac{cps^{i}_{sam}}{cps^{i}_{rm}}\right) \times \left\{\left(\frac{cps^{is}_{rm}}{cps^{is}_{sam}}\right) \times \left(\frac{C^{is}_{sam}}{C^{is}_{rm}}\right)\right\} \qquad \text{(eq. 1)}$$

where C^{i}_{sam} represents the concentration of i element in the sample, and C^{i}_{rm} the concentration of element "i" in the reference material. The cps^{i}_{sam} and cps^{i}_{rm} are net count rates of analyzed element "i" in the sample and reference material, respectively, while cps^{is}_{rm} and cps^{is}_{sam} are net count rates of internal standard of element "is" in the sample. The C^{is}_{sam} and C^{is}_{rm} are the concentrations of "is" in the sample and in reference material, respectively (Liu et al., 2008). Considering that:

$$k = \left(\frac{cps^{is}_{rm}}{cps^{is}_{sam}}\right) \times \left(\frac{C^{is}_{sam}}{C^{is}_{rm}}\right) \qquad \text{(eq. 2)}$$

the concentration of an element i in the sample is denoted by

$$C_{sam}^{i} = C_{rm}^{i} \times \left(\frac{cps_{sam}^{i}}{cps_{rm}^{i}}\right) \times k \qquad \text{(eq. 3)}$$

Based on the fact that the sum of all elements is represented by 100 wt%, the concentration of all species in the sample can be expressed as:

$$\left(\sum_{i=1}^{N} C_{sam}^{i} \times \frac{C_{rm}^{i}}{cps_{rm}^{i}}\right) \times k = 100 \qquad \text{(eq. 4)}$$

where N is the total number of elements in the sample and the value $\left(\frac{C_{rm}^{i}}{cps_{rm}^{i}}\right)$ can be calculated through regression statistics considering the analysis of reference materials, independently of an internal standard (Liu et al., 2008). The calculation of k represents a unique value and is denoted as the ablation yield correction factor (AYCF):

$$AYCF = \frac{100}{\sum_{j=1}^{N}\left[cps_{sam}^{j} \times \left(\frac{C_{rm}^{i}}{cps_{rm}^{i}}\right)\right]} \qquad \text{(eq. 5)}$$

Finally, the concentration of each element (C_{sam}^{is}) in the samples is calculated using:

$$C_{sam}^{i} = AYCF \times cps_{sam}^{i} \times l^{i} \qquad \text{(eq. 6)}$$

In addition to the mineralogical and trace element data of sinter samples, the chemical composition of nine geothermal spring water samples related to active sinter was determined. Separate samples for cations and anions were collected and filtered through a 0.45 µm cellulose acetate filter and stored in pre-cleaned polypropylene bottles. Samples for major cations and trace metal analyses were acidified with 0.65 ml (to 150 ml of water) of HNO_3 in a concentration of 4N. The samples were analyzed at the Fluid Geochemistry Laboratory at CEGA, Universidad de Chile, using atomic absorption spectrometry (AAS) for major cations, and ion chromatography (IC) for anions and bicarbonates. The trace element concentration of the geothermal water samples was analyzed using high resolution inductively coupled plasma – mass spectrometry (HR-ICP-MS) at Activation Laboratories Ltd (Actlabs), Canada.

3.4 Results

3.4.1 Sinter mineralogy and micro-morphology

The main mineralogical characteristics of the 37 sinter samples from Puchuldiza are listed in Table 1, including silica phases and accessory minerals. The FWHM value is also shown for each sample. Samples were classified as opal A, opal A/CT, opal CT, opal CT/C, and opal C/quartz according to their FWHM values and micro-morphologies (Lynne et al., 2007). Representative XRD traces for selected samples are shown in Figure 7.

Active and fossil silica sinter samples from Puchuldiza exhibit a wide range of FWHM values from amorphous to crystalline phases, between 0.11 and 9.52°2Θ (Table 1). Samples M1.2, M3.2a, P8a, M3.5v, and P8a show the highest FWHM values and correspond to amorphous opal A. Samples with FWHM values higher than 7 were classified as the same phase (e.g., samples M3.1, M3.6, M3.3r, P7a). FWHM values between 0.3 and 6.59°2Θ were measured in samples P7d, M3.7B, M3.5, M3.6b, M3.6d, M2.6b, P5, M2.2b, M2.2r, P3, and M2.5. In these samples, opal A/CT (4.3 - 6.59°2Θ), opal CT (1.6 - 2.51°2Θ), and opal CT/C (0.39 - 1.21°2Θ) phases were identified (Table 1). The most mature phases opal C/quartz were identified in samples M2.6r, M2.1, P1a and P1b, and show FWHM values of 0.11 - 0.28°2Θ.

The mineralogical contents and micro-morphologies are described for sinter samples as classified based on their constituent silica phases (opal A, opal A/CT, opal CT, opal CT/C, and opal C/quartz).

The Puchuldiza sinter samples are characterized by silica-bearing bands of variable coloration (e.g., Fig. 6 C,-E,-F,-G), although chemically pure silica is colorless (Rossman, 1994). The coloration is caused by chemical impurities in the silica and accessory minerals that co-precipitate with silica in sinter. The XRD patterns (Fig. 7 and Table 1) show halite (NaCl) as a common accessory mineral in all phases, and in amorphous and para-crystalline phases, detrital quartz was identified. Opal A phase-bearing samples (Fig. 7) contain hematite (Fe_2O_3) and magnetite (Fe_3O_4) in grey-red bands (samples M1.2, M3.2a, and M3.3r, M3.7p). Additionally, yellow-orange bands show realgar (As_4S_4) and native sulfur (e.g., samples M3.1, M3.1r and M3.1ar), while the pink coloration of sample M3.3r is related to orpiment (As_2S_3). The white color in opal A phases is mainly caused by the presence of calcite ($CaCO_3$) and detrital quartz

(samples M3.2a, M3.7 and M3.7a), even though some samples only display XRD patterns associated to amorphous silica. Opal A/CT phase-bearing samples show yellow and white coloration with only halite and detrital quartz as accessory minerals (e.g., in sample M3.5, opal A/CT-CT in Fig. 7). Opal CT, opal CT/C, and opal C/quartz-bearing samples (Fig. 7) display red, pink and yellow colors related to the co-existence of cinnabar (HgS) and halite (e.g., samples M2.6b, M2.2b, M2.2r, and M2.5). Some samples do not show accessory minerals as determined by XRD analyses, (e.g., M2.7m and P7c), although their coloration varies from white to different shades of white-pink, yellow, green, and red. This color variation is attributed to chemical impurities or nano-scale mineral inclusions in silica that were not detected by XRD techniques.

The micro-morphologies observed in sinter samples from Puchuldiza are highly variable and strongly correlate with the degree of crystallinity. Samples containing amorphous and para-crystalline silica phases display micro-spheres with variable sizes in different distributions. For example, opal A-bearing samples (22 samples) exhibit well-defined microspheres with diameters between 1 and 6 μm and smooth surfaces. The micro-spheres in these samples are distributed in honey comb (Fig. 8A), conglomerate and micro-botryoidal arrangements (Fig. 8B, -C); also, micro-spheres, occur on the surfaces of tubular microorganisms, forming smooth and rough filaments of ~10 and ~5 μm diameter, respectively (Figs. 8D, 9B). The filaments form a crisscross growth pattern without alignment resulting in a high porosity texture in the samples (e.g., samples M3.7b and M3.5v, Figs. 8D, 9B). Additionally, the silica micro-spheres are joined side by side or are interconnected in the botroydal arrangements filling the voids between filaments (Fig. 8D). In general, the silica micro-spheres exhibit a regular diameter in different samples (~1-6 μm), except for sample M1.2 which shows a coexistence of spheres of variable sizes (<1-5 μm), that are related to different formations stages (Fig. 8C). Samples M3.1ar, M2.7m, M3.1m, and M3.3 show platelets <5 μm that are distributed homogeneously in the samples and are intergrown with silica spheres (Fig. 9D, -C). SEM-EDS analyses suggest that platelets are composed of silica and show regular hexagonal shapes; irregularly shaped platelets usually display the smallest sizes and do not show any orientation. Samples M2.7m, M3.1, and M3.3 show a massive vitreous silica matrix between silica spheres or as massive bands (Fig. 9D); this silica precipitate is associated to late-stage precipitation of residual silica (Rodgers et al., 2004). Microorganisms such as diatoms and micro-algae were observed only in samples containing opal A silica. The microorganisms are usually associated with different aggregation of

micro-spheres and in some cases they preserve their morphological characteristics (Fig. 9A), while in other cases tubular microorganisms are covered by silica spheres (Figs. 8D, 9B). Microorganisms encrusted by spheres have been interpreted as they were present in the hot springs during silica precipitation (Herdianita et al., 2000).

Samples containing opal A/CT (samples P7d, M3.7b, and M3.5 in Table 1) display agglomeration of irregular micro-spheres of ~6-15 μm of diameter with rough surfaces and multiple clusters of filaments (Fig. 9B). For example, sample M3.7b shows a high porosity due to multiple filaments in a crisscross arrangement along with micro spheres of ~10 μm and irregular silica platelets of 5-20 μm, both recognized in the voids generated by inter-filaments gaps. Additionally, samples containing opal CT (samples M3.6b, M3.6d, M2.6b, P5, M2.2b, and M2.2r) and opal CT/C (samples P3 and M2.5) exhibit agglomerations of uniform silica spheres of 10-25 μm of diameter (Figs. 8E, -F, and Fig. 10A, -B), with roughness to lepi-surfaces along with silica platelets <10 μm that occur side by side with silica spheres. In sample M2.2r, micro-silica platelets <5 μm were observed with silica micro-spheres <1μm, both on the surfaces of lepi-spheres. The presence of these micro silica spheres is most likely associated with late-stage silica precipitation or colloidal transport in the hot water (Fig. 8F).

Sinter samples that contain the most mature silica phases (samples M2.6r, M2.1, P1a, P1b) show agglomeration of spheres of ~40-120 μm diameter with irregular surfaces. These irregular surfaces are formed by proto-crystals of quartz with sizes <10 μm, (Fig. 10C, -D), and well-developed microcrystals of quartz (10-30 μm) (Figs. 10E, -F). In sample M2.1, on the other hand, the micro-crystals were recognized mostly in micro-fractures and cavities within the sample. Well-developed quartz crystals usually occur inside voids, and do not show specific growth orientation.

Despite the fact that accessory minerals were detected by XRD (Table 1), the SEM inspection of samples did not allow a precise determination of their morphology, suggesting that these mineral species might be present as submicron-sized inclusions and/or are covered by layers of silica spheres or vitreous silica. The only exception is halite, which occurs as cubic crystals of 5-10 μm size in samples M2.5 and M3.1.

3.4.2 Sinter geochemistry and hydrothermal fluid composition

Representative LA-ICP-MS analyses of sinter samples from Puchuldiza are shown in Table 2, based on their degree of silica crystallinity, i.e., opal A, opal CT and opal C/quartz (all samples analyses are presented in the Appendix). Sinter samples contain more than 75 wt.% SiO_2, reaching a maximum of 95 wt.% in sample M3.7. CaO, Al_2O_3, Na_2O, K_2O, TiO_2, and Fe_2O_3 are present in all sinter samples and some MnO (samples M3.7, M3.6, M2.5 and M3.1) and MgO (samples M3.7, M3.6, and M2.5) were measured. The concentrations of CaO vary between 0.9 to 2.5 wt.%, with the highest value measured in sample M3.1. The Al_2O_3 show concentrations in the range of 0.08 to 0.63 wt.%, for samples M2.6r and M2.5, respectively. Na_2O is present between 0.06 and 0.73 wt.% and shows little variation, similarly to K_2O which is present in concentrations of 0.1 to 0.28 wt.% in samples M3.1 and M2.2r, respectively. Fe_2O_3 content was determined using ^{57}Fe, and show values between 0.11 wt.% in sample M3.7 and 3.7 wt.% in sample M2.2r. MnO and MgO show concentrations between 0.004 and 0.015 wt.% and from 0.004 to 0.014 wt.%, respectively.

Sinter samples contain high concentrations of metals and metalloids including Au, Ag, Cu, As, Sb, B and Li (Table 2). The less crystalline, more immature opal A-bearing sample M3.7 contains 0.23 ppm Au, 0.74 ppm Ag, and 21.62 ppm Cu. The other elements are present with a wide range of concentrations, i.e., As (133 - 10509 ppm), Sb (211 - 1007 ppm), B (328-3015 ppm), and Li (24-3015 ppm). Samples M3.6b is intermediate and less immature opal CT-bearing and contains a higher content of precious metals (9.63 ppm Au, 13.47 ppm Ag), and Cu (46.86 ppm). As, Sb, B and Li are present in relatively high concentrations (833.47 ppm, 274.12 ppm, 71.65 ppm, 65.649 ppm, respectively). The most mature and crystalline opal C/quartz-bearing samples (samples M2.2r, M2.5, M2.5b, M2.6r, and M2.6b) show the highest concentrations of Au (1.85-22.7 ppm), and Ag (9.3-46.3 ppm), whereas the other elements show variable concentrations (As: 9.1-2480 ppm, Sb: 339.27-1630.52 ppm, B: 58.55-606.77 ppm, Cu: 1.3-390 ppm, and Li 112-286 ppm).

In Figure 11, the mean and median concentrations of Au, Ag, Cu, As, Sb, and B are plotted as a function of silica crystallinity. In addition, a compilation of previously published LA-ICP-MS analyses from other sinter deposits around the world is shown as a reference, however no

silica crystallinity was reported for these data. These results reveal a significant correspondence between trace element concentrations and the degree of silica crystallinity. Gold and Ag show a trend of higher contents with increasing crystallinity, spanning two orders of magnitude in concentration from opal A to opal C/quartz. In contrast, As and B content show an inverse correspondence with silica crystallinity. Finally, the concentration of other species such as Sb and Cu do not show a clear trend with the crystallinity degree of silica, and their median values do not vary distinctly between different silica phases (Fig. 11).

The geothermal water related to the sinter deposits are NaCl-dominated with temperatures ranging between 54.4 and 87.8 ºC (the latter is the boiling T° at ~4.200 m a.s.l.), and pH varies between 6.2 and 8.8. The total dissolved solids (TDS) ranges from 4000 to 4500 mg/l, above the average of 3770 mg/l in geothermal springs from northern Chile (Tassi et al., 2010). Representative chemical analyses of major cations, anions and trace elements are shown in Table 3. The major constituents are SiO_2 (105-187 mg/l), Cl (2316-2616 mg/l), Na (1405-1625 mg/l), and K (144-218 mg/l), with B (73.9-88.6 mg/l), As (11.3-15.3 mg/l), and Li (10.6-12.9 mg/l) showing significant concentrations. Hg (0.0399-0.1 mg/l), Sb (0.0288-0.91 mg/l), and Cu (6.94-18.4 µg/l) also show high concentrations, and Au is present in low but measurable amounts (0.4-1.8 ng/l) (Table 3).

3.5Discussion

3.5.1 Silica precipitation and diagenetic maturation effects on trace element uptake

The siliceous sinter deposits at Puchuldiza record the complete diagenetic sequence from non-crystalline opal A to microcrystalline quartz, and the morphological changes observed here are similar to those described in other geothermal systems (Herdianita et al., 2000; Lynne et al., 2005; Lynne et al., 2007). These morphological changes (Figs. 8 to 10) are characterized by an increase in silica micro-particle abundance and variations in their size, shape and arrangement. Packed-in honeycombing (Fig. 8A), micro-botroydal clustering (Figs. 8 and 9), and sphere concatenation (Fig. 8D) causes continuous modification of the micro-surfaces and changes in the porosity of the siliceous sample. The multiple dispositions of silica micro-particles are the result of different mechanisms induced by self-assemblage processes and biological activity, which

control the directionality and growth of particle assembly (e.g., Jamtveit and Hammer, 2012; De Yoreo et al., 2015). These two mechanisms are more relevant in amorphous opal A and paracrystalline opal A/CT phases (Figs. 8A, -D), while agglomeration of micro-spheres and crystals in opal CT, opal C and opal C/quartz is the result of self-assemblage only (Figs. 8E, -D and Fig. 10). In spite of a complete diagenetic sequence reported in Puchuldiza, the coexistence of amorphous and mature silica phases is rare, and noted only in samples from proximal vent facies of sinter in active hot springs with periodic activity. A similar characteristic was described by Guidry and Chafetz (2003) in the same facies, and was attributed by the aforementioned authors to changes in the hydrodynamic activity of the thermal fluid source.

The geochemistry of the geothermal water and the formation of siliceous sinter are closely related, firstly by the degree of SiO_2 saturation that triggers silica precipitation, and secondly by other dissolved species and constituents in the hydrothermal fluid that may display a strong interaction with silica phases. There is consensus that the first silica phase that precipitates is opal A (Rodgers et al., 2004; Lynne et al., 2007; Orange et al., 2013), although the direct nucleation of more mature phases has been reported to occur in recent experimental studies of silica precipitation due to the variations in water chemistry (Okamoto et al., 2010; Saishu et al., 2012). Therefore, here we evaluate the potential effects of silica precipitation on the uptake of metals and metalloids, and the impact of post-depositional processes leading to trace element enrichment in the sinter.

During the first stages of sinter formation, the polymerization and subsequent coagulation/flocculation of colloidal silica particles form the amorphous opal A phase (Iler, 1979; Rimstidt and Cole, 1983; Buffle and Leppard, 1995; Herdianita et al., 2000; Smith et al., 2003; Tobler et al., 2009; Tobler and Benning, 2013). Apart from direct co-precipitation of accessory minerals, proposed mechanisms of elemental incorporation into sinter include isomorphous substitution and chemical adsorption on the surface of silica aggregates (Ichikuni, 1970; Nelson and Giles, 1985; Saunders, 1990; Pope et al., 2005; Kaasalainen and Stefánsson, 2012). During this initial stage, silica colloids may contribute to an increase in the trace element budget throughout adsorption on silica surfaces (Buffle and Leppard, 1995; Kersting et al., 1999; de Jonge et al., 2004; Kretzschmar and Schafer, 2005). This phenomenon has been described in shallow hydrothermal systems to explain the occurrence of nanoparticles of Au and Ag

(Saunders, 1990,1994; Pope et al., 2005; Hough et al., 2011). Following adsorption of metals on silica colloids, polymerization of SiO_2 leads to the formation of opal A on preexisting surfaces such as mineral grains and even microorganisms that are exposed to recirculation of thermal water (Kersting et al., 1999; Kretzschmar and Schafer, 2005; Lynne et al., 2007; Barnard and Guo, 2012; Cademartiri et al., 2012; Alsina et al., 2013). The absence of morphologies related to other minerals reinforces the idea that these species are present at the nano-scale and/or covered by silica precipitates (silica micro-spheres or vitreous silica). Additionally, previous studies have indicated that biological agents may enhance silica precipitation and thus metal adsorption, in particular Au (Jones et al., 2001; Konhauser et al., 2001; Yokoyama et al., 2004; Lalonde et al., 2005; Pancost et al., 2005; Phoenix et al., 2005).

Although microorganisms may influence metal precipitation, either as active agents during bio-mineralization or as passive agents during heterogeneous nucleation of silica, biological influences on metal uptake will not be discussed in detail here.

Environmental conditions have been reported to exert a strong influence on silica precipitation and texture development (Lynne, 2012a; Nicolau et al., 2014; Campbell et al., 2015), and thus may play a role on metal uptake during the early stages of sinter formation. The amorphous silica phases from the high-altitude Puchuldiza field (~4200 m a.s.l.) are characterized by some of the highest FWHM values reported in the literature (7-9.52 º2Ɵ), in agreement with previous values reported by Nicolau et al. (2014) at El Tatio (~4270 m a.s.l.). In Figure 12, the FWHM values of high-altitude sinters from Puchuldiza and El Tatio are compared with XRD data of sinters formed under different altitude conditions worldwide. The dataset include samples from Steamboat Spring and Roosevelt Hot Spring, both in the US, occurring at ~1400 m a.s.l and ~1840 m a.s.l., respectively, and from the Taupo Volcanic Zone, New Zealand (Te Kopia ~410 m a.s.l, Waiotapu ~380 m a.s.l, Orakei Korako ~350 m a.s.l., and Sinter Island ~320 m a.s.l.). The representative median values of FWHM for high-altitude sinters are above 9, while for sinter deposits at lower altitudes FWHM values are commonly below 9. Coincidently, the highest FWHM value (12.5º2Ɵ) corresponds to El Tatio sinter, which is located at the highest altitude, while the lowest FWHM value (6º2Ɵ) corresponds to Te Kopia that is located below 1000 m a.s.l. High FWHM values for amorphous opal A in sinter has been attributed to: (1) Incorporation of cations attached to silanol bonds (Si-OH) in the silica network that may distort

the crystalline setting (Ichikuni, 1970; Iler, 1979; Nicolau et al., 2014); (2) Incorporation of nano-minerals or mineral nano-particles within the silica matrix (Garcia-Valles et al., 2008), and (3) Extreme environmental conditions typical of high-altitude systems, e.g., lower boiling point of thermal water, high evaporation rates and extreme fluctuations in daily temperatures. Therefore, the influence of these factors on silica precipitation and metal partition are yet to be explored and further studies including laboratory and in situ precipitation experiments are needed.

Once silica is precipitated and accumulated to form sinter deposits, chemical diffusion processes play an important role during structural ordering triggered by diagenesis. Amorphous and para-crystalline phases have been described as open and distorted structures (e.g., opal A) that progressively order to become mature phases (Lynne and Campbell, 2004; Hinman and Walter, 2005; Lynne et al., 2007; Okamoto et al., 2010). Crystallographic defects and structural distortions of silica allow the accommodation of impurities such as (nanoscale) accessory minerals and/or ions adsorbed as cationic hydroxyl or chloride species complexes on the silica surfaces (Rossman, 1994; El-Ammouri, 2000; Veith et al., 2009; Dal Martello, 2012; Lynne, 2012b; Mohammadnejad et al., 2013). Previous studies have documented impurities in silica, including precious metals and Cu, in the form of nano-scale mineral inclusions, liquid-like inclusions and trace elements in crystalline silica phases such as quartz (e.g., Lehmann and Bambauerp, 1973; Iler, 1979; Götze et al., 2004 and references in there). During diagenesis, silica phases undergo different morphological and crystallographic modifications, including significant structural rearrangement. This process triggers the formation of structural vacancies that become available sites for diffusion of different chemical species (Dal Martello, 2012). Furthermore, cation diffusion during diagenesis may occur along grain boundaries, between phases or on the surface of micro-particles that are exposed to recirculation of thermal water, leading to fluid-mineral exchange (Dal Martello et al., 2012). Additionally, the diagenetic rate represents another factor that influences elemental mobility in sinter through retardation or acceleration of phase transitions, resulting in a modification of diffusion pathways producing a slow or fast diffusion through the silica matrix (Dal Martello et al., 2013). Therefore, a reasonable mechanism to explain metal enrichment in sinter may be the result of diffusion-driven processes triggered by structural changes from opal A to quartz influenced by diagenesis. These changes would involve a crystallographic or structural refinement where, e.g., precious metals such as Au and Ag that

may be present in silica as adsorbed/absorbed species or as mineral nano-particles, are later remobilized, accommodated and re-concentrated as diagenesis progresses.

3.5.2 Trace metal and metalloid enrichment of silica phases in sinter

Our LA-ICP-MS results indicate that the concentration of trace metals (Au, Ag, Cu) and metalloids (As, Sb, B) is correlated with the crystallinity degree of silica phases in sinter (Fig. 11). While Au and Ag are enriched in the more crystalline phases (opal C/quartz), arsenic and B concentrate preferentially in amorphous phases (opal A). These findings indicate that the diagenetic transitions of silica in sinter deposits, defined by significant structural (Fig. 7) and morphological (Figs. 8 to 10) changes, may play an important role on metal and metalloid enrichment in siliceous sinters and also influence their budget of accessory mineral components. At Puchuldiza, samples containing amorphous opal A display the highest variability in accessory mineral occurrence; these samples contain realgar, hematite, and native sulfur, along with other detrital minerals derived from surrounding rocks such as anorthite and quartz (Fig. 7). Considering the fact that opal A is the first silica phase to precipitate from thermal water, we interpret this variability as a result of changes in the hydrogeochemistry of the active spring, where As, S and Fe-bearing accessory minerals co-precipitate from metal-rich thermal waters along with opal A. In contrast, more mature sinters dominated by opal C and opal C/quartz show lower variability in their accessory mineral content; these samples contain, for example, Hg minerals (e.g. cinnabar) that are absent from opal-A bearing samples

The low concentration of Au and Ag in opal A and opal A/CT at Puchuldiza coincides with the formation of silica laminations associated with precipitation of residual silica. These features are similar to those reported by Herdianita et al., (2000), who proposed that precious metals usually occur in low concentrations in this type of residual silica. The precipitation of residual silica is due to steam condensate and could be related to local variation in the water table of the springs that feed the active sinter (Rodgers et al., 2004; Lynne et al., 2008). Therefore, we interpret the increase in concentration of Au (and Ag) with increased silica crystallinity as a result of post-depositional enrichment. During sinter diagenesis the continuous crystallinity and morphological changes promote the destabilization of silica surfaces by mechano-chemical processes, triggering the generation of surface defects and the creation of siloxyl ($\equiv Si - O \bullet$) and

silyl ($\equiv Si\bullet$) reactive sites (or surface free radicals) (Mohammadnejad et al., 2013). These surface defects possess a high chemical activity and have been widely studied due to their high capacity to capture and favor the nucleation of metal clusters such as Au and Ag (Ferullo et al., 2006; Shor et al., 2010). The reaction below shows the formation of surface radicals by the breakage of covalent siloxane bonds after activation of the silica surface:

$$\equiv Si - O - \equiv Si \Rightarrow \equiv Si\cdot + \equiv Si - O\cdot \qquad \text{(eq. 7)}$$

Mohammadnejad et al. (2013) proposed a mechanism of fixation and stabilization of Au on silica based on the interaction of silica free radicals and Au transported in the fluid. In this model, the Au-chloride complexes in the hydrothermal fluid are electrostatically attracted to the active sites formed on the silica surface, and then chemically adsorbed on defect sites by substitution of the chloride ligand by a surface silanol. Finally, the adsorbed Au is reduced from Au^{3+} to metallic Au^0 and stabilized on the silica surface by free radical silica groups, according to:

$$\equiv Si - O\bullet + 2Au^{3+} + 3H_2O \Rightarrow 2Au^0 + 3O_2 + 6H^+ + 3 \equiv Si - O - Si \equiv \text{(eq. 8)}$$

$$\equiv Si\bullet + 2Au^{3+} + 3H_2O \Rightarrow 2Au^0 + 6H^+ + 3 \equiv Si - O - Si \equiv \qquad \text{(eq. 9)}$$

Equation 8 is more suitable to describe the reduction of Au on defect sites of the silica surface, due to the lower activity of $\equiv Si - O\bullet$, which has a higher chance to react with Au-chloride complexes in comparison to $\equiv Si\bullet$, that react mainly with the environment (Mohammadnejad et al., 2013). Once Au (and Ag) are incorporated to the silica surfaces, the once dispersed nano-particles or metal clusters are embedded by silica to be later agglomerated into larger particles via Ostwald ripening during sinter diagenesis, as previously shown to support the growth of silica micro-particles in sinter formation (Rodgers et al., 2004; Wen Low et al., 2006; Tobler et al., 2009; Mohammadnejad et al., 2013; Cassano et al., 2014). The continuous agglomeration of nanoparticles of native Au (and Ag) in mature phases (opal C/quartz) causes the formation of sub-micrometer-sized inclusions of Au-Ag. Sub-micrometer-sized inclusions of native Au were detected in mature silica phases from Puchuldiza during laser ablation analysis (sample M2.6r, Fig. 13). Figure 13A shows a LA-ICP-MS profile across a sinter grain that is representative for homogeneous or structurally-bound incorporation of Au and Ag in sinter

(sample M2.6r). In contrast, the numerous spikes in the signal shown in Figure 13B are indicative of ablation of nano-particulate inclusions of Au and Ag in sample M2.6r. Although high-resolution images of these particles are not presented here, similar inclusions in sinter have been previously reported and imaged by Wen Lou et al. (2006) and Cassano et al. (2014) using HR-TEM, where larger Au nanoparticles form by Ostwald ripening of smaller particles in a silica microspace (Wen Lou et al., 2006). Therefore, the highest Au and Ag concentrations detected in the more mature sinter phases (opal C/quartz in Fig. 11) at Puchuldiza are most likely related to the presence of nano-inclusions of native metals rather than structural incorporation of cationic species in quartz (Fig. 14). In quartz, trace impurities occur in vacancies, crystal defects and substitutional or interstitial positions parallel to the c-axis. However, this mineral phase has a low tolerance to incorporate foreign elements (Dal Martello, 2012). Therefore, it is likely that at least some of the Au and Ag detected in quartz in the Puchuldiza samples may reside within the crystal structure, as a result of preferential retention during diagenesis and/or late-stage diffusion (Shor et al., 2010). It is noteworthy to mention that our data show that Au and As are geochemically decoupled in sinter samples from Puchuldiza, showing opposite concentration trends with respect to silica crystallinity (Fig. 11). This geochemical behavior is different to the widely documented correspondence between Au and As that has been previously reported in pyrite and other sulfides from a wide range of hydrothermal ore deposits (Reich et al., 2005; Deditius et al., 2014 and references therein), and suggest that Au enrichment in the siliceous sinter at Puchuldiza is not controlled by As-bearing sulfide minerals.

Unlike precious metals, metalloids (As and B) show a decreasing trend with increasing crystallinity of silica (Fig. 11). The increased concentration of As in the more amorphous silica phases (opal A) is most likely related to the occurrence of As-bearing accessory minerals hosted in the sinter, i.e., realgar and Fe-oxyhydroxides (Fig. 14B, -D; Table 1). Previous studies have shown that As is preferably removed from water by adsorption on Fe-oxyhydroxides and on amorphous Fe oxides forming chemisorbed surface complexes. These processes have been reported in the El Tatio geothermal field (Zeng, 2004; Smith and Edwards, 2005; Landrum et al., 2009; Alsina et al., 2013; Nair et al., 2014; Bisone et al., 2016). The incorporation occurs only in the first step of sinter formation when the surfaces of accessory minerals are available (Fig. 14D). Post-depositional processes in sinter continuously coat the active surfaces of accessory minerals with silica, inhibiting the incorporation of As (Swedlund and Webster, 1999). Additionally, the

low capacity of silica to adsorb As and its poor tolerance to hold this element within the structure contributes to the observed decrease of As concentrations in the more mature phases of silica (Smith and Edwards, 2005; Landrum et al., 2009; Nair et al., 2014). This behavior is consistent with reports by Swedlund and Webster (1999) showing that silica directly inhibits As adsorption into Fe bearing minerals at the Wairakei Geothermal Power Station, New Zealand.

It is likely that chemical species that are not enriched in the more crystalline phases (i.e., As and B) may have been lost from the silica matrix to the thermal fluid, during structural rearrangement. For example, Ichikuni (1970) proposed that B concentrations in sinter decrease during diagenesis due to crystallographic changes related to dehydration. According to the cited study, boron is incorporated into amorphous opal A by adsorption of $B(OH)^-_4$ species during silica precipitation. Further diagenetic changes would trigger B migration into the aqueous solution, leading to the observed inverse correspondence with silica crystallinity. This interpretation is in good agreement with our data where B (and also As) are preferentially enriched in the more amorphous phases (Fig. 11). This is also consistent with the fact that no B-bearing minerals were recognized at Puchuldiza, unlike El Tatio where the arsenic borate cahnite ($Ca_4B_2As_2O_{12}*4H_2O$) was reported in sinter samples (Nicolau et al., 2014).

Finally, the variable concentrations of Sb and Cu in silica, as seen in Figure 11, are indicative that these two elements are concentrated during the first stages of silica precipitation, and do not suffer significant alterations during silica maturation. The behavior of Sb has been previously studied in the sinter deposits of El Tatio by Landrum et al. (2009), suggesting that this element partitions mainly to the opal silica matrix and co-precipitates with $Si(OH)_4$ due to the similar saturation conditions, especially as cervantite (Sb_2O_4). Variations in saturation of Sb with respect to different Sb-bearing phases such as cervantite may be the result of local temperature variations triggering the formation of silica bands enriched in nano-particles of Sb oxide minerals. In the case of Cu, its incorporation into silica phases may be similar to Au and Ag, with strong interactions due to adsorption of $Cu(OH)^+$ species on to silica surfaces defects (El-Ammouri, 2000; Ferullo et al., 2006; Shor et al., 2010). However, occurrence of Cu in sinter reported here is likely related to cryptocrystalline inclusions of Cu-bearing minerals such as chrysocolla in different silica phases (Crane et al., 2001), and the low concentration is related to its preferential co-precipitation with sulfides at the subsurface from an alkaline and boiling

geothermal water (El-Ammouri, 2000; Kaasalainen and Stefánsson, 2012; Kaasalainen et al., 2015).

It is relevant to note that the precious metal and metalloid budget of sinters from Puchuldiza are within the same range of other sinter deposits worldwide (Fig. 11). In general, As, Sb, B, and Cu display high concentrations in amorphous silica phases from sinter deposits in Puchuldiza, El Tatio, Waiotapu, and Champagne Pool (Fig.11). The amorphous opal A phase in these deposits show high to very high FWHM values, suggesting that low degrees of structural maturation generally correlated with high metalloid enrichment in sinter. In contrast, the more mature silica phases from Puchuldiza and from the Jurassic paleo-sinter of El Deseado Massif (Fig. 11) are characterized by higher concentrations of Au and Ag, although the immature silica phases at Waiotapu exhibit the same concentration range (Fig. 11). These observations suggest that, in general, mature sinter deposits host higher concentrations of precious metals such as Au and Ag, whereas metalloids such as As, Sb, and B are mainly concentrated in sinters dominated by immature phases of silica.

3.6 Summary and concluding remarks

This work reports a comprehensive mineralogical and geochemical characterization of the metal-rich siliceous sinter deposits of Puchuldiza, in northern Chile, where the complete diagenetic sequence – i.e., amorphous opal A, paracrystalline opal A/CT, opal CT, opal C, and microcrystalline quartz – is present. The sinter deposits contain significant amounts of metals (e.g., Au, Ag, Cu) and metalloids (e.g., As, Sb, B) that are associated with different silica phases pointing to a relevant role of the degree of silica crystallinity on elemental enrichment in sinters.

Combined SEM, XRD and LA-ICP-MS data show that the concentration of metals and metalloids in sinters display a strong correspondence with silica crystallinity (Fig. 11). Arsenic and B are predominantly enriched in the more amorphous phases (opal A/CT), while Au and Ag show higher concentrations in the more crystalline phases (opal C/quartz). We interpret this differential enrichment as the result of structural, morphological and geochemical changes produced by silica maturation during sinter diagenesis.

During the first stages of sinter formation, crystallographic transition promote the generation of surface defects on silica by mechano-chemical processes, creating reactive sites where Au and Ag are electrostatically attracted and chemisorbed (Ferullo et al., 2006; Shor et al., 2010; Mohammadnejad et al., 2013). As diagenesis progresses, the generation of structural vacancies triggers the diffusion of chemical species incorporated into the less crystalline silica phases. The continuous structural changes occurring during diagenesis (Fig. 11) may promote the agglomeration of adsorbed species and embedded metal clusters through Ostwald ripening (Fig. 14), leading to the formation of nano-to micron-sized inclusions of precious metals (Fig. 13). Metalloids such as As exhibit an opposite geochemical behavior. Owing to the low capacity of silica phases to adsorb and retain arsenic, its enrichment in the more amorphous phases is most likely due to co-precipitation of As-bearing accessory minerals (e.g., realgar, orpiment) and Fe-oxyhydroxides that efficiently adsorb arsenic (Fig. 14). As a result of structural rearrangements during diagenesis, As (and B) are desorbed from the silica matrix, contributing to a progressive decrease of As in the more mature phases of silica. Finally, other enriched elements such as Sb and Cu are incorporated during in the first stages of sinter formation and their concentrations do not vary significantly during maturation, although Cu concentrations significantly decrease in the more crystalline phases.

Although these trends strongly support the role of silica crystallinity and structural maturation on metal/metalloid enrichment in sinter, further experimental and field studies are needed to fully understand the elemental partitioning behavior between silica and geothermal fluids as they discharge and cool at the surface. Among other aspects, colloidal transport of precious metals in geothermal fluids (Hannington et al., 2016), and the potential effects of microorganisms on metal fixation and nano-particle formation (Johnson et al., 2013) must be addressed. Finally, and considering the highly amorphous character of opal A in high-altitude systems such as Puchuldiza and El Tatio (Fig. 12), results from this study confirm that environmental conditions can have an unforeseen impact on silica precipitation, and thus may impact the metal/metalloid tenor of sinter deposits.

3.7Acknowledgements

We acknowledge FONDAP-CONICYT project 15090013 “Andean Geothermal Centre of Excellence (CEGA)” for providing financial support to carry out this research, that included a M.Sc scholarship. We also acknowledge support from FONDECYT project 1130030 and FONDEQUIP EQM120098. The Millennium Nucleus for Metal Tracing Along Subduction (NMTM), MSI Grant NC130065 provided additional support to fund this study.

Tables

Tabla 1 Mineralogical features of silica sinters from Puchuldiza. The FWHM values and the corresponding structural classification are provided, along with a general macroscopic description and location information. Accessory mineralogy is described for each sample.

Sample ID	FWHM (°2Θ)	Silica Phase	Other constituents
M1.2	9,52	Opal A	Detrital quartz and hematite. Pool margin from sample Site 4.
M3.2a	8,9	Opal A	Hematite, calcite, halite, and organic material. Pool margin from Site 2.
P8a	8,57	Opal A	Paleo sinter with laminations (Fig 6 E). Yellow level. Site 13.
M3.5v	8,5	Opal A	Halite and silica spheres encrusted on microorganisms filaments. Site 10.
M3.1a	8,33	Opal A	Halite and microorganisms. Pool margin from Site 1.
M3.1ar	8,3	Opal A	Realgar, sulfur, halite and microorganisms. Site 1.
M3.3	8,31	Opal A	Halite. From pool margin in sinter mound from Site 3.
M3.1	8,2	Opal A	Quartz, anorthite, halite and microorganisms. Site 1.
P8b	7,97	Opal A	Paleo sinter with sinter laminations (Fig 6 E). Brown level. Site 13.
P7b	7,95	Opal A	Paleo sinter with sinter laminations (Fig 6 E). Red level. Site 13.

M3.7v	7,77	Opal A	Calcite, albite, halite, quartz and organic matter. Site 11.
P7e	7,75	Opal A	Paleo sinter with sinter laminations (Fig 6 E). Orange level. Site 13.
M3.1.r	7,58	Opal A	Halite in pool margin. Site 1.
P7a	7,75	Opal A	Paleo sinter with sinter laminations (Fig 6 E). Orange-yellow level. Site 13.
P7c	7,7	Opal A	Paleo sinter with sinter laminations (Fig 6 E). White-yellow level. Site 13.
M3.7	7,56	Opal A	Calcite. Site 11.
M2.7m	7,5	Opal A	Sample from Site 5.
M3.3r	7,5	Opal A	Sample from Site 3 with organic matter.
M3.6	7,5	Opal A	Halite in Site 12.
P8c	7,29	Opal A	Paleo sinter with sinter laminations (Fig 6 E). Red-pink level. Site 13.
M3.7p	7,2	Opal A	Halite, hematite, magnetite and organic matter. Site 11.
M3.1	7	Opal A	Realgar, halite and high presence of microorganisms. Site 1.
P7d	6,59	Opal A/CT	Paleo sinter with sinter laminations (Fig 6 E). White level. Site 13.
M3.7b	5,68	Opal A/CT	Sample from site 11.
M3.5	4,3	Opal A/CT	Quartz and halite, from Site 10.
M3.6b	2,51	Opal CT	Diffractogram with tridymite-like peaks, from Site 12.
M3.6D	2,5	Opal CT	Diffractogram with tridymite-like peaks and quartz, from Site 12.
M2.6B	1,96	Opal CT	Cinnabar, halite and cristobalite-like peaks. Site 6.
P5	1,7	Opal CT	Sample from Site 13.

M2.2b	1,66	Opal CT	Cinnabar, halite and tridymite-like peaks, in white level, from Site 8.
M2.2r	1,6	Opal CT	Cinnabar, halite and tridymite-like peaks, in red level, from Site 8.
P3	1,21	Opal CT/C	Paleo sinter with quartz and cristobalite-like peaks. Site 13
M2.5	0,39	Opal CT/C	Quartz, cinnabar and cristobalite-like peaks. Site 7.
M2.6r	0,28	Opal C/ Quartz	Quartz, cinnabar and cristobalite-like peaks. Site 6.
M2.1	0,25	Opal C/ Quartz	Quartz, in Site 9.
P1a	0,15	Opal C/ Quartz	Paleo sinter with quartz, from red level in Site 13.
P1b	0,11	Opal C/ Quartz	Paleo sinter with quartz, from white level in Site 13.

Tabla 2. Selected trace elements analyses of different silica phases determined by LA-ICP-MS. Concentration are in ppm unless specified otherwise.

	Silica Phases							
	Opal A		Opal CT	Opal C/quartz				
	M3.1	M3.7	M3.6b	M2.2r	M2.5	M2.5b	M2.6r	M2.6b
SiO_2 (wt%)	89,98	95,82	89,01	88,25	79,54	76,73	87,04	86,91
CaO (wt%)	2,521	0,625	0,91	2,082	5,926	3,951	3,196	3,183
Al_2O_3	1102,98	4200,67	2428,52	432,1	11887,25	5620,97	930,98	889,9
Na_2O	7346,39	2843,91	689,21	2496,14	2543,51	3942,34	3459,51	3591,31
K_2O	1014,99	2541,61	1169,5	2806,61	2564,21	2761,37	2633,83	2752,7
MnO	22,19	158,36	44,64	n.d	141,6	n.d	25,58	n.d
TiO_2	11,93	198,09	340,6	525,21	164,93	2669,52	679,02	438,52
MgO	n.d	148,02	40	n.d	94,67	n.d	n.d	n.d
Au	n.d	0,25	8,59	20,26	30,58	1,86	19,06	n.d
Ag	n.d	0,75	13,5	46,3	9,3	n.d	111,9	n.d
Cu	n.d	21,63	45,82	0,3	157,27	14,82	129,08	1,01
As	22996,22	133,52	2469,28	19,95	452,79	101,28	54,9	31,12
Sb	371,88	1007,24	267,26	345,14	295,79	1583,5	435,06	1466,45
B	994,78	3015,66	328,07	75,2	606,78	88,89	84,3	103,16
Li	1,22	83,46	61,13	n.d	112,04	n.d	23,2	n.d

Tabla 3. Geochemistry of thermal water. The temperatures are in ºC and concentrations in ppm, unless specified otherwise.

	Site 1	Site 2	Site 3	Site 4	Site 5	Site 6	Site 7	Site 11	Site 12
T	54,4	87,8	78,7	75,4	84	82,3	81,2	86	74,5
pH	6,2	8,8	7,5	7,8	8,2	8	8,3	7,4	8,2
SiO_2	106	135	161	187	110	182	172	167	178
F^-	3,3	3,3	4,49	3,79	3,47	3,84	4,02	3,63	3,83
Cl^-	2389	2413	2442	2542	2316	2563	2616	2504	2519
Br^-	4,27	4,45	4,43	6,85	6,79	7,38	7,58	6,91	7,31
NO_3^-	0,88	1,04	0	0,79	0	0	0	0,62	0
SO_4^{2-}	131	133	134	141	125	144	143	137	148
HCO_3^-	205,01	168,4	46,37	231,86	195,25	144	154,25	118,37	231,86
Na	1425	1455	1405	1580	1425	1570	1625	1520	1570
K	144	150	183	213	176	209	218	202	211
Ca	53,7	36,8	22,5	39,7	29,9	24,4	23,1	14,5	50,6
Mg	2,32	1,42	0,46	0,99	0,84	0,57	0,64	0,23	1,08
Au (ppt)	0,6	0,5	0,6	0,9	1,8	0,4	1,3	1,6	1,6
Cu	n.d	n.d	n.d	n.d	0,0069	n.d	0,018	n.d	n.d
Al	3,15	0,07	0,062	0,114	0,298	0,41	0,097	0,162	0,176
As	10,7	11	11,3	12,9	12,5	12,9	13	12,8	12,4
B	75,8	76,4	77,8	84,9	73,9	84,9	88,6	84,1	85,7
Sb	0,028	0,54	0,665	0,71	0,91	0,817	0,879	0,637	0,533
Hg	0,039	0,045	0,1	0,065	0,052	0,063	0,069	0,059	0,061
Li	10,9	10,7	10,6	12,6	11	12,3	12,9	12	12,4
Mn	0,664	0,225	0,072	0,141	0,122	0,015	0,016	0,024	0,218
Pb (ppb)	0,05	0,05	0,05	0,05	1,66	0,05	0,05	0,05	0,05
Sr	2,6	2,62	1,91	2,68	2,35	2,32	2,57	2,34	2,89
Cs	2,24	2,49	3,26	2,86	2,5	2,95	2,99	2,79	2,83
Ba	0,178	0,167	0,134	0,286	0,279	0,246	0,276	0,225	0,274

Figures and captions

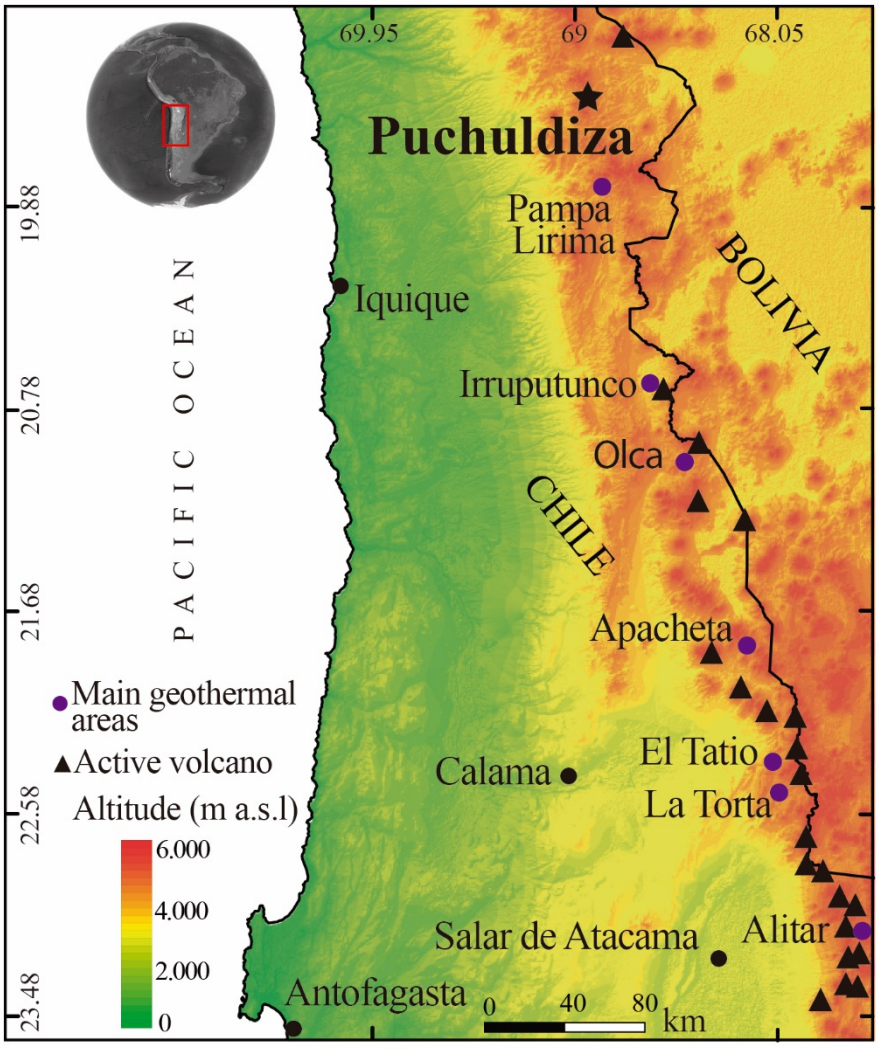

Figura 5. Location map of the Puchuldiza geothermal field in the Altiplano of northern Chile. Other geothermal areas are shown (purple circles), as well as active volcanoes (black triangles). Figure modified from Nicolau et al. (2014) and Aravena et al. (2016).

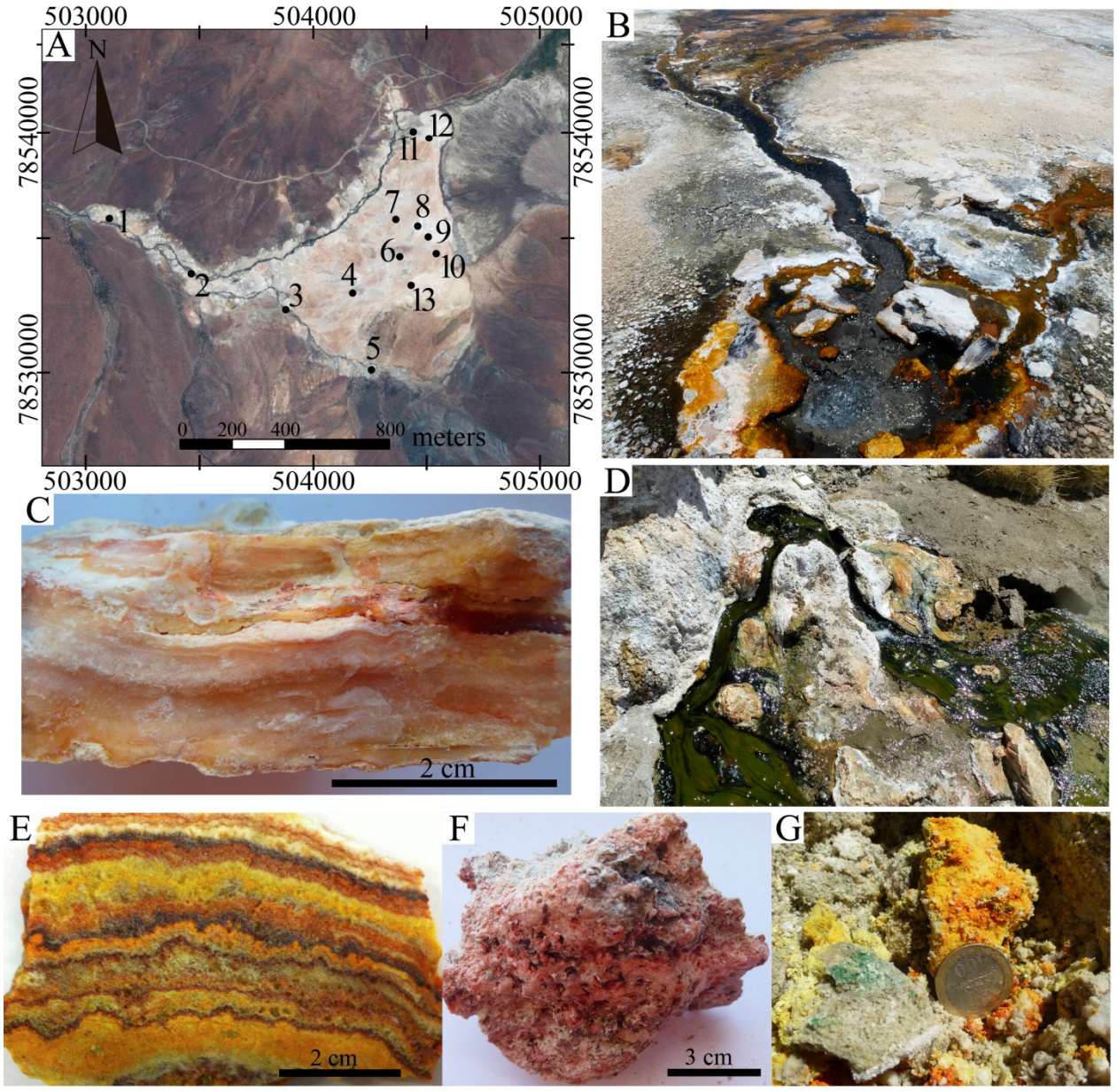

Figura 6. (A) Location of the 13 sinter sampling sites, distributed throughout the Puchuldiza field. (B and D) Sample sites of active sinter related to bubbling pools. The pool in B has ~1 m diameter in sampling site 7 and in D the pool has ~0.3 m, with discharge channels and temperatures of 84°C and 54°C, respectively. (C and E) Paleo-sinter samples showing bands and red nodules (sampling site 9) and multiple color bands (site 13, E). (F and G): Active sinter samples showing high porosity (site 6, F) and nodules of a sulfide precipitate (site 11, G).

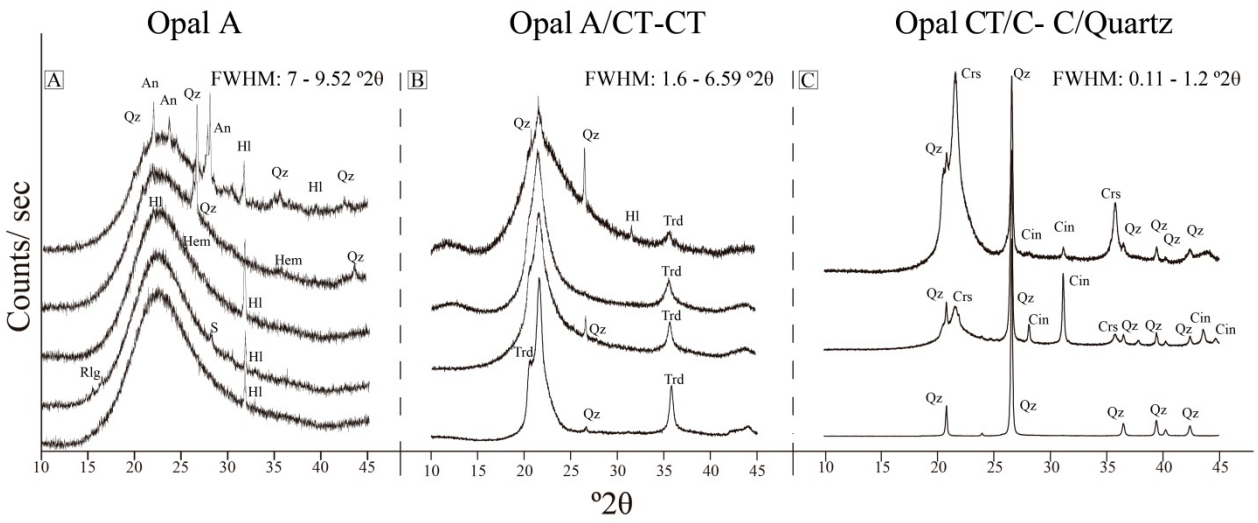

Figura 7. Representative X-ray diffractogram traces of sinter samples from the Puchuldiza. (A) Stack of 5 diffractograms of opal A- bearing samples: the broadband is centered at 23.5-24 °2Θ, with FWHM values between 7- and -9.5°2Θ. (B) Stack of 4 diffractograms of paracrystalline opal A/CT – CT-bearing samples: the broadband in centered at ~21.5°2Θ, and FWHM values vary between 1.6 and 6.59°2Θ. (C) Stack of 3 diffractograms of opal CT/C-C/quartz: the well-defined peaks of quartz are representative of high crystallinity degree. Main accessory minerals phases are labeled and correspond to anorthite (An), hematite (Hem), realgar (Rlg), halite (Hl), detrital quartz (Qz), cinnabar (Cin), native sulphur (S), trydimite (Trd) and cristobalite (Crd).

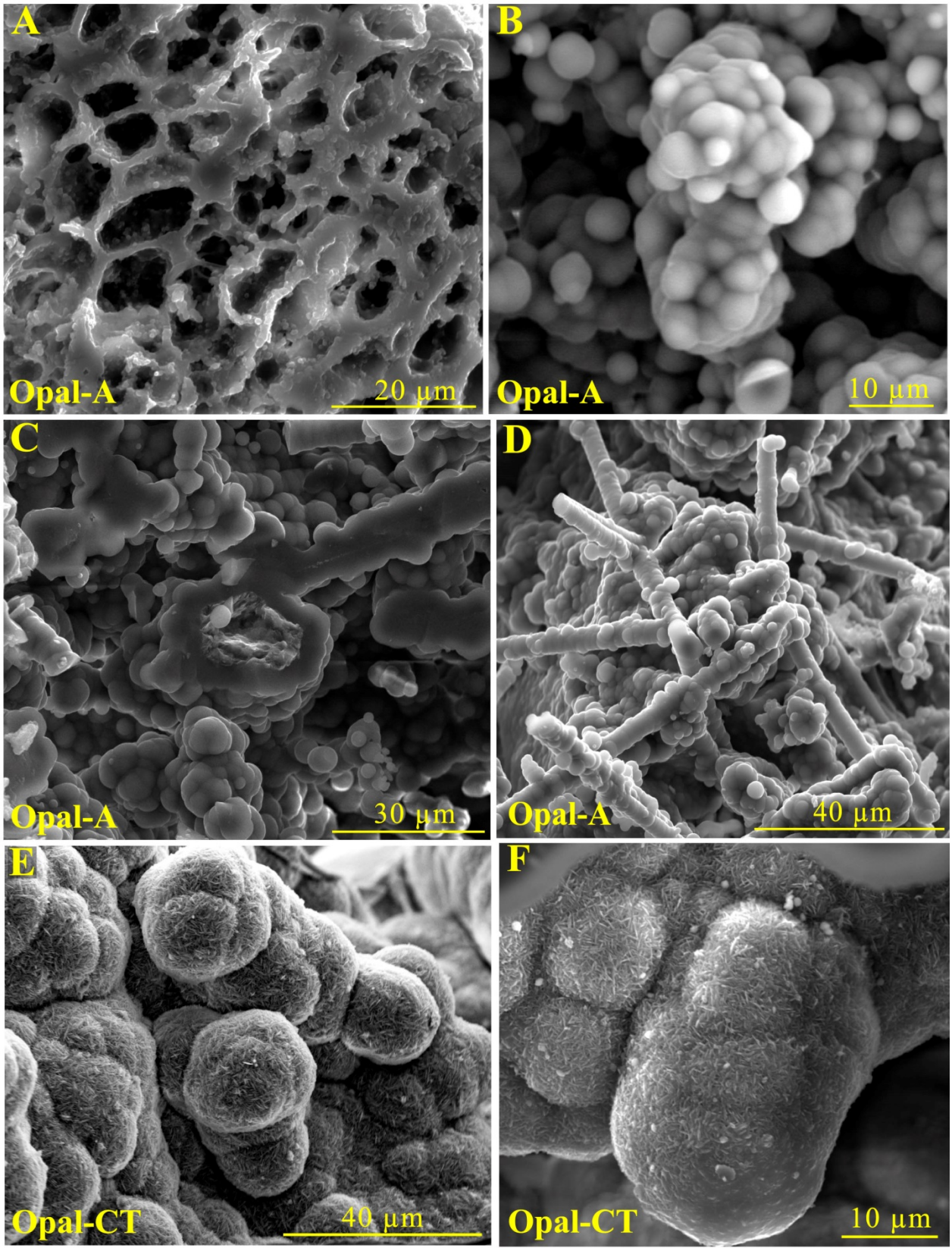

Figura 8. Morphology and micro-textures of amorphous silica phases in sinters form Puchuldiza. (A) Opal A micro-spheres (1-4 µm) forming a honey-comb arrangement. (B) Micro-botroidal

arrangement of opal A spheres of diameter ~4-5 μm (C) Agglomeration and packs of aligned opal A micro-spheres (2-6 μm), showing a fracture surface. (D) Opal A micro-spheres aligned in tubular rows as filaments. (E) Agglomeration of opal-CT micro-spheres ~6-15 μm diameter, showing lepispheres with roughness surfaces. (F) Opal-CT lepispheres and micro-particles encrusted between silica platelets on larger micro-spheres.

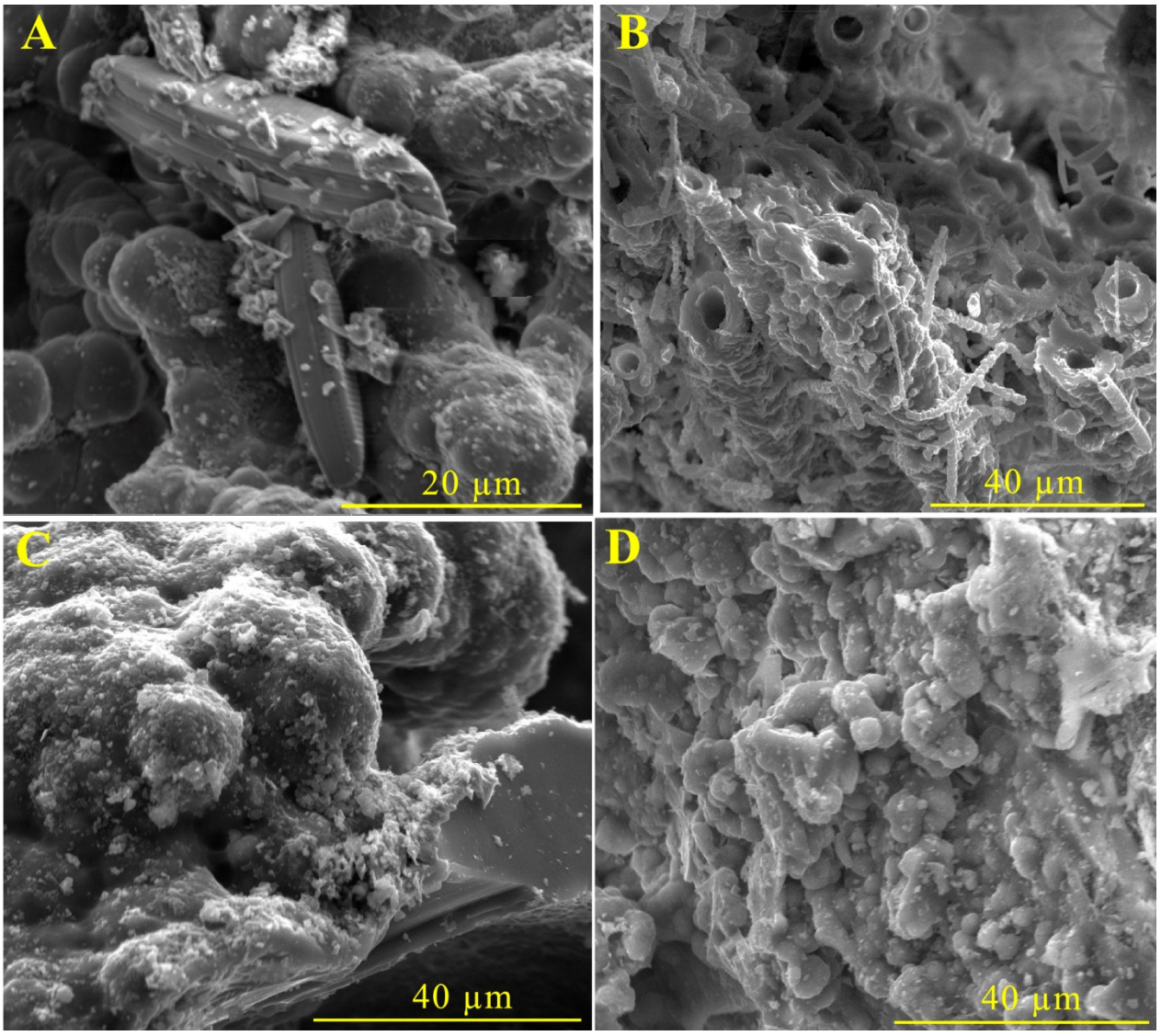

Figura 9. Morphology and micro-textures and microbial components of the Puchuldiza sinters. (A) Microorganisms between microspheres of opal A show well-defined forms and display silica platelets on their surfaces. (B) Tubular microorganisms with micro-spheres of opal A encrusted on the surface. (C) Micro-spheres show rough surfaces due to large amounts of silica platelets.

An amorphous silica band can be observed at the bottom. (D) Micro-spheres and silica platelets form conglomerates of different sizes.

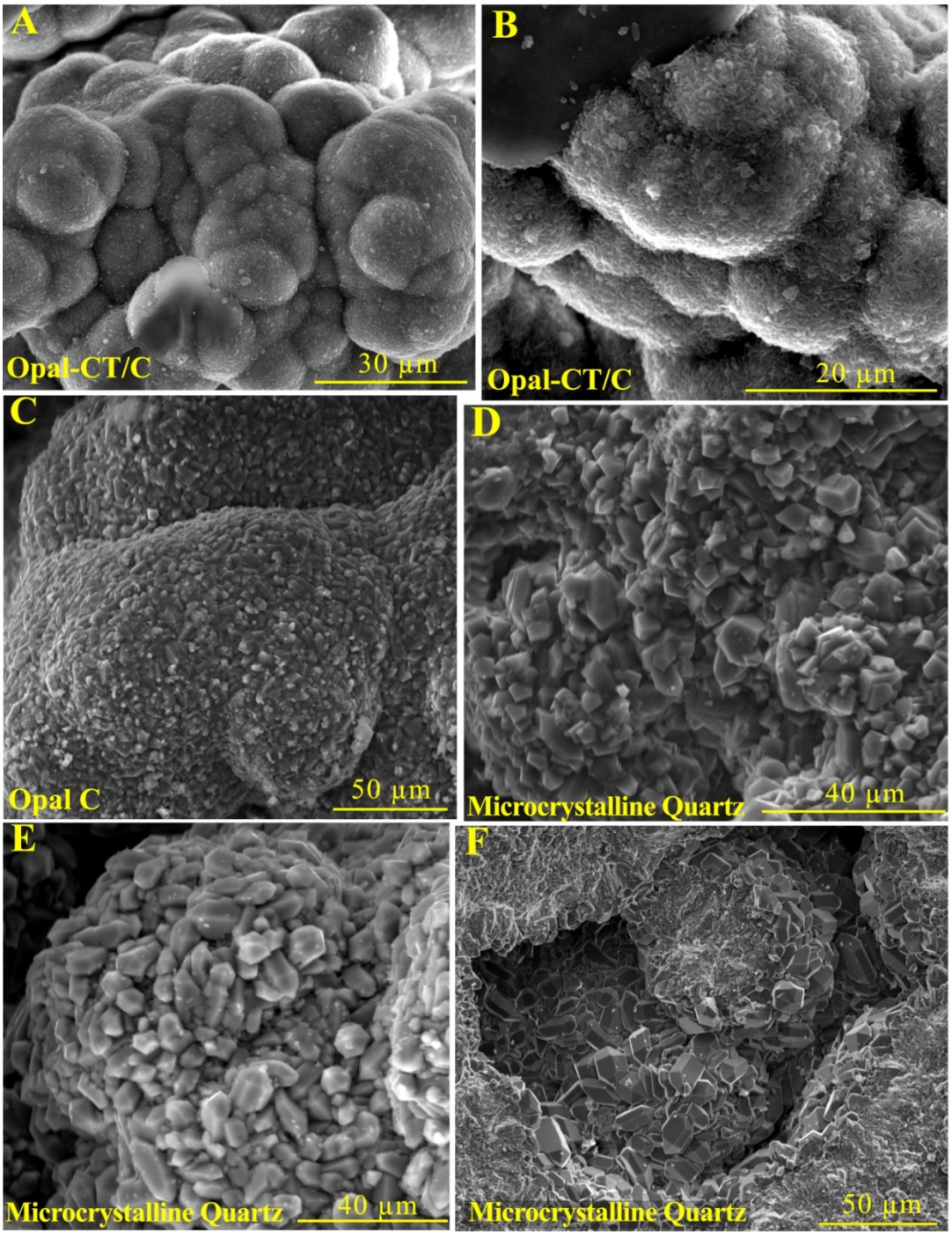

Figura 10. Morphology and micro-textures of the more crystalline silica phases in sinters from Puchuldiza. (A) Agglomeration of opal C micro-spheres with rough surfaces. (B) Agglomerated micro-spheres of opal-CT/C with quartz pseudo-microcrystals on the surface. (C) Typical

morphology of opal C micro-spheres in sinter. (D) Quartz microcrystals with prismatic faces. (E) Microcrystals of quartz on the surface of a micro-sphere. (F) Well-defined bipyramidal microcrystals of quartz.

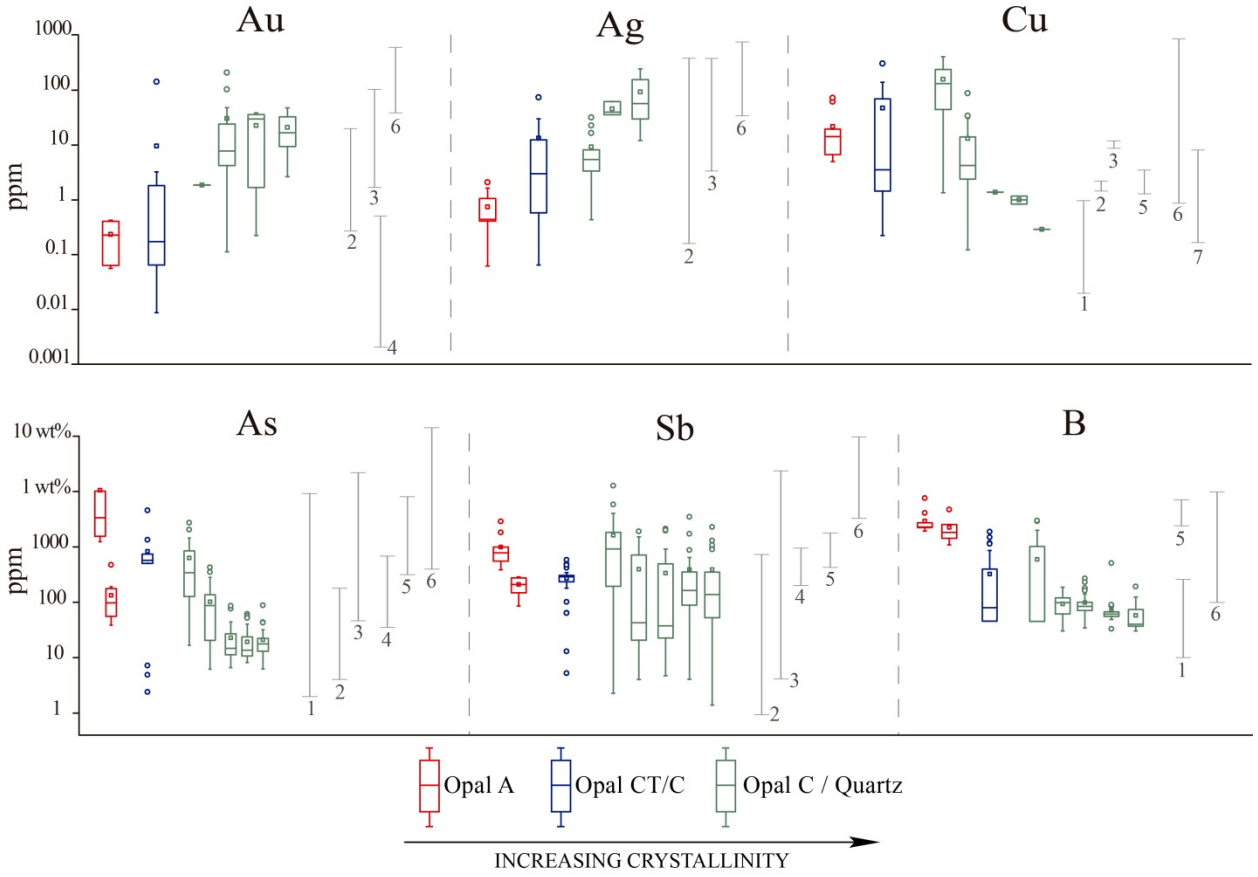

Figura 11. Box and whisker chart showing the concentration of metals (Au, Ag, Cu) and metalloids (As, Sb, B) in sinters from Puchuldiza measured by LA-ICP-MS and plotted against the degree of crystallinity of silica. Measured concentrations in opal A, -opal CT and opal C/quartz are shown in red, blue and green boxes, respectively. As a comparison, elemental concentrations in sinters reported in the literature are shown on the right-hand side (black lines, no corresponding crystallinity data available). References: (1): Steamboat Springs and Opal Mound, US (Lynne et al., 2007); (2): Deseado Massif, Argentina (Guido et al., 2002); (3):Champagne Pool, New Zealand (Jones et al., 2001), (4):Hoshino area, Japan (Belhadi et al., 2002); (5): El Tatio, Chile (Landrum et al., 2009); (6):Waiotapu, New Zealand (Pope et al., 2005); (7):Drummond Basin, Australia (Uysal et al., 2011).

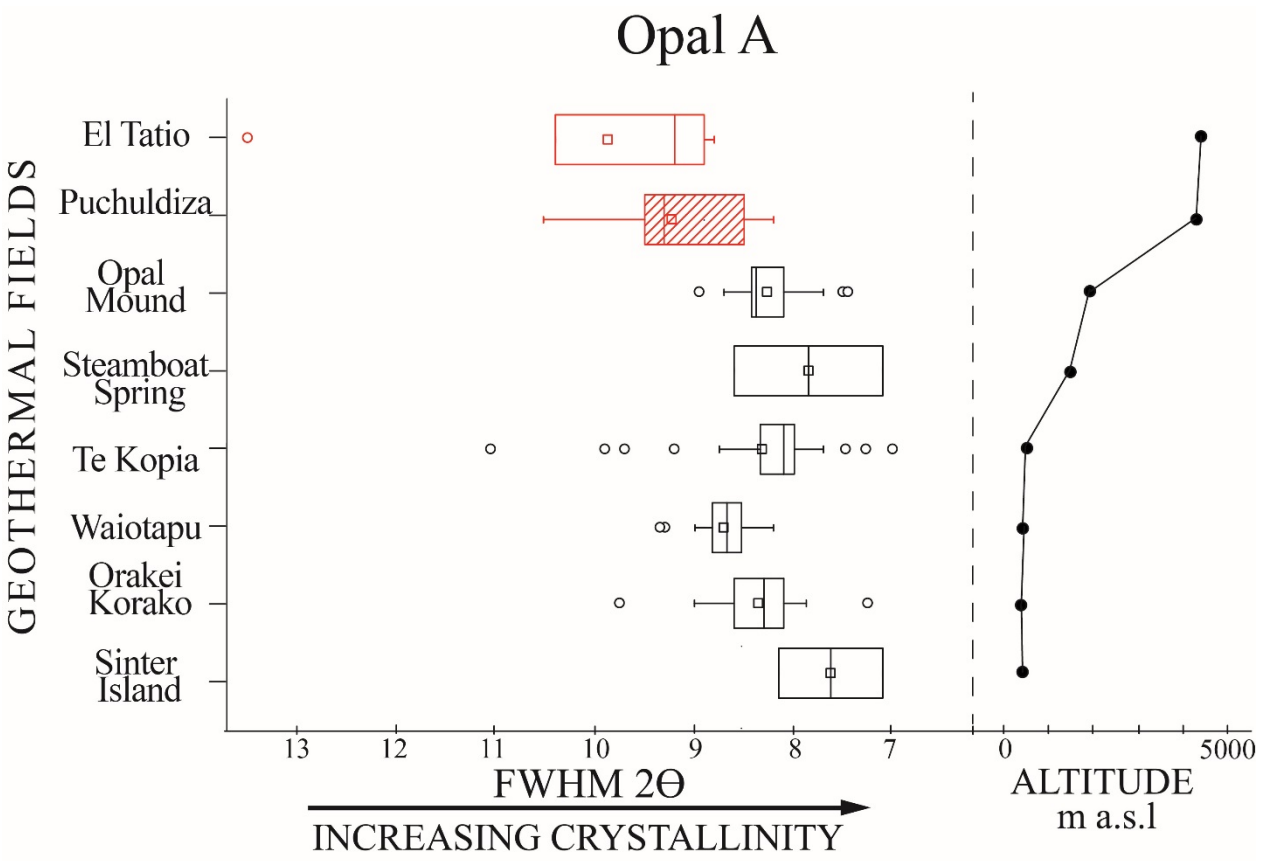

Figura 12. Box and whisker chart showing the Full Width Half Maximum (FWHM, or "degree of crystallinity") values measured on XRD traces of opal A. The data shown includes samples from Puchuldiza (this work) and from previously published studies, spanning a wide range of altitudes (m a.s.l.). The high FWHM is a key characteristic of sinter deposits from high-altitude setting (e.g., Chilean Altiplano). References: El Tatio, Chile (Nicolau et al., 2014), Opal Mound, US (Lynne et al., 2005), Steamboat Spring, USA (Lynne et al., 2007), Te Kopia (Lynne and Campbell, 2004; Rodgers et al., 2004), Waiotapu, New Zealand (Lynne and Campbell, 2004; Rodgers et al., 2004), Orakei Korako, New Zealand (Lynne and Campbell, 2004) and Sinter Island, New Zealand (Lynne et al., 2007).

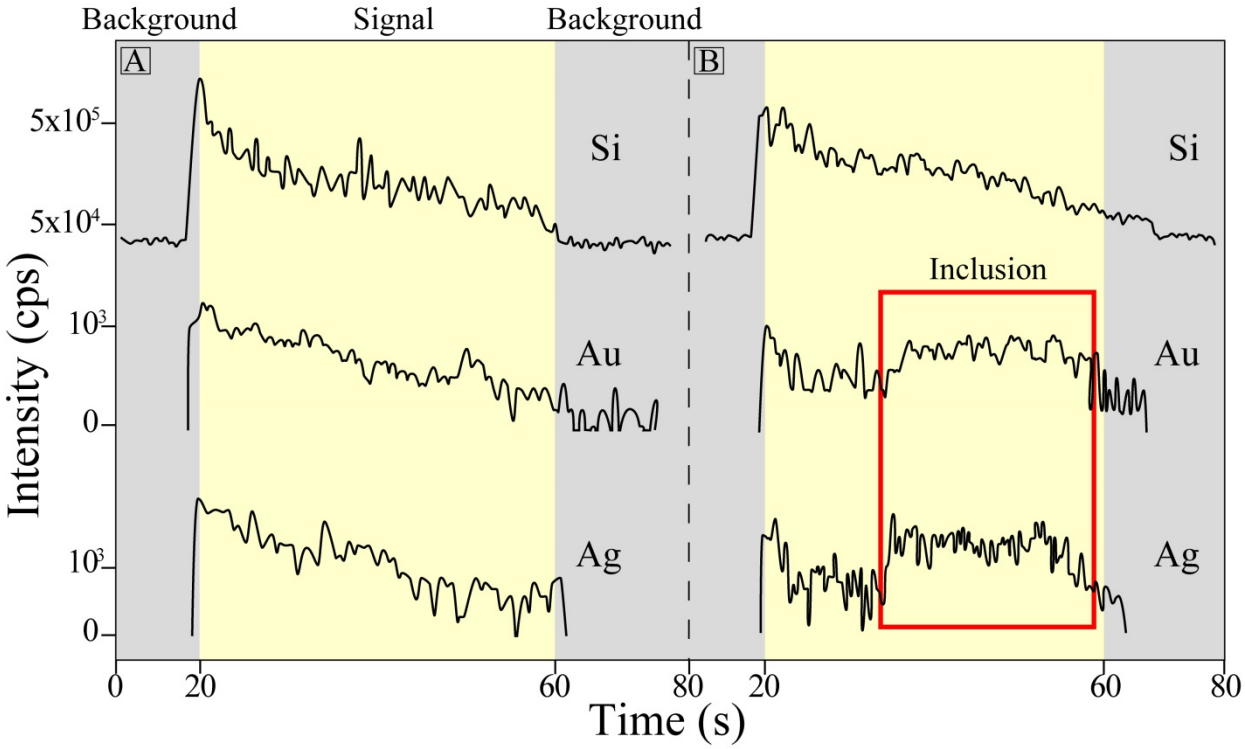

Figura 13. Representative time vs. intensity signals for Si, Au, and Ag obtained during LA-ICP-MS analyses in sample M2.6r. (A) Profile shows homogeneous distribution of Si, Au and Ag, (B) Ablation of Au and Ag-bearing inclusions hosted in the silica matrix show as spikes in the transient signal (red rectangle). Intensity is in counts per second (cps) and time in seconds (s).

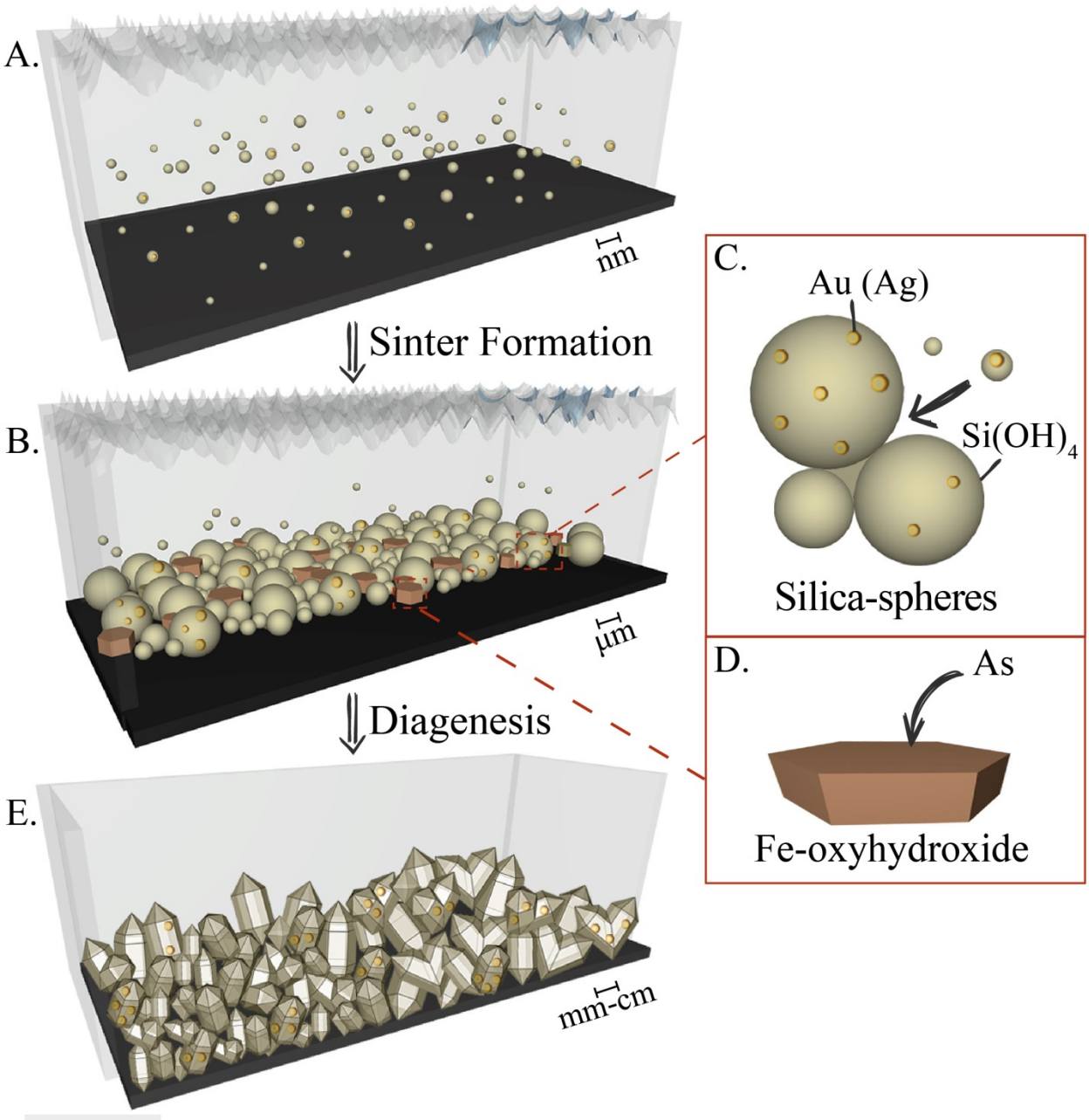

Figura 14. Conceptual model of metal incorporation into silica phases during sinter formation. (A): At the nano-scale, the initial stage of sinter formation starts with over saturation of geothermal water with respect to silica as they discharge and cool at the surface, resulting in silica precipitation; (B): Amorphous opal A nanospheres agglomerate and form micro-spheres. During this stage, gold and silver are incorporated into silica spheres either as cationic species and/or metal nanoparticles or colloids (C), while arsenic and boron are incorporated into accessory minerals Fe-oxyhydroxides (D, brown). (E) As diagenesis progress, metals are enriched while metalloids are depleted from the sinter as a result of structural changes underwent

by the silica host (i.e., maturation or increase in crystallinity), among other kinetically controlled processes.

3.8References

(JICA) J. I. C. A. (1979) *Geothermal Power Development Project in Puchuldiza Area.*,

Alsina M., Zanella L., Hoel C., Pizarro G. E., Gaillard J. F. and Pasten P. a. (2013) Arsenic speciation in sinter mineralization from a hydrothermal channel of El Tatio geothermal field, Chile. *J. Hydrol.* **518**, 434–446.

Amberg A. (2011) *NI 43-101 Technical Report, Puchuldiza Project, I Region Chile.*,

Aravena D., Muñoz M., Morata D., Lahsen A., Parada M. Á. and Dobson P. (2016) Geothermics Assessment of high enthalpy geothermal resources and promising areas of Chile. *Geothermics* **59**, 1–13.

Barnard A. and Guo H. (2012) *Nature's Nanostructures*., Pan Standford Pte. Ltd., Singapore.

Belhadi a., Nakanishi T., Watanabe K. and Izawa E. (2002) Gold mineralization and occurrence of sinter in the Hoshino area, Fukuoka prefecture, Japan. *Resour. Geol.* **52**, 371–380.

Bisone S., Chatain V., Blanc D., Gautier M., Bayard R., Sanchez F. and Gourdon R. (2016) Geochemical characterization and modeling of arsenic behavior in a highly contaminated mining soil. *Environ. Earth Sci.* **75**, 306.

Buffle J. and Leppard G. (1995) Characterization of aquatic colloids and macromolecules. 1. Structure and behavior of colloidal material. *Environ. Sci. Technol.* **29**, 2169–2175.

Cademartiri L., Bishop K. J. M., Snyder P. W. and Ozin G. a. (2012) Using shape for self-assembly. *Philos. Trans. R. Soc. A Math. Phys. Eng. Sci.* **370**, 2824–2847.

Cady S. L. and Farmer J. D. (1996) Fossilization Processes in Siliceous Thermal Springs: Trends in Preservation Along Thermal Gradients. In *CIBA Foundation Symposium, no. 202* (eds. G. . Bock and J. . Goode). Wiley, Chichester, U.K. pp. 150–173.

Campbell K. a., Lynne B. Y., Handley K. M., Jordan S., Farmer J. D., Guido D. M., Foucher F., Turner S. and Perry R. S. (2015) Tracing Biosignature Preservation of Geothermally Silicified Microbial Textures into the Geological Record. *Astrobiology* **15**, 858–882.

Campbell K., Buddle T. F. and Browne P. R. L. (2003) Late Pleistocene siliceous sinter associated with fluvial, lacustrine, volcaniclastic and landslide deposits at Tahunaatara,

Taupo Volcanic Zone, New Zealand. *Earth Environ. Sci. Trans. R. Soc. Edinburgh* **94**, 485–501.

Cassano D., Rota Martir D., Giovanni S., Vincenzo P. and Violani V. (2014) Solution phase n-doping of C60 and PCBM using tetrabutylammonium fluoride. *J. Mater. Chem.* **2**, 303.

Cortés J., Cascante M. and Zavala V. (2014) *Geología de las Áreas Isluga y Sierra de Huaillas, Región de Tarapacá. Servicio Nacional de Geología y Minería, Carta Geológica de Chile, Serie Geología Básica*.,

Dal Martello E. (2012) Impurity distribution and reduction behaviour of quartz in the production of high purity silicon. Norwegian University of Science and Technology.

Dal Martello E., Tranell G., Ostrovski O., Zhang G., Raaness O., Larsen R. B., Tang K. and Koshy P. (2012) Trace Elements in the Si Furnace-Part II: Analysis of Condensate in Carbothermal Reduction of Quartz. *Metall. Mater. Trans. B* **44**, 244–251.

Dal Martello E., Tranell G., Ostrovski O., Zhang G., Raaness O., Larsen R. B., Tang K. and Koshy P. (2013) Trace Elements in the Si Furnace-Part II: Analysis of Condensate in Carbothermal Reduction of Quartz. *Metall. Mater. Trans. B* **44**, 244–251. Available at: http://link.springer.com/10.1007/s11663-012-9720-9.

Deditius A. P., Reich M., Kesler S. E., Utsunomiya S., Chryssoulis S. L., Walshe J. and Ewing R. C. (2014) The coupled geochemistry of Au and As in pyrite from hydrothermal ore deposits. *Geochim. Cosmochim. Acta* **140**, 644–670.

Deditius A. P., Utsunomiya S., Renock D., Ewing R. C., Ramana C. V., Becker U. and Kesler S. E. (2008) A proposed new type of arsenian pyrite: composition, nanostructure and geological significance. *Geochim. Cosmochim. Acta* **72**, 2919–2933.

El-Ammouri E. (2000) Heavy Metals Removal from Effluents by Adsorption on Activated Silica Sols. McGill University, Montreal.

Ellis A. . and Mahon W. A. . (1977) Chemistry and Geothermal Systems. *Acad. Press*.

Fernandez-Turiel J. L., Garcia-Valles M., Gimeno-Torrente, D Saavedra-Alonso J. and Martinez-Manent S. (2005) The hot spring and geyser sinters of El Tatio, Northern Chile. *Sediment. Geol.* **180**, 125–147.

Ferullo R. M., Garda G. R., Belelli P. G., Branda M. M. and Castellani N. J. (2006) Deposition of small Cu, Ag and Au particles on reduced SiO2. *J. Mol. Struct. THEOCHEM* **769**, 217–223.

Fournier R. . and Rowe J. . (1966) Estimation of underground temperatures from the silica content ofwater from hot springs and steam wells. *Am. J. Sci.* **264**, 685–697.

Garcia-Valles M., Fernandez-Turiel J. L., Gimeno-Torrente D., Saavedra-Alonso J. and Martinez-Manent S. (2008) Mineralogical characterization of silica sinters from the El Tatio geothermal field, Chile. *Am. Mineral.* **93**, 1373–1383.

Gibson R. a., Sherry A., Kaur G., Pancost R. D. and Talbot H. M. (2014) Bacteriohopanepolyols preserved in silica sinters from Champagne Pool (New Zealand) indicate a declining temperature gradient over the lifetime of the vent. *Org. Geochem.* **69**, 61–69.

Giggenback W. . (1991) *Chemical techniques in geothermal exploration. Application of Geochemistry inGeothermal ReservoirDevelopment.*,

Giggenback W. . (1988) Geothermal solute equilibria. Derivation of Na–K–Mg–Ca geoindicators. *Geochim. Cosmochim. Acta*, 2749–2765.

Götze J., Plötze M., Graupner T., Hallbauer D. K. and Bray C. J. (2004) Trace element incorporation into quartz: A combined study by ICP-MS, electron spin resonance, cathodoluminescence, capillary ion analysis, and gas chromatography. *Geochim. Cosmochim. Acta* **68**, 3741–3759.

Guido D., de Barrio R. and Schalamuk I. (2002) La Marciana Jurassic sinter: implications for exploration for epithermal precious-metal deposits in Deseado Massif, southern Patagonia, Argentina. *Trans. Inst. Min. Metall. (Section B Appl. Earth Sci.* **111**, 106–113.

Guidry S. a. and Chafetz H. S. (2003) Anatomy of siliceous hot springs: Examples from Yellowstone National Park, Wyoming, USA. *Sediment. Geol.* **157**, 71–106.

Handley K. M., Campbell K. a, Mountain B. W. and Browne P. R. L. (2005) Abiotic-biotic controls on the origin and development of spicular sinter: in situ growth experiments, Champagne Pool, Waiotapu, New Zealand. *Geobiology* **3**, 93–114.

Hannington M., Haroardóttir V., Garbe-Shönberg D. and Brown K. L. (2016) Gold enrichment in active geothermal systems by accumulating colloidal suspensions. *Nat. Geosci.* **9**, 299–302.

Herdianita N. R., Browne P. R. L., Rodgers K. a. and Campbell K. a. (2000) Mineralogical and textural changes accompanying ageing of silica sinter. *Miner. Depos.* **35**, 48–62. Available at: http://link.springer.com/10.1007/s001260050005.

Herdianita N., Rodgers K. and Browne P. R. L. (2000) Routine instrumental procedures to characterise the mineralogy of modern and ancient silica sinters. *Geothermics* **29**, 65–81.

Hinman N. . and Walter M. . (2005) Textural preservation in siliceous hot spring deposits during early diagenesis: examples from Yellowstone National Park and Nevada, U.S.A. *J. Sediment. Res.* **75**, 200–215.

Hough R. M., Noble R. R. P. and Reich M. (2011) Natural gold nanoparticles. *Ore Geol. Rev.* **42**, 55–61.

Ichikuni M. (1970) Incorporation of Siliceous and Iron into Siliceous Sinters. *Chem. Geol.* **6**, 273–279.

Iler R. (1979) *The Chemistry of Silica: Solubility, Polymerization, Colloid and Surface Properties, and Biochemistry*.,

Jamtveit B. and Hammer Ø. (2012) Sculpting of Rocks by Reactive Fluids. *Geochemical Perspect.* **1**, 341–481.

JICA (1979) *Report on Geothermal Power Development Project in Puchuldiza Area. Phase I*.,

Johnson C., Wyall M., Li X., Ibrahim A., Schuster J., Southam G. and Magarvey N. (2013) Gold biomineralization by a metallophore from a gold-associated microbe. *Nat. Chem. Biol.* **9**, 241–243.

Jones B., Renaut R. W. and Rosen M. R. (2001) Biogenicity of gold- and silver-bearing siliceous sinters forming in hot (75°C) anaerobic spring-waters of Champagne Pool, Waiotapu, North Island, New Zealand. *J. Geol. Soc.* **158** , 895–911.

de Jonge L. W., Kjaergaard C. and Moldrup P. (2004) Colloids and colloid-facilitated transport of contaminants in soils. *Vadose Zo. J.* **3**, 321–325.

Kaasalainen H. and Stefánsson A. (2012) The chemistry of trace elements in surface geothermal waters and steam, Iceland. *Chem. Geol.* **330-331**, 60–85. Available at: http://linkinghub.elsevier.com/retrieve/pii/S0009254112003786 [Accessed November 25, 2014].

Kersting A., Efurd D., Finnegan D., Rokop D., Smith D. and Thompson J. (1999) Migration of plutonium in ground water at the Nevada Test Site. *Nature* **397**, 56–59.

Konhauser K. O. and Ferris F. G. (1996) Diversity of iron and silica precipitation by microbial mats in hydrothermal waters, Iceland: Implications for Precambrian iron formations. *Geology* **24**, 323–326.

Konhauser K. O., Jones B., Reysenbach A.-L. and Renaut R. W. (2003) Hot spring sinters: keys to understanding Earth's earliest life forms. *Can. J. Earth Sci.* **40**, 1713–1724.

Konhauser K. O., Phoenix V. R., Bottrell S. H., Adams D. G. and Head I. M. (2001) Microbial-silica interactions in Icelandic hot spring sinter: Possible analogues for some Precambrian siliceous stromatolites. *Sedimentology* **48**, 415–433.

Kretzschmar R. and Schafer T. (2005) Metal Retention and Transport on Colloidal Particles in

the Environment. *Elements* **1**, 205–210.

Lahsen A. (1978) *Evaluación de los resultados de la exploración del campo geotérmico de Puchuldiza, I región Tarapacá. CORFO - Comité para el Aprovechamiento de la Energía Geotérmica*.,

Lahsen A. (1970) *Informe preliminar sobrelageología de Puchuldiza. CORFO- Comité Geotérmico, Estudio para el Desarrollo Geotérmico en el norte de Chile.*,

Lahsen A., Sepúlveda F., Rojas J. and Palacios C. (2005) Present Status of Geothermal Exploration in Chile. In *World Geothermal Congress 2005* pp. 24–29.

Lalonde S., Konhauser K. O., Reysenback A. and Ferris F. (2005) The experimental silicification of Aquificales and their role in hot spring formation. *Geobiology* **72**, 1257–1268.

Landrum J. T., Bennett P. C., Engel a. S., Alsina M. a., Pastén P. a. and Milliken K. (2009) Partitioning geochemistry of arsenic and antimony, El Tatio Geyser Field, Chile. *Appl. Geochemistry* **24**, 664–676. Available at: http://linkinghub.elsevier.com/retrieve/pii/S0883292708004496 [Accessed December 11, 2014].

Lehmann G. and Bambauerp H. U. (1973) Quartz Crystals and Their Colors. *Angew. Chem. Internat. Ed.* **12**, 283–291.

Liu Y., Hu Z., Gao S., Günther D., Xu J., Gao C. and Chen H. (2008) In situ analysis of major and trace elements of anhydrous minerals by LA-ICP-MS without applying an internal standard. *Chem. Geol.* **257**, 34–43.

Lynne B. Y. (2012a) Life At High Altitude : a Comparative Study of High Versus Low Altitude Hot Spring Settings and Associated Sinter Textures From El Tatio , Chile and the Taupo Volcanic Zone , New Zealand . *Geotherm. Resour. Counc.* **36**, 1–7.

Lynne B. Y. (2012b) Mapping vent to distal-apron hot spring paleo-flow pathways using siliceous sinter architecture. *Geothermics* **43**, 3–24.

Lynne B. Y. and Campbell K. a (2004) Morphologic and Mineralogic Transitions From Opal-A to Opal-CT in Low-Temperature Siliceous Sinter Diagenesis, Taupo Volcanic Zone, New Zealand. *J. Sediment. Res.* **74**, 561–579.

Lynne B. Y., Campbell K. a., James B. J., Browne P. R. J. and Moore J. (2007) Tracking crystallinity in siliceous hot-spring deposits. *Am. J. Sci.* **307**, 612–641.

Lynne B. Y., Campbell K. a., Moore J. and Browne P. R. L. (2008) Origin and evolution of the Steamboat Springs siliceous sinter deposit, Nevada, U.S.A. *Sediment. Geol.* **210**, 111–131.

Lynne B. Y., Campbell K. a., Moore J. N. and Browne P. R. L. (2005) Diagenesis of 1900-year-old siliceous sinter (opal-A to quartz) at Opal Mound, Roosevelt Hot Springs, Utah, U.S.A. *Sediment. Geol.* **179**, 249–278. Available at: http://linkinghub.elsevier.com/retrieve/pii/S0037073805002162 [Accessed November 14, 2014].

Mahon W. and Cusicanqui H. (1980) Geochemistry of the Puchuldiza and Tuja hot springs, Chile. *New Zeal. J. Sci.* **23**, 149–159.

McKenzie E. J., Brown K. L., Cady S. L. and Campbell K. a. (2001) Trace metal chemistry and silicification of microorganisms in geothermal sinter, Taupo Volcanic Zone, New Zealand. *Geothermics* **30**, 483–502.

Mohammadnejad S., Provis J. L. and Deventer J. S. J. Van (2013) Reduction of gold (III) chloride to gold (0) on silica surfaces. *J. Colloid Interface Sci.* **389**, 252–259.

Montenegro C., Katja D., Lahsen A. and Parada M. (2008) Actualización de los antecedentes geoquímicos y geofísicos del campo geotérmico de Puchuldiza y su comparación con el área de exploración geotérmica de Guanacota, región de Tarapaca. Memoria de Título. Departamento de geología, Universidad de Chile. .

Nair S., Karimzadeh L. and Merkel B. J. (2014) Sorption of uranyl and arsenate on SiO2, Al2O3, TiO2 and FeOOH. *Environ. Earth Sci.* **72**, 3507–3512.

Nelson C. and Giles D. (1985) Hydrothermal Eruption Mechanisms and Hot Spring Gold Deposits. *Econ. Geol.* **80**, 1633–1639.

Nicolau C., Reich M. and Lynne B. (2014) Physico-chemical and environmental controls on siliceous sinter formation at the high-altitude El Tatio geothermal field, Chile. *J. Volcanol. Geotherm. Res.* **282**, 60–76.

Okamoto A., Saishu H., Hirano N. and Tsuchiya N. (2010) Mineralogical and textural variation of silica minerals in hydrothermal flow-through experiments: Implications for quartz vein formation. *Geochim. Cosmochim. Acta* **74**, 3692–3706.

Orange F., Lalonde S. V and Konhauser K. O. (2013) Experimental simulation of evaporation-driven silica sinter formation and microbial silicification in hot spring systems. *Astrobiology* **13**, 163–76.

Ortiz M., Achurra L., Cortés R., Fonseca A., Silva C. and Vivallos J. (2008) *Exploración Geológica para el fomento de la energía geotérmica*.,

Ortiz M., Achurra L., Cortés R., Fonseca A., Silva C. and Vivallos J. (2008) *Exploración*

Geológica para el fomento de la energía geotérmica. Estudio Geológico, Geofísico e Hidroquímico del Sector Puchuldiza Sur., Santiago, Chile.

Pancost R. D., Pressley S., Coleman J. M., Benning L. G. and Mountain B. W. (2005) Lipid biomolecules in silica sinters: indicators of microbial biodiversity. *Environ. Microbiol.* **7**, 66–77.

Parker R. J. and Nicholson K. (1990) Arsenic in geothermal sinters: determineation and implications for mineral exploration. *12th NZ Geotherm. Work.*, 35–39.

Phoenix V., Renaut R., Jones B. and Grant F. (2005) Bacterial S-layer preservation and rare arsenic – antimony – sulphide bioimmobilization in siliceous sediments from Champagne Pool hot spring , Waiotapu , New Zealand. *J. Geol. Soc. London* **162**, 323–331.

Pope J. and Brown K. L. (2014) Geochemistry of discharge at Waiotapu geothermal area, New Zealand – Trace elements and temporal changes. *Geothermics* **51**, 253–269. Available at: http://linkinghub.elsevier.com/retrieve/pii/S0375650514000078 [Accessed November 25, 2014].

Pope J. G., Brown K. L. and McConchie D. M. (2005) Gold concentrations in springs at Waiotapu, New Zealand: Implications for precious metal deposition in geothermal systems. *Econ. Geol.* **100**, 677–687.

Reich M., Kesler S. E., Utsunomiya S., Palenik C. S., Chryssoulis S. L. and Ewing R. C. (2005) Solubility of gold in arsenian pyrite. *Geochim. Cosmochim. Acta* **69**, 2781–2796.

Rimstidt J. . and Cole D. (1983) Geothermal mineralization I: The mechanism of formation of the Beowawe, Nevada, siliceous sinter deposit. *Am. J. Sci.* **283**, 861–875.

Rodgers K. a., Browne P. R. L., Buddle T. F., Cook K. L., Greatrex R. a., Hampton W. a., Herdianita N. R., Holland G. R., Lynne B. Y., Martin R., Newton Z., Pastars D., Sannazarro K. L. and Teece C. I. a. (2004) Silica phases in sinters and residues from geothermal fields of New Zealand. *Earth-Science Rev.* **66**, 1–61. Available at: http://linkinghub.elsevier.com/retrieve/pii/S0012825203001259 [Accessed January 1, 2015].

Rossman G. (1994) Colored Varieties of the Silica Minerals. In *Silica: Physical Behavior, Geochemistry and Materials Applications - Reviews in Mineralogy Volume 29* (eds. P. . Heaney, C. . Prewitt, and G. . Gibbs). Mineralogical Society of America. pp. 433–467.

Saishu H., Okamoto a. and Tsuchiya N. (2012) Mineralogical variation of silica induced by Al and Na in hydrothermal solutions. *Am. Mineral.* **97**, 2060–2063.

Saunders J. a. (1990) Colloidal transport of gold and silica in epithermal precious-metal systems:

evidence from the Sleeper deposit, Nevada. *Geology* **18**, 757–760.

Saunders J. a. (1994) Silica and gold textures in bonanza ores of the Sleeper deposit, Humboldt County, Nevada: evidence for colloids and implications for epithermal ore-forming processes. *Econ. Geol.* **89**, 628–638.

Shor A. M., Ivanova-Shor E. a., Laletina S. S., Nasluzov V. a. and Rösch N. (2010) Small silver clusters at paramagnetic defects of silica surfaces a density functional embedded-cluster study. *Surf. Sci.* **604**, 1705–1712.

Sillitoe R. H. (2015) Epithermal paleosurfaces. *Miner. Depos.* **50**, 767–793.

Smith B., Turner S. and Rodgers K. (2003) Opal-A and associated microbes from Wairakei, New Zealand: the first 300 days. *Mineral. Mag.*, 563–579.

Smith D. K. (1998) Nomenclature of the Silica Minerals and Bibliography. *Power Diffr.* **13**, 2–19.

Smith S. D. and Edwards M. (2005) The influence of silica and calcium on arsenate sorption to oxide surfaces. *J. Water Supply Res. Technol. - AQUA* **54**, 201–211.

Swedlund P. and Webster J. (1999) Adsorption and polymerisation of silicic acid on ferrihydrite, and its effect on arsenic adsorption. *Water Res* **33**, 3413–3422.

Tassi F., Aguilera F., Darrah T., Vaselli O., Capaccioni B., Poreda R. J. and Delgado Huertas a. (2010) Fluid geochemistry of hydrothermal systems in the Arica-Parinacota, Tarapacá and Antofagasta regions (northern Chile). *J. Volcanol. Geotherm. Res.* **192**, 1–15. Available at: http://linkinghub.elsevier.com/retrieve/pii/S0377027310000405 [Accessed November 26, 2014].

Tobler D. J. and Benning L. G. (2013) In situ and time resolved nucleation and growth of silica nanoparticles forming under simulated geothermal conditions. *Geochim. Cosmochim. Acta* **114**, 156–168. Available at: http://dx.doi.org/10.1016/j.gca.2013.03.045.

Tobler D. J., Shaw S. and Benning L. G. (2009) Quantification of initial steps of nucleation and growth of silica nanoparticles: An in-situ SAXS and DLS study. *Geochim. Cosmochim. Acta* **73**, 5377–5393. Available at: http://dx.doi.org/10.1016/j.gca.2009.06.002.

Tobler D. J., Stefánsson A. and Benning L. G. (2008) In-situ grown silica sinters in Icelandic geothermal areas. *Geobiology* **6**, 481–502.

Urzúa M. (1999) Geoquímica y productos de alteración en el area geotermal de Puchuldiza, región de Tarapacá, Chile. Memoria para optal el titulo de geólogo, U. de Chiel. .

Uysal I. T., Gasparon M., Bolhar R., Zhao J. X., Feng Y. X. and Jones G. (2011) Trace element

composition of near-surface silica deposits-A powerful tool for detecting hydrothermal mineral and energy resources. *Chem. Geol.* **280**, 154–169.

Veith G. M., Lupini A. R., Rashkeev S., Pennycook S. J., Mullins D. R., Schwartz V., Bridges C. a. and Dudney N. J. (2009) Thermal stability and catalytic activity of gold nanoparticles supported on silica. *J. Catal.* **262**, 92–101.

Wen Low X., Yuan C., Rhoades E., Zhang Q. and Archer L. a. (2006) Encapsulation and Ostwald ripening of Au and Au-Cl complex nanostructures in silica shells. *Adv. Funct. Mater.* **16**, 1679–1684.

Williams L. ., Parks G. . and Crerar D. . (1985) Silica diagenesis, I. Solubility controls. *J. Sedmentary Petrogr.* **89**, 8463–8484.

Yokoyama T., Taguchi S., Motomura Y., Watanabe K., Nakanishi T., Aramaki Y. and Izawa E. (2004) The effect of aluminum on the biodeposition of silica in hot spring water: Chemical state of aluminum in siliceous deposits collected along the hot spring water stream of Steep Cone hot spring in Yellowstone National Park, USA. *Chem. Geol.* **212**, 329–337.

De Yoreo J. J., Gilbert P. U. P. a., Sommerdijk N. a. J. M., Penn R. L., Whitelam S., Joester D., Zhang H., Rimer J. D., Navrotsky A., Banfield J. F., Wallace a. F., Michel F. M., Meldrum F. C., Colfen H. and Dove P. M. (2015) Crystallization by particle attachment in synthetic, biogenic, and geologic environments. *Science (80-.).* **349**, aaa6760.

Zeng L. (2004) Arsenic adsorption from aqueous solutions on an Fe (III)-Si binary oxide adsorbent. *Water Qual. Res. J. Canada* **39**, 267–275.

Zhou J. and Lau K. . (1998) Does a monsoon climate exist over South America? *J. Clim.*, 1020–1040.

CAPITULO 4

CONCLUSIONES

En esta investigación se estudiaron las características morfo-cristalográficas y geoquímicas de muestras de sínter del campo geotérmico de Puchuldiza en el Altiplano del norte de Chile. Las rocas, asociadas a paleo-sínter y sínter neo-formado, se caracterizaron por una secuencia diagenética completa para la sílice, con variaciones cristalográficas entre las fases amorfas de ópalo A, fases para-cristalinas de ópalo A/CT, ópalo CT-ópalo C y fases micro cristalinas de cuarzo. Además, se reportaron altas concentraciones de metales como Au, Ag y Cu, y metaloides como As, Sb y B.

Las fases silíceas presentaron una marcada correlación entre el enriquecimiento en metales preciosos (oro-plata) y el aumento en el grado de cristalinidad. Por el contrario, las fases amorfas exhibieron una mayor concentración en metaloides (arsénico-boro). Estas variaciones geoquímicas de las fases silíceas se relacionarían a las modificaciones estructurales y morfológicas producidas tanto en condiciones deposicionales y post-deposicionales de la sílice en los distintos estadíos de la transición diagenética.

Los metales preciosos pueden ser incorporados al sínter durante la formación de ópalo A o durante la diagénesis, al ser atraídos electrostáticamente a los defectos superficiales generados en la sílice producto de cambios físico-químicos durante las variaciones morfo-cristalográficas. Posteriormente, las partículas de oro y plata se aglomeran durante la diagénesis producto de la maduración de Ostwald, generando un mayor enriquecimiento en cristales de cuarzo.

El arsénico se encuentra enriquecido en las fases amorfas al estar relacionado principalmente con minerales accesorios que incluyen As en su estructura, como rejalgar, o bien con oxihidróxidos de hierro; los que adsorben arsénico en sus superficies. La presencia de diferentes minerales accesorios se asocia a variaciones en las condiciones de precipitación desde el fluido hidrotermal. La ausencia de morfologías relacionadas a otros minerales, sugiere que éstos son incorporados a la nanoescala o bien, son recubiertos por sílice.

El boro, al igual que el arsénico, se concentra principalmente en las fases amorfas, al incorporarse a la matriz silícea, pero es expulsado de la matriz durante el reordenamiento cristalográfico. Otros metales como antimonio y cobre no presentan patrones de enriquecimiento definidos y se asocian a una incorporación primaria durante la formación del sínter.

La fase amorfa de ópalo A en Puchuldiza, presenta altos valores de FWHM, al igual que en El Tatio (e.j., Nicolau et al., 2014). Esta característica es representativa de depósitos de sínter emplazados en una alta altitud topográfica como en el Altiplano, y respondería a la combinación de factores ambientales e hidroquímicos que influirían en los mecanismos de cristalización de la sílice.

BIBLIOGRAFÍA

Amberg A. (2011) *NI 43-101 Technical Report, Puchuldiza Project, I Region Chile.*,

Boudreau A. E. and Lynne B. Y. (2012) The growth of siliceous sinter deposits around high-temperature eruptive hot springs. *J. Volcanol. Geotherm. Res.* **247-248**, 1–8.

Cady S. L. and Farmer J. D. (1996) Fossilization Processes in Siliceous Thermal Springs: Trends in Preservation Along Thermal Gradients. In *CIBA Foundation Symposium, no. 202* (eds. G. . Bock and J. . Goode). Wiley, Chichester, U.K. pp. 150–173.

Campbell K. a., Lynne B. Y., Handley K. M., Jordan S., Farmer J. D., Guido D. M., Foucher F., Turner S. and Perry R. S. (2015) Tracing Biosignature Preservation of Geothermally Silicified Microbial Textures into the Geological Record. *Astrobiology* **15**, 858–882.

Cortés J., Cascante M. and Zavala V. (2014) *Geología de las Áreas Isluga y Sierra de Huaillas, Región de Tarapacá. Servicio Nacional de Geología y Minería, Carta Geológica de Chile, Serie Geología Básica*.,

Ellis A. . and Mahon W. A. . (1977) Chemistry and Geothermal Systems. *Acad. Press*.

Garcia-Valles M., Fernandez-Turiel J. L., Gimeno-Torrente D., Saavedra-Alonso J. and Martinez-Manent S. (2008) Mineralogical characterization of silica sinters from the El Tatio geothermal field, Chile. *Am. Mineral.* **93**, 1373–1383.

Geilert S., Vroon P. Z. and Bergen M. J. Van (2016) Effect of diagenetic phase transformation on the silicon isotope composition of opaline sinter deposits of Geysir , Iceland. *Chem. Geol.* **433**, 57–67.

Geilert S., Vroon P. Z., Keller N. S., Gudbrandsson S. and Stefa A. (2015) ScienceDirect Silicon isotope fractionation during silica precipitation from hot-spring waters : Evidence from the Geysir geothermal field , Iceland. *Geochim. Cosmochim. Acta* **164**, 403–427.

Giggenbach W. F. (1988) Geothermal solute equilibria. Derivation of Na-K-Mg-Ca geoindicators. *Geochim. Cosmochim. Acta* **52**, 2749–2765.

Giggenbach W.F. and Goguel R.L. (1989) *Collection and analysis of geothermal and volcanic water and gas discharges*. Report No. CD 2401. Department of Scientific and Industrial Research. Chemistry Division. Petone, New Zealand.

Giggenback W. . (1991) *Chemical techniques in geothermal exploration. Application of Geochemistry in Geothermal ReservoirDevelopment.*,

Guido D., de Barrio R. and Schalamuk I. (2002) La Marciana Jurassic sinter: implications for exploration for epithermal precious-metal deposits in Deseado Massif, southern Patagonia, Argentina. *Trans. Inst. Min. Metall. (Section B Appl. Earth Sci.* **111**, 106–113.

Guidry S. a. and Chafetz H. S. (2003) Anatomy of siliceous hot springs: Examples from Yellowstone National Park, Wyoming, USA. *Sediment. Geol.* **157**, 71–106.

Hamilton A., Campbell K., Rowland J. and Browne P. (2016) The Kohuamuri siliceous sinter as a vector for epithermal mineralisation, Coromandel Volcanic Zone , New Zealand. *Miner. Depos.*

Japan International Cooperation Agency (JICA), 1979. Geothermal power development project in Puchuldiza area. Unpubl. Report, 109 pp.

Herdianita N., Rodgers K. and Browne P. R. L. (2000) Routine instrumental procedures to characterise the mineralogy of modern and ancient silica sinters. *Geothermics* **29**, 65–81.

Ichikuni M. (1970) Incorporation of Siliceous and Iron into Siliceous Sinters. *Chem. Geol.* **6**, 273–279.

Johnson C., Wyall M., Li X., Ibrahim A., Schuster J., Southam G. and Magarvey N. (2013) Gold biomineralization by a metallophore from a gold-associated microbe. *Nat. Chem. Biol.* **9**, 241–243.

Konhauser K. O. and Ferris F. G. (1996) Diversity of iron and silica precipitation by microbial mats in hydrothermal waters, Iceland: Implications for Precambrian iron formations. *Geology* **24**, 323–326.

Lahsen A. (1978) *Evaluación de los resultados de la exploración del campo geotérmico de Puchuldiza, I región Tarapacá.* CORFO - Comité para el Aprovechamiento de la Energía Geotérmica.

Lahsen A., Alfredo. 1970. Informe preliminar sobre la geología de Puchuldiza. CORFO - Comité Geotérmico, Estudio para el Desarrollo Geotérmico en el Norte de Chile, 31 p., 2 planos, Santiago

Lahsen A., Sepúlveda F., Rojas J. and Palacios C. (2005) Present Status of Geothermal Exploration in Chile. In *World Geothermal Congress 2005* pp. 24–29.

Lynne B. Y., Campbell K. a., Moore J. N. and Browne P. R. L. (2005) Diagenesis of 1900-year-old siliceous sinter (opal-A to quartz) at Opal Mound, Roosevelt Hot Springs, Utah, U.S.A. *Sediment. Geol.* **179**, 249–278.

Lynne B. Y., Campbell K. a., James B. J., Browne P. R. J. and Moore J. (2007) Tracking crystallinity in siliceous hot-spring deposits. *Am. J. Sci.* **307**, 612–641.

Lynne B. Y., Campbell K. a., Moore J. and Browne P. R. L. (2008) Origin and evolution of the Steamboat Springs siliceous sinter deposit, Nevada, U.S.A. *Sediment. Geol.* **210**, 111–131.

Lynne B. Y. (2012a) Life At High Altitude : a Comparative Study of High Versus Low Altitude Hot Spring Settings and Associated Sinter Textures From El Tatio , Chile and the Taupo Volcanic Zone , New Zealand . *Geotherm. Resour. Counc.* **36**, 1–7.

Lynne B. Y. (2012b) Mapping vent to distal-apron hot spring paleo-flow pathways using siliceous sinter architecture. *Geothermics* **43**, 3–24.

Lynne B. Y. (2015) Impact of three common post-depositional environmental settings on siliceous sinter diagenesis: An eight year experiment. *J. Volcanol. Geotherm. Res.* **292**, 84.

Mahon W. and Cusicanqui H. (1980) Geochemistry of the Puchuldiza and Tuja hot springs, Chile. *New Zeal. J. Sci.* **23**, 149–159.

McKenzie E. J., Brown K. L., Cady S. L. and Campbell K. a. (2001) Trace metal chemistry and silicification of microorganisms in geothermal sinter, Taupo Volcanic Zone, New Zealand. *Geothermics* **30**, 483–502.

Montenegro C., Katja D., Lahsen A. and Parada M. (2008) Actualización de los antecedentes geoquímicos y geofísicos del campo geotérmico de Puchuldiza y su comparación con el área de exploración geotérmica de Guanacota, región de Tarapaca. Memoria de Título. Departamento de geología, Universidad de Chile. .

Nicolau C., Reich M. and Lynne B. (2014) Physico-chemical and environmental controls on siliceous sinter formation at the high-altitude El Tatio geothermal field, Chile. *J. Volcanol. Geotherm. Res.* **282**, 60–76.

Orange F., Lalonde S. V and Konhauser K. O. (2013) Experimental simulation of evaporation-driven silica sinter formation and microbial silicification in hot spring systems. *Astrobiology* **13**, 163–76.

Ortiz M., Achurra L., Cortés R., Fonseca A., Silva C. and Vivallos J. (2008) *Exploración Geológica para el fomento de la energía geotérmica. Estudio Geológico, Geofísico e Hidroquímico del Sector Puchuldiza Sur.*, Santiago, Chile.

Pancost R. D., Pressley S., Coleman J. M., Benning L. G. and Mountain B. W. (2005) Lipid biomolecules in silica sinters: indicators of microbial biodiversity. *Environ. Microbiol.* **7**, 66–77.

Parker R. J. and Nicholson K. (1990) Arsenic in geothermal sinters: determineation and implications for mineral exploration. *12th NZ Geotherm. Work.*, 35–39.

Phoenix V., Renaut R., Jones B. and Grant F. (2005) Bacterial S-layer preservation and rare arsenic – antimony – sulphide bioimmobilization in siliceous sediments from Champagne Pool hot spring , Waiotapu , New Zealand. *J. Geol. Soc. London* **162**, 323–331.

Pope J. and Brown K. L. (2014) Geochemistry of discharge at Waiotapu geothermal area, New Zealand – Trace elements and temporal changes. *Geothermics* **51**, 253–269.

Pope J. G., Brown K. L. and McConchie D. M. (2005) Gold concentrations in springs at Waiotapu, New Zealand: Implications for precious metal deposition in geothermal systems. *Econ. Geol.* **100**, 677–687.

Preston L. J., Benedix G. K., Genge M. J. and Sephton M. A. (2008) A multidisciplinary study of silica sinter deposits with applications to silica identification and detection of fossil life on Mars. *Icarus* **198**, 331–350.

Rodgers K. a., Browne P. R. L., Buddle T. F., Cook K. L., Greatrex R. a., Hampton W. a., Herdianita N. R., Holland G. R., Lynne B. Y., Martin R., Newton Z., Pastars D., Sannazarro K. L. and Teece C. I. a. (2004) Silica phases in sinters and residues from geothermal fields of New Zealand. *Earth-Science Rev.* **66**, 1–61.

Saunders J. a. (1994) Silica and gold textures in bonanza ores of the Sleeper deposit, Humboldt County, Nevada: evidence for colloids and implications for epithermal ore-forming processes. *Econ. Geol.* **89**, 628–638.

Sillitoe R. H. (2015) Epithermal paleosurfaces. *Miner. Depos.* **50**, 767–793.

Smith D. K. (1998) Nomenclature of the Silica Minerals and Bibliography. *Power Diffr.* **13**, 2–19.

Tassi F., Aguilera F., Darrah T., Vaselli O., Capaccioni B., Poreda R. J. and Delgado Huertas a. (2010) Fluid geochemistry of hydrothermal systems in the Arica-Parinacota, Tarapacá and Antofagasta regions (northern Chile). *J. Volcanol. Geotherm. Res.* **192**, 1–15.

Urzúa M. (1999) Geoquímica y productos de alteración en el area geotermal de Puchuldiza, región de Tarapacá, Chile. Memoria para optal el titulo de geólogo, U. de Chile.

Uysal I. T., Gasparon M., Bolhar R., Zhao J. X., Feng Y. X. and Jones G. (2011) Trace element composition of near-surface silica deposits-A powerful tool for detecting hydrothermal mineral and energy resources. *Chem. Geol.* **280**, 154–169.

Vaughan R. G., Hook S. J., Calvin W. M. and Taranik J. V (2005) Surface mineral mapping at Steamboat Springs , Nevada , USA , with multi-wavelength thermal infrared images. *Remote Sens. Environ.* **99**, 140–158.

Zhou J. and Lau K. . (1998) Does a monsoon climate exist over South America? *J. Clim.*, 1020–1040.

ANEXOS

Sitios de Muestreo

Definiciones morfológicas y de facies litológicas de sínter basadas en Guidry y Chafetz (2003) y definiciones texturales según Lynne et al. (2012).

Sitio	Descripción
1	Coordenada UTM 503043 / 7853763. Grupo de domos (*domal mounds*) activos e inactivos de 1.5 a 10 m de diámetro basal. La temperatura del agua es de 54.4ºC con pH 6.2. Algunos domos poseen canales de descarga ricos en materia orgánica que descargan por la pendiente (*apron slope*). En los bordes de los manantiales termales, se reconoce una amplia variedad de color asociada al sínter: blanco en la superficies y rojo, naranjo, amarillo y pardo en a la sub-superficie.
2	Coordenada UTM 503405 / 7853529. Manantial burbujeante de 50 cm de diámetro. La temperatura del agua es de 87.8ºC con pH 8.8. En la zona *splash*, el sínter exhibe colores blanco a pardo, con texturas espiculares (*spicular texture*) y columnares (*columnar texture*). En los bordes de la fuente se reconocen texturas *lily-pad* y *digitate*.
3	Coordenada UTM 503834 / 7853399. Domo (*domal mound*) de 1 m de diámetro con temperaturas de 78.7ºC y pH 7.5. Gran cantidad de materia orgánica en los canales de descarga en la *apron slope*. En los bordes de la fuente termal se reconoce textura oncoidal con colores que varían entre rosado, blanco, amarillo y rojo.
4	Coordenada UTM 504202 / 7853469. Manantial burbujeante de 3.5 m de diámetro con 75.4ºC y pH 7.8. Alrededor de la fuente se reconoce una zona con actividad hidrotermal intermitente, de color negro en la superficie y laminaciones rojas, blancas, pardas y grises en la sub-superficie. Las texturas predominantes son la textura geyserítica, *bulbous* y *columnar* con vegetación silicificada, los canales de descarga presentan texturas *digitate bulbous* y *dily-pad*.

5	Coordenada UTM 504301 / 7853087. Manantial burbujeante con 84°C y pH 8.2. El sínter asociado al manantial presenta diferentes coloraciones dependiendo el lugar de precipitación, entre verde a negro en el fondo de los canales de descarga; y negro, verde, rosado, naranjo y blanco en los bordes del manantial. En los bordes de la piscina se reconocen texturas columnar, *spicular*, *geyseritic* y *bulbous*; y en los canales de descarga textura *oncoidal* y *lily-pad* con gran actividad orgánica.
6	Coordenada UTM 504424 / 7853619. *Geyser* de 1.5x2.5 m de diámetro basal con una alta actividad eruptiva, con 82.3°C y pH 8. En la zona *splash* se reconoce textura geyserítica con colores blanco y grises, junto a variaciones de color en la *vent zone*, entre rosado, rojo y pardo.
7	Coordenada UTM 504454 / 7853715. *Geyser* de 2x2.5 m de diámetro basal, con 81.2°C y pH 8.3. La zona *splash* presenta texturas columnar, espicular y geyserítica, con colores blanco, gris y rojizo.
8	Coordenada UTM 504538 / 7853687. Paleo sínter en fuente termal inactiva de 1 m de diámetro. Se reconoce un paleo domo. Las muestras de sínter presentan laminaciones ondulantes menores a 0.5 cm de espesor, de colores blanco, gris, rosado y rojizo.
9	Coordenada UTM 504549 / 7853677. Paleo sínter en fuente termal inactive de 1.5 m de diámetro. Las muestras de sínter de las zonas proximales se caracterizaron por bandas menores a 0.5 cm de espesor de colores blanco, rosado, amarillo y rojizo.
10	Coordenada UTM 504564 / 7853670. *Geyser* artificial. La zona *splash* presenta variaciones de color entre pardo, rosado, naranjo y blanco, con texturas *digitate geyseritic*. Gran actividad orgánica en los canales de descarga.
11	Coordenada UTM 504496 / 7854185. Grupo de manantiales activos e inactivos, con 86°C y pH 8. Alrededor de las fuentes prevalece la textura geyserítica. En las fuentes activas se reconocieron laminaciones de texturas *spicular geyseritic* con coloraciones naranjas, rojizas, verdes y amarillas.

12	Coordenada UTM 504501 / 7854162. *Hot spring* de 2x2.5m, con 74.5°C y pH 8.2. Los márgenes de la fuente presentan texturas *palisade* de coloraciones blancas y grises.
13	Coordenada UTM 504447 / 7853491 (google earth). Depósito de paleo sínter con texturas *palisade*, *bubble mat*, *coniform, breccia* y *streamer*. Variaciones de color en laminaciones menores a 0.5 cm.

Resultados LA-ICP-MS

	^{7}Li	^{11}B	^{23}Na	^{24}Mg	^{27}Al	^{29}Si	^{39}K	^{44}Ca	^{48}Ti	^{54}Fe	^{55}Mn	^{63}Cu	^{75}As	^{107}Ag	^{121}Sb	^{197}Au
Error%	4.9 - 13.7	2.1 - 13.7	4.1 - 12.9	5.1 - 14.2	1 - 16.7	Reference	11.2 - 29.6	5.4 - 16.4	1.2 - 19	10.3 - 19	3.7 - 16.5	5.1 - 11.3	1.1 - 14.5	3.8 - 17.9	2 - 17.4	8 - 19.3
L.O.D	1.93	26.32	279	1.01	3.88		39.28	1240	2.13	280	2.17	1.11	9.86	0.26	0.9	0.07
M3.1	n.d	1403.98	3746.83	608.41	25.34	317002.59	586.40	12500.24	5.58	697.92	1849.65	n.d	34635.26	n.d	151.92	n.d
	n.d	1359.46	3526.08	615.76	1419.89	326384.24	585.62	13512.17	18.66	711.54	1421.89	n.d	943.82	n.d	114.73	n.d
	n.d	3645.13	3575.05	652.44	16.79	323238.16	859.55	14971.41	9.04	744.90	n.d	n.d	7694.44	n.d	65.59	n.d
	n.d	1806.81	4472.76	662.59	20.03	317582.89	849.97	13512.16	5.90	771.71	1857.21	n.d	1987.87	n.d	156.59	n.d
	17.16	1832.82	5126.41	457.76	209.82	298662.30	889.83	9806.71	4.19	548.29	2546.55	n.d	1097.66	n.d	184.49	n.d
	n.d	982.78	3972.19	601.57	63.58	279777.19	678.78	12328.89	4.27	699.72	3799.47	n.d	2272.42	n.d	196.17	n.d
	n.d	735.71	2931.63	750.65	173.15	273343.47	537.55	14227.84	3.65	793.23	3848.75	n.d	5703.33	n.d	184.52	n.d
	n.d	71.46	3642.38	1133.40	1343.11	267055.35	605.54	20874.80	5.29	1154.01	7773.48	n.d	11047.45	n.d	191.10	n.d
	n.d	144.94	2981.30	886.07	2954.87	282364.77	490.46	16575.05	6.27	897.53	6050.27	n.d	24292.79	n.d	615.40	n.d
	n.d	197.59	2845.22	761.59	309.61	282993.45	468.11	14150.95	3.85	780.53	5244.06	n.d	15162.78	n.d	276.25	n.d
	n.d	120.92	3281.81	973.72	14.84	279630.21	529.20	18064.94	3.32	964.57	6721.09	n.d	7920.43	n.d	163.27	n.d
	n.d	306.67	2945.02	699.74	19.93	285367.18	484.97	13596.42	3.33	726.08	4660.85	n.d	5535.55	n.d	176.70	n.d
	n.d	171.81	3393.16	933.86	16.46	275763.83	559.45	17342.03	3.34	930.25	6431.67	n.d	7938.50	n.d	208.17	n.d
	n.d	418.23	4826.53	765.34	30.34	275762.56	803.45	14818.36	3.86	842.85	5135.99	n.d	25327.32	n.d	441.05	n.d
	n.d	268.94	3446.88	742.44	38.32	279551.04	518.02	14265.56	3.29	749.22	5066.42	n.d	14055.60	n.d	199.29	n.d
	n.d	148.84	2656.52	728.70	20.48	273773.71	440.24	14066.58	4.68	717.98	5017.91	n.d	55047.56	n.d	559.34	n.d
	n.d	198.79	3014.49	766.51	18.42	275763.83	464.15	14836.69	3.49	734.61	5256.45	n.d	41468.45	n.d	426.62	n.d
	n.d	237.42	2810.02	742.09	14.32	275763.83	475.22	14308.72	2.75	709.77	5084.85	n.d	11987.08	n.d	264.36	n.d
	n.d	114.85	3614.80	920.72	14.49	275763.83	526.10	17720.74	3.89	886.46	6360.46	n.d	14888.10	n.d	196.12	n.d
	n.d	220.02	2652.52	667.41	15.44	275763.83	437.26	13141.25	2.57	641.23	4578.85	n.d	30960.14	n.d	367.83	n.d
M3.7	30.828	2325.02	2149.50	48.55	1260.21	439171.37	1324.51	10044.68	10.32	n.d	67.07	6.68	38.70	0.48	390.95	0.07
	44.048	2330.88	2013.80	69.56	1455.55	442822.95	1159.47	14255.51	5.59	618.77	94.08	6.88	63.80	0.41	491.32	n.d
	50.303	1974.01	2565.20	47.26	686.07	446553.66	2067.81	14647.05	3.70	1338.15	59.10	10.93	38.79	n.d	739.80	n.d
	134.937	2581.19	2493.51	47.72	539.60	450076.59	1988.84	6939.61	6.85	600.22	135.43	19.50	133.83	n.d	1006.17	n.d
	53.081	2266.16	972.84	35.66	691.82	450179.73	562.74	476.96	6.65	n.d	82.23	5.89	55.99	0.42	559.93	0.43
	59.275	2790.62	1400.81	78.53	305.36	449690.05	2211.84	1793.71	6.61	n.d	140.43	18.51	107.27	1.64	791.73	n.d
	62.230	2282.26	569.11	7.02	210.71	448482.81	232.95	n.d	67.33	n.d	n.d	16.95	90.92	0.44	798.45	0.38
	222.640	7771.00	2971.72	109.50	2025.90	450076.59	1481.46	715.26	42.07	894.24	150.91	61.48	191.13	n.d	1846.46	n.d
	86.007	2361.42	2706.92	99.71	2370.95	450076.59	1422.26	n.d	314.89	317.96	92.69	14.19	177.45	b.d.l.	918.76	0.07
	24.204	2299.84	1344.00	47.88	1199.49	450076.59	1039.45	294.24	85.41	b.d.l.	77.70	4.97	98.28	0.45	620.30	n.d
	150.423	4189.74	4019.50	390.38	13708.99	450076.59	9717.72	n.d	756.76	4847.05	449.41	71.95	472.49	2.10	2915.75	n.d
M3.6b	25.86	481.17	979.74	11.05	7.00	439858.75	675.07	n.d	n.d	n.d	28.43	n.d	28521.81	n.d	462.02	0.32
	32.14	728.95	1772.95	19.29	46.45	529659.84	935.08	n.d	b.d.l.	n.d	61.49	n.d	17461.79	n.d	228.25	n.d
	20.18	402.21	7743.95	9.42	677.34	485887.50	531.49	181.80	b.d.l.	n.d	27.89	36.70	35898.30	n.d	510.28	0.08
	1521.83	n.d	n.d	n.d	n.d	523952.52	5700.43	n.d	5827.62	n.d	n.d	219.91	7267.59	119.18	937.02	227.43
	2.03	n.d	n.d	n.d	284.87	484484.68	n.d	n.d	19.11	n.d	n.d	2.87	802.18	12.96	n.d	3.77
	n.d	275.11	n.d	n.d	n.d	488690.23	2975.94	78384.67	n.d	n.d	n.d	n.d	1076.70	n.d	403.84	n.d
	180.61	n.d	n.d	18.88	43.00	504845.81	1603.17	n.d	n.d	n.d	n.d	82.68	813.29	n.d	89.63	n.d
	275.99	2429.93	n.d	23.09	921.30	463307.54	8021.22	n.d	267.51	37066.73	315.06	154.32	n.d	15.85	130.58	0.15
	169.80	n.d	n.d	9.87	9.12	511227.16	1745.12	n.d	n.d	n.d	436.06	146.64	1633.07	n.d	78.89	n.d
	96.26	411.59	n.d	291.08	2129.03	421794.00	n.d	51408.10	400.07	20921.47	53.13	8.52	500.99	30.13	491.43	n.d
	23.53	101.46	1424.28	63.19	2276.34	450810.23	1163.28	8380.81	373.54	6233.22	68.24	n.d	n.d	n.d	423.78	0.94
	3.69	45.46	461.92	13.40	423.87	463221.03	283.28	n.d	97.63	b.d.l.	b.d.l.	1.88	n.d	b.d.l.	283.92	0.05
	b.d.l.	46.14	481.13	9.98	483.21	462691.01	166.68	2291.68	49.94	n.d	8.72	1.15	n.d	n.d	303.42	n.d
	2.81	80.96	611.65	12.74	389.12	463061.28	515.86	1348.82	68.30	n.d	10.89	1.14	b.d.l.	n.d	305.88	n.d
	4.00	63.85	633.71	15.10	511.70	463196.89	457.70	1714.97	60.41	n.d	3.32	1.51	b.d.l.	n.d	309.16	0.15
	2.49	70.79	595.48	15.58	675.45	461595.31	393.19	1184.88	54.67	b.d.l.	4.80	1.21	b.d.l.	n.d	278.96	0.09
	4.52	43.71	576.00	34.13	739.82	461447.60	455.75	1106.09	92.40	1035.71	n.d	3.90	n.d	n.d	292.85	0.07
	2.67	77.08	518.34	14.35	355.74	461589.68	441.75	258.66	53.55	1546.35	n.d	b.d.l.	n.d	n.d	279.69	b.d.l.
	n.d	126.08	97.06	14.59	1429.68	458691.21	115.33	n.d	142.54	2855.25	n.d	n.d	n.d	n.d	296.01	n.d
	b.d.l.	60.01	597.47	16.82	398.91	542355.66	407.87	2517.88	59.96	1208.82	4.62	n.d	n.d	0.74	375.69	0.29
	5.05	79.94	682.39	26.81	521.80	538659.19	458.40	1148.56	68.06	850.23	4.93	1.77	n.d	n.d	354.07	b.d.l.
	b.d.l.	94.92	1016.04	36.44	552.83	536879.39	468.41	5441.06	23.38	6162.80	n.d	4.06	n.d	n.d	395.71	1.20
	117.54	2163.77	n.d	n.d	18093.35	593725.70	3067.09	9576.16	166.53	n.d	53.74	429.73	1035.20	n.d	7.58	3.89
	4.42	144.53	727.89	13.64	4959.08	518899.86	456.46	5079.08	115.24	8839.01	n.d	n.d	n.d	0.94	403.08	0.07
	n.d	1378.59	5180.35	41.95	922.61	520321.10	843.10	25476.24	n.d	5712.30	100.51	38.84	n.d	n.d	553.14	n.d
	n.d	1487.17	n.d	n.d	n.d	536879.39	1364.30	n.d	85.91	13689.06	28.45	70.40	660.65	4.87	16.96	4.18
	46.48	n.d	n.d	n.d	666.72	536879.39	3086.00	5547.11	23.36	n.d	n.d	99.46	673.86	2.92	305.87	n.d
	n.d	104.08	623.25	13.84	324.86	536879.39	271.98	2759.55	3.93	5028.47	6.35	3.53	n.d	n.d	433.46	0.26
	n.d	1130.86	n.d	28.99	879.37	536879.39	n.d	n.d	282.02	38407.99	n.d	n.d	956.98	0.56	233.92	n.d

M2.2r	n.d	27.41	635.20	460.01	48.55	208046.04	1381.01	5608.48	b.d.l.	193763.14	n.d	n.d	b.d.l.	n.d	7.59	n.d
	n.d	30.83	652.78	474.99	128.24	206910.14	1398.52	5577.92	b.d.l.	188537.68	n.d	n.d	b.d.l.	n.d	4.78	n.d
	n.d	28.04	620.60	444.77	49.21	206168.71	1243.75	5312.48	b.d.l.	171200.17	n.d	n.d	b.d.l.	n.d	8.87	n.d
	n.d	b.d.l.	648.12	453.42	55.95	208523.41	1278.75	5367.05	b.d.l.	169377.78	n.d	n.d	b.d.l.	n.d	9.70	n.d
	n.d	27.97	721.87	518.30	67.79	205062.85	1412.12	5937.79	b.d.l.	191296.85	n.d	n.d	b.d.l.	n.d	4.26	n.d
	n.d	33.70	762.56	546.70	100.34	213638.14	1415.94	6379.42	b.d.l.	192662.60	n.d	n.d	b.d.l.	n.d	4.93	n.d
	n.d	34.03	716.49	478.92	593.92	220768.93	1303.00	5703.92	b.d.l.	161652.62	n.d	n.d	b.d.l.	n.d	21.20	n.d
	n.d	32.15	839.79	601.27	336.82	222814.14	1440.94	7040.47	b.d.l.	194806.29	n.d	n.d	b.d.l.	n.d	8.44	n.d
	n.d	31.48	715.45	458.16	185.03	224610.48	1241.52	5586.27	b.d.l.	149093.21	n.d	n.d	b.d.l.	n.d	15.87	n.d
	n.d	27.78	734.80	474.36	64.28	221562.57	1187.39	5723.60	b.d.l.	150711.99	n.d	n.d	b.d.l.	n.d	12.00	n.d
	n.d	33.31	774.03	481.72	106.05	224397.36	1321.49	6028.07	2.72	148455.85	n.d	n.d	b.d.l.	n.d	26.34	n.d
	n.d	32.79	856.62	606.04	46.92	226128.64	1400.55	7248.64	2.55	180280.49	n.d	n.d	b.d.l.	n.d	14.33	n.d
	n.d	30.71	853.92	568.65	47.18	230717.98	1308.09	6805.46	b.d.l.	162866.52	n.d	n.d	b.d.l.	n.d	13.88	n.d
	n.d	35.84	736.38	467.71	73.43	227229.98	1180.06	5856.33	4.86	135513.55	n.d	n.d	b.d.l.	n.d	26.48	n.d
	n.d	28.91	763.71	474.69	114.02	222136.72	1135.96	6012.68	b.d.l.	134321.63	n.d	n.d	b.d.l.	n.d	17.24	n.d
	n.d	29.43	804.32	521.59	45.52	216435.42	1284.80	6198.01	2.74	142669.94	n.d	n.d	b.d.l.	n.d	16.65	n.d
	n.d	31.92	882.69	602.99	63.81	207026.02	1287.26	7229.23	3.69	160227.50	n.d	n.d	b.d.l.	n.d	11.43	n.d
	n.d	27.23	838.84	543.02	52.55	207654.57	1211.45	6625.80	2.69	142080.24	n.d	n.d	b.d.l.	n.d	16.00	n.d
	n.d	29.14	879.45	575.20	73.67	210080.87	1257.87	6897.73	b.d.l.	150035.56	n.d	n.d	b.d.l.	n.d	13.52	n.d
	n.d	29.16	969.04	671.43	18.88	207651.85	1338.40	7703.78	b.d.l.	194577.45	n.d	n.d	b.d.l.	n.d	13.81	n.d
	n.d	28.13	860.71	577.04	70.50	210601.45	1171.88	6838.37	b.d.l.	163538.18	n.d	n.d	b.d.l.	n.d	17.92	n.d
	n.d	30.20	825.16	513.22	65.81	216605.16	1077.86	6293.32	b.d.l.	137647.80	n.d	n.d	b.d.l.	n.d	29.12	n.d
	n.d	28.23	950.52	620.86	44.62	211478.30	1271.62	7563.45	4.23	165914.95	n.d	n.d	b.d.l.	n.d	10.15	n.d
	n.d	27.20	978.73	654.26	104.92	209260.41	1273.25	7842.67	b.d.l.	168734.31	n.d	n.d	b.d.l.	n.d	8.77	n.d
	n.d	b.d.l.	799.25	501.98	1341.70	208704.67	1006.39	6121.79	b.d.l.	124112.02	n.d	n.d	b.d.l.	n.d	12.76	n.d
	n.d	252.23	1347.57	659.28	17.05	201101.69	1333.95	8546.68	71.87	135468.07	n.d	n.d	b.d.l.	n.d	123.52	n.d
	n.d	32.67	1131.33	732.92	7.80	198811.65	1297.96	9120.69	b.d.l.	151401.61	n.d	n.d	b.d.l.	n.d	2.29	n.d
	n.d	195.10	1285.97	749.80	10.74	208008.34	1475.67	9365.19	b.d.l.	155552.50	n.d	n.d	11.81	n.d	60.17	n.d
	n.d	33.21	1164.55	759.39	11.62	214022.74	1286.59	9470.22	41.53	151669.68	n.d	n.d	b.d.l.	n.d	56.25	n.d
	n.d	70.18	1216.73	773.01	11.84	212967.56	1367.90	9643.63	22.76	154464.52	n.d	n.d	b.d.l.	n.d	49.90	n.d
	n.d	29.11	872.81	520.67	101.53	212017.56	966.38	6728.63	3410.10	107469.99	n.d	n.d	51.62	n.d	982.67	3.62
	n.d	38.43	974.98	602.80	55.19	203352.33	1095.40	7688.39	746.06	118440.94	n.d	n.d	13.50	n.d	311.18	n.d
	n.d	36.39	1182.75	769.55	8.58	203042.87	1299.26	9758.91	3.05	145704.02	n.d	n.d	9.48	n.d	16.11	n.d
	n.d	b.d.l.	1231.17	822.97	9.28	210128.63	1330.07	10078.30	b.d.l.	152410.32	n.d	n.d	b.d.l.	n.d	8.45	n.d
	n.d	28.02	1272.16	815.29	13.27	211071.06	1334.31	10177.66	b.d.l.	149107.86	n.d	n.d	9.01	n.d	6.69	n.d
	n.d	45.81	1141.45	694.53	166.39	220784.27	1319.25	8927.86	11.06	128339.86	n.d	n.d	b.d.l.	n.d	121.44	n.d
	n.d	32.23	1021.44	647.58	62.50	216133.05	1072.96	8245.13	304.84	118330.00	n.d	n.d	10.14	n.d	232.51	n.d
	n.d	35.42	1249.51	809.59	21.68	211724.90	1331.43	10336.79	4.18	146742.14	n.d	n.d	b.d.l.	n.d	14.81	n.d
	n.d	44.90	954.79	587.45	90.75	211288.01	1064.71	7671.56	67.80	104731.65	n.d	n.d	15.09	n.d	416.12	n.d
	n.d	41.45	1250.72	792.48	70.35	210827.03	1333.38	10180.85	35.84	141711.63	n.d	n.d	b.d.l.	n.d	49.81	n.d
	n.d	49.49	1305.33	803.38	36.12	226833.71	1381.38	10526.15	188.65	143213.05	n.d	n.d	14.00	n.d	241.63	n.d
	n.d	33.62	1435.25	918.29	9.88	232950.22	1446.92	11841.11	6.21	161495.31	n.d	n.d	b.d.l.	n.d	23.08	n.d
	n.d	39.28	1123.06	680.25	247.20	247101.29	1242.66	9196.68	534.26	123395.66	n.d	n.d	35.70	n.d	1245.03	n.d
	n.d	39.64	896.38	513.82	353.12	244113.86	1015.96	7063.09	701.35	91469.39	n.d	n.d	22.01	n.d	1135.35	n.d
	n.d	33.71	1118.36	686.33	95.74	235854.68	1177.51	9147.38	92.50	118927.33	n.d	n.d	10.73	n.d	297.48	n.d
	n.d	39.14	986.94	573.38	113.92	239227.42	1110.38	7586.53	266.91	100218.78	n.d	n.d	30.17	22.52	518.76	21.80
	n.d	34.15	1211.11	729.16	132.71	226305.58	1175.56	9456.49	240.08	122316.91	n.d	n.d	17.35	n.d	297.77	16.46
	n.d	28.40	1125.20	685.93	51.45	230922.65	1129.90	8996.24	237.85	113774.78	n.d	n.d	21.97	19.68	286.28	15.92
	n.d	35.04	1020.86	613.13	115.89	231773.51	1070.78	8216.40	132.68	101561.19	n.d	n.d	14.44	n.d	427.72	0.92
	n.d	34.95	1440.59	901.71	26.53	230436.09	1408.29	11858.58	48.58	147251.58	n.d	n.d	12.54	n.d	36.91	n.d
	n.d	39.49	1109.77	666.48	83.94	240777.28	1165.37	9161.32	41.16	110590.13	n.d	n.d	13.97	n.d	271.66	n.d
	n.d	42.10	1183.59	717.03	100.75	246697.70	1194.55	9643.91	513.92	115671.02	n.d	n.d	11.75	n.d	440.71	n.d
	n.d	33.02	1076.80	657.71	57.81	231773.51	1072.60	8864.55	86.37	104164.91	n.d	n.d	9.74	n.d	238.63	n.d
	n.d	36.13	1019.44	602.37	150.41	231773.51	1058.17	8330.18	1118.65	101566.02	n.d	n.d	31.09	n.d	1173.61	n.d
	n.d	36.92	980.48	515.74	133.68	231773.51	968.48	8127.45	627.31	82473.91	n.d	b.d.l.	28.41	34.41	1111.73	19.66
	n.d	b.d.l.	730.22	371.27	104.76	231773.51	767.44	6616.87	712.85	54534.49	n.d	n.d	14.01	n.d	293.58	0.12

M2.5	n.d	1305.94	n.d	n.d	n.d	365554.10	7112.94	n.d	n.d	76932.05	n.d	283.42	83.64	n.d	336.76	n.d
	59.16	n.d	1649.95	5.51	557.14	379480.25	2155.32	37888.10	n.d	15619.73	n.d	1.31	353.78	n.d	4.60	n.d
	116.37	1984.35	n.d	432.54	n.d	382984.10	n.d	158900.98	412.06	n.d	189.55	154.75	1205.80	n.d	143.66	5.958
	n.d	356.13	n.d	13.37	1259.36	355048.81	3023.23	44978.93	n.d	53319.34	n.d	n.d	133.05	n.d	17.50	4.078
	n.d	n.d	n.d	22.89	858.32	357566.51	n.d	n.d	n.d	27850.50	127.90	30.84	54.22	5.32	n.d	0.109
	47.22	n.d	3614.23	16.27	n.d	348072.50	n.d	n.d	33.72	7477.49	113.87	n.d	171.32	n.d	109.88	n.d
	311.49	n.d	n.d	n.d	1242.57	358118.15	n.d	n.d	n.d	n.d	n.d	237.54	115.14	n.d	260.13	n.d
	188.10	n.d	8311.95	60.34	5981.55	401269.78	3092.80	53575.42	n.d	29549.78	186.84	n.d	n.d	n.d	81.67	n.d
	210.92	711.66	3192.00	14.95	6971.03	409645.13	1088.73	n.d	n.d	n.d	100.46	n.d	325.10	n.d	n.d	n.d
	640.39	411.37	n.d	20.95	n.d	400733.59	n.d	n.d	75.46	n.d	n.d	199.32	n.d	n.d	n.d	n.d
	19.60	n.d	2618.37	30.97	3165.37	337409.41	344.83	6102.42	n.d	2277.33	n.d	20.19	n.d	3.29	61.41	7.043
	77.50	392.18	12363.96	404.64	5792.22	322092.08	6429.27	n.d	189.30	14455.95	291.72	390.12	743.03	7.50	917.87	12.827
	b.d.l.	n.d	5255.52	39.93	n.d	330570.91	3265.72	n.d	368.35	3458.73	57.40	n.d	69.50	n.d	1.37	1.036
	518.69	2895.22	n.d	257.45	57725.63	354221.20	n.d	244401.83	n.d	136302.69	n.d	229.72	1985.92	31.29	9.19	100.384
	n.d	90.56	302.44	b.d.l.	3182.85	382025.85	1700.27	39705.25	64.15	35938.33	121.37	n.d	n.d	0.43	52.94	n.d
	102.57	n.d	796.16	3.71	655.76	409275.52	1588.65	n.d	n.d	10111.36	1.24	17.78	358.20	n.d	7.39	n.d
	n.d	n.d	n.d	n.d	2533.38	375898.12	93.18	n.d	514.77	n.d	38.41	n.d	629.29	n.d	1033.95	12.291
	n.d	1451.17	3500.85	2.46	n.d	328999.80	3080.67	45912.62	n.d	n.d	94.74	n.d	840.07	7.50	2094.70	n.d
	n.d	2773.65	5905.26	n.d	n.d	327533.51	n.d	n.d	121.47	n.d	n.d	214.74	n.d	n.d	828.98	43.739
	n.d	n.d	n.d	123.79	968.91	320129.65	3046.18	n.d	99.95	161521.38	291.61	89.68	n.d	2.71	126.01	9.485
	404.53	n.d	2028.97	n.d	n.d	332108.98	n.d	44075.15	212.76	197503.93	n.d	51.58	n.d	20.76	n.d	7.078
	n.d	n.d	504.29	n.d	n.d	358297.29	5026.29	172803.01	n.d	n.d	516.03	n.d	267.84	n.d	131.77	n.d
	20.23	n.d	n.d	n.d	n.d	346188.58	n.d	24944.15	n.d	27609.25	n.d	n.d	15.24	n.d	n.d	191.150
	n.d	151.30	n.d	n.d	n.d	289439.81	2331.50	n.d	n.d	90405.18	24.44	n.d	219.94	4.88	n.d	n.d
	n.d	1608.18	n.d	n.d	n.d	332108.98	n.d	n.d	83.04	62591.49	27.77	92.44	557.83	4.70	88.61	n.d
	106.48	1256.00	n.d	20.10	n.d	332108.98	12690.88	142238.62	72.99	100403.49	342.16	77.71	1315.83	15.11	205.51	3.163
	12.51	n.d	669.04	49.38	995.72	332108.98	n.d	105046.47	256.76	203225.45	358.99	296.69	2482.42	2.65	n.d	6.143
	192.13	567.56	n.d	16.26	6.92	332108.98	n.d	n.d	108.73	n.d	n.d	n.d	n.d	6.72	1190.31	22.061
M2.5b	n.d	b.d.l.	1702.80	963.73	145.52	201159.79	1368.68	16684.75	b.d.l.	109166.05	n.d	n.d	b.d.l.	n.d	1.24	n.d
	n.d	49.12	1545.08	826.46	45.73	201166.40	1269.73	14267.67	23.24	95176.30	n.d	b.d.l.	10.12	n.d	138.89	n.d
	n.d	b.d.l.	1626.50	917.86	22.24	196883.86	1352.29	16189.11	7.78	105100.49	n.d	n.d	10.83	n.d	32.38	n.d
	n.d	b.d.l.	1678.69	952.40	11.11	198760.30	1381.44	16383.08	b.d.l.	109487.00	n.d	n.d	b.d.l.	n.d	1.14	n.d
	n.d	b.d.l.	1650.31	963.98	33.39	200084.26	1365.22	16545.49	b.d.l.	107867.40	n.d	n.d	b.d.l.	n.d	1.26	n.d
	n.d	b.d.l.	1696.18	977.98	1263.77	202044.53	1365.58	16525.28	2.64	108378.91	n.d	n.d	b.d.l.	n.d	6.19	n.d
	n.d	35.44	1578.33	888.75	128.15	202473.56	1295.97	15068.32	27.14	99738.75	n.d	10.37	10.30	n.d	55.79	n.d
	n.d	33.16	1646.49	920.06	35.30	199548.72	1354.28	15667.47	43.50	103209.11	n.d	n.d	9.17	n.d	79.87	n.d
	n.d	49.51	1603.20	869.79	616.18	197410.94	1349.48	15762.90	417.16	97754.20	n.d	1.88	36.62	n.d	490.24	n.d
	n.d	81.32	1576.13	772.39	1610.88	198819.33	1330.87	13808.31	4991.55	102677.01	n.d	66.18	315.63	n.d	3819.43	n.d
	n.d	62.34	1637.69	867.84	731.43	200712.29	1345.26	15786.36	3536.56	107570.80	n.d	36.80	179.60	n.d	2452.44	n.d
	n.d	75.33	1663.32	833.46	503.93	201930.38	1446.19	14710.33	6239.44	109778.95	n.d	58.38	284.78	n.d	3943.67	1.25
	n.d	44.14	1606.53	881.27	301.57	208914.85	1346.06	15501.16	373.29	99093.72	n.d	2.64	45.52	n.d	457.13	n.d
	n.d	38.42	1766.02	978.95	1654.41	224103.20	1462.09	17161.09	3.09	110828.64	n.d	1.52	b.d.l.	n.d	78.71	n.d
	n.d	65.79	1927.90	1025.09	4928.10	236384.38	1644.53	18706.39	930.83	121048.36	n.d	19.81	80.43	n.d	1986.21	n.d
	n.d	b.d.l.	2073.24	946.64	339.22	245089.48	1804.47	26465.91	b.d.l.	98206.88	n.d	n.d	b.d.l.	n.d	1.86	n.d
	n.d	37.64	1419.39	602.00	124.84	248932.03	1322.85	17322.76	707.28	63755.21	n.d	n.d	55.73	n.d	562.30	n.d
	n.d	95.53	1511.25	641.86	180.27	233598.93	1333.45	16670.90	804.05	71750.40	n.d	n.d	41.02	n.d	430.06	n.d
	n.d	106.86	1955.06	744.01	378.75	229097.39	1493.37	16229.48	630.34	87354.11	n.d	17.24	82.28	n.d	807.04	n.d
	n.d	61.83	2063.37	739.83	211.67	224822.78	1225.91	14201.37	954.74	82916.63	n.d	b.d.l.	85.49	n.d	913.41	n.d
	n.d	67.14	1651.77	847.35	534.41	219947.65	1502.65	15610.24	1966.03	105503.99	n.d	2.33	113.06	n.d	1748.40	n.d
	n.d	84.18	1447.14	732.16	2117.04	223998.58	1261.07	13789.40	513.78	83497.11	n.d	b.d.l.	51.67	n.d	539.74	n.d
	n.d	77.81	1596.90	813.41	193.50	218696.26	1356.73	14894.93	1928.39	96240.77	n.d	1.77	102.02	n.d	1289.83	n.d
	n.d	76.06	1484.17	781.45	299.45	214569.83	1318.88	13911.01	1991.76	99443.01	n.d	1.67	87.98	n.d	1000.17	n.d
	n.d	71.82	1441.39	779.13	138.91	211614.98	1191.55	13877.01	326.65	88115.51	n.d	n.d	32.91	n.d	328.73	n.d
	n.d	b.d.l.	1555.14	860.66	256.39	211409.39	1261.08	15380.38	221.21	95420.22	n.d	n.d	13.67	n.d	136.55	n.d
	n.d	91.92	1504.67	771.46	2067.30	208894.84	1370.57	14561.64	7573.45	100183.45	n.d	4.99	246.73	n.d	2856.47	n.d
	n.d	86.12	1390.53	737.25	379.74	208643.92	1256.25	12830.77	505.34	125892.57	n.d	n.d	80.40	n.d	6712.49	n.d
	n.d	76.85	1432.81	750.29	612.19	209901.00	1230.09	13526.70	366.87	89490.11	n.d	n.d	39.05	n.d	1064.41	n.d
	n.d	50.21	1579.41	829.16	14732.43	203733.81	1342.16	14606.95	249.61	97195.83	n.d	7.26	35.59	n.d	621.31	n.d
	n.d	33.40	1664.02	945.67	1351.29	204894.73	1360.30	16218.71	351.74	105482.20	n.d	n.d	46.15	n.d	386.38	n.d
	n.d	49.04	1541.90	790.04	5688.12	209049.49	1336.48	14034.75	2754.21	96662.72	n.d	6.53	149.33	n.d	1862.25	n.d
	n.d	36.66	1807.48	972.99	4002.45	212670.08	1422.75	17802.14	505.68	106972.79	n.d	n.d	23.41	n.d	285.07	n.d
	n.d	42.64	1493.35	828.45	1198.68	203733.81	1329.78	14625.81	924.84	95340.95	n.d	n.d	68.64	n.d	965.84	n.d
	n.d	51.96	1462.90	782.21	5215.23	203733.81	1232.26	14440.65	600.38	88875.98	n.d	1.59	62.31	n.d	667.42	n.d
	n.d	73.15	1454.35	765.56	1189.17	203733.81	1181.69	13406.14	298.94	83620.97	n.d	n.d	53.73	n.d	591.59	n.d
	n.d	55.26	1442.04	790.53	2710.25	203733.81	1283.74	14096.75	370.90	86761.86	n.d	b.d.l.	23.88	n.d	274.88	n.d

M2.6b	n.d	37.88	1348.55	796.70	131.52	208393.58	1196.17	11811.97	2.17	110189.75	n.d	n.d	11.30	n.d	87.02	n.d
	n.d	45.91	1122.10	629.16	367.55	201226.40	1042.39	9381.43	30.16	86772.14	n.d	n.d	10.60	n.d	63.82	n.d
	n.d	43.42	1428.06	813.89	3140.91	193594.49	1354.90	12146.48	50.73	146391.33	n.d	n.d	11.19	n.d	17.84	n.d
	n.d	b.d.l.	1528.93	930.24	7.61	205411.70	1351.86	13372.39	b.d.l.	125730.86	n.d	n.d	9.91	n.d	2.06	n.d
	n.d	22.51	1511.60	932.15	9.43	205594.94	1359.25	13687.84	b.d.l.	153775.31	n.d	n.d	b.d.l.	n.d	7.78	n.d
	n.d	43.04	1408.18	813.08	144.82	211842.66	1314.00	11888.07	9.54	127948.59	n.d	n.d	b.d.l.	n.d	81.16	n.d
	n.d	138.78	1232.56	651.77	359.48	211661.78	1156.12	9653.16	2.58	97322.62	n.d	b.d.l.	b.d.l.	n.d	140.60	n.d
	n.d	35.69	1505.71	886.57	76.61	205364.76	1344.04	13281.71	b.d.l.	130435.49	n.d	n.d	b.d.l.	n.d	14.60	n.d
	n.d	b.d.l.	1411.11	834.06	15.51	215244.16	1247.22	12303.26	12.88	120168.36	n.d	n.d	9.71	n.d	317.80	n.d
	n.d	29.96	1525.00	904.80	21.63	221993.84	1318.07	13379.48	33.66	126923.72	n.d	n.d	b.d.l.	n.d	101.94	n.d
	n.d	19.24	1555.20	922.06	36.72	232408.46	1344.34	13490.54	24.58	128441.55	n.d	n.d	b.d.l.	n.d	106.18	n.d
	n.d	83.05	1327.50	703.40	301.47	245656.16	1314.42	10647.49	1343.69	108659.01	n.d	b.d.l.	51.09	n.d	2031.43	n.d
	n.d	131.91	1341.99	739.11	43.64	239166.15	1259.93	11299.28	135.63	103572.82	n.d	n.d	10.14	n.d	340.70	n.d
	n.d	98.61	1232.25	678.07	39.46	237105.99	1149.71	10252.57	b.d.l.	93755.52	n.d	n.d	b.d.l.	n.d	94.38	n.d
	n.d	99.70	1065.78	582.49	82.01	229648.23	998.19	8726.91	b.d.l.	79057.58	n.d	n.d	b.d.l.	n.d	83.11	n.d
	n.d	46.70	1552.05	914.65	109.39	227967.47	1351.12	13435.93	4.75	122030.95	n.d	n.d	b.d.l.	n.d	55.29	n.d
	n.d	46.99	1380.29	783.89	313.04	233353.01	1212.82	11782.13	8.36	107778.82	n.d	n.d	b.d.l.	n.d	74.54	n.d
	n.d	69.79	1482.50	837.37	612.14	223309.23	1300.04	12454.44	b.d.l.	111856.13	n.d	n.d	b.d.l.	n.d	42.33	n.d
	n.d	135.76	1167.42	608.30	733.06	226656.50	1092.33	9188.08	7.96	81853.40	n.d	n.d	10.62	n.d	169.50	n.d
	n.d	57.36	1411.65	745.91	54.44	220967.03	1237.85	12939.71	7.33	94504.93	n.d	n.d	b.d.l.	n.d	50.65	n.d
	n.d	91.96	1090.41	514.21	1257.56	220706.90	1110.03	9514.30	3148.47	178697.62	n.d	n.d	275.62	n.d	26312.98	n.d
	n.d	51.81	1397.50	771.36	66.10	230538.98	1199.18	12060.40	4.88	102782.48	n.d	n.d	b.d.l.	n.d	49.34	n.d
	n.d	70.69	1353.28	750.13	35.57	226581.15	1201.12	11536.56	2.42	98793.82	n.d	n.d	9.37	n.d	88.09	n.d
	n.d	43.97	1460.35	770.45	211.81	226397.65	1285.82	13688.69	2.42	97338.59	n.d	n.d	b.d.l.	n.d	54.51	n.d
	n.d	36.52	1398.65	767.28	93.84	220743.52	1199.42	12121.85	62.44	98641.35	n.d	n.d	10.09	n.d	133.16	n.d
	n.d	39.59	1546.42	862.26	133.23	222941.69	1303.15	13020.65	94.66	111822.34	n.d	n.d	23.22	n.d	471.28	n.d
	n.d	48.01	1348.79	752.69	212.55	224669.67	1181.47	11615.39	62.13	97074.13	n.d	n.d	17.12	n.d	348.21	n.d
	n.d	40.47	1645.86	945.91	29.01	230870.32	1433.20	14532.68	3.65	124812.48	n.d	n.d	b.d.l.	n.d	33.47	n.d
	n.d	42.67	1592.47	731.31	366.79	229499.06	1142.80	11226.80	69.34	95810.98	n.d	n.d	14.52	n.d	308.81	n.d
	n.d	49.49	1430.47	811.99	51.61	219702.67	1227.53	12095.60	16.56	102996.73	n.d	n.d	12.87	n.d	187.52	n.d
	n.d	87.93	1105.95	592.19	130.50	224669.67	1071.37	9254.70	420.35	78345.89	n.d	n.d	22.86	n.d	930.90	n.d
	n.d	48.54	1679.59	979.85	50.32	224669.67	1459.22	14886.41	b.d.l.	125029.19	n.d	n.d	b.d.l.	n.d	35.35	n.d
	n.d	b.d.l.	1743.75	1022.89	19.76	224669.67	1501.84	15346.12	b.d.l.	131042.49	n.d	n.d	10.61	n.d	11.07	n.d
	n.d	54.12	1122.18	583.47	533.12	224669.67	1021.50	9224.26	48.71	76790.66	n.d	n.d	b.d.l.	n.d	191.32	n.d
M2.6r	n.d	46.84	1128.48	657.96	166.75	245838.42	1114.32	9358.21	253.77	100619.47	n.d	n.d	13.44	n.d	446.17	n.d
	n.d	116.20	1369.76	797.76	34.84	251381.93	1279.85	11031.81	217.80	120820.93	n.d	n.d	19.77	39.97	312.16	5.57
	n.d	46.12	1223.74	703.97	92.95	259710.06	1142.64	10103.69	1300.95	107864.79	n.d	n.d	25.65	n.d	547.66	n.d
	n.d	45.91	1105.70	615.66	362.17	262689.94	1078.97	8796.54	1422.74	96436.23	n.d	n.d	47.30	n.d	1181.32	n.d
	n.d	55.10	1012.83	561.95	337.47	260329.89	1024.11	8166.79	861.61	85472.17	n.d	n.d	52.50	n.d	921.48	n.d
	n.d	51.57	1040.32	589.99	210.82	254581.78	1031.96	8633.77	882.48	90214.97	n.d	n.d	24.08	n.d	733.75	n.d
	n.d	47.68	1141.08	655.20	162.90	257436.04	1112.16	9331.71	265.44	96464.90	n.d	n.d	16.24	n.d	467.27	n.d
	n.d	42.01	1155.49	680.16	111.10	249336.84	1117.30	9803.60	158.97	99347.78	n.d	n.d	11.54	n.d	417.21	n.d
	n.d	42.59	1142.91	664.13	64.35	239968.84	1054.81	9573.09	342.49	95434.23	n.d	n.d	15.01	27.30	409.41	12.31
	n.d	33.67	911.01	488.56	122.86	229323.62	855.01	7276.31	600.71	72129.03	n.d	n.d	24.24	135.96	837.70	26.18
	n.d	b.d.l.	1289.82	749.78	31.35	221168.55	1147.77	10900.60	302.96	108836.49	n.d	n.d	19.30	6.43	302.00	17.44
	n.d	74.34	1507.26	877.82	39.97	231543.09	1370.80	12398.04	135.97	127305.55	n.d	n.d	10.61	n.d	156.99	1.55
	n.d	49.89	1734.33	993.24	45.19	244103.35	1568.82	15482.76	56.17	138481.25	n.d	n.d	b.d.l.	n.d	93.73	n.d
	n.d	28.74	1525.41	787.02	40.26	262285.41	1386.90	14066.58	165.26	104581.77	n.d	n.d	18.10	n.d	351.29	8.76
	169.78	235.39	55383.82	225.80	5678.01	251543.06	1003.03	43711.26	179.31	40550.65	324.50	191.38	242.22	90.67	159.79	9.82
	205.33	255.14	52877.61	232.67	5459.03	240888.57	1009.10	44750.59	199.43	39911.55	193.47	153.77	248.98	87.04	157.13	11.20
	179.86	142.33	38980.85	204.05	4524.45	231941.04	946.44	42847.71	171.26	33431.69	n.d	157.04	196.37	86.82	145.85	8.45
	n.d	b.d.l.	1673.34	985.78	12.69	214489.13	1387.88	15204.73	b.d.l.	118768.50	n.d	n.d	b.d.l.	n.d	2.12	n.d
	n.d	b.d.l.	1395.01	794.77	65.41	214816.60	1192.14	12789.46	b.d.l.	97114.86	n.d	n.d	b.d.l.	n.d	10.83	n.d
	n.d	b.d.l.	1403.65	774.98	54.02	212898.44	1153.83	12083.92	b.d.l.	92324.89	n.d	n.d	b.d.l.	n.d	18.82	n.d
	n.d	b.d.l.	1567.93	890.33	80.54	210415.94	1304.74	14183.18	6.85	106592.09	n.d	n.d	b.d.l.	n.d	22.05	n.d
	n.d	b.d.l.	1659.78	953.70	31.86	209983.12	1395.12	15091.16	2.20	114416.12	n.d	n.d	b.d.l.	n.d	7.97	n.d
	n.d	b.d.l.	1543.33	827.83	79.94	209712.08	1279.70	13444.94	2.70	101147.45	n.d	n.d	b.d.l.	n.d	14.62	n.d
	n.d	b.d.l.	1451.51	826.79	31.04	209802.26	1209.26	13342.54	b.d.l.	99641.46	n.d	n.d	b.d.l.	n.d	6.87	n.d
	n.d	b.d.l.	1540.91	884.42	114.09	206401.54	1293.88	14109.73	4.25	106667.58	n.d	n.d	b.d.l.	n.d	10.61	n.d
	n.d	b.d.l.	1669.30	970.40	37.60	211607.31	1386.68	15386.99	2.34	116426.10	n.d	n.d	b.d.l.	n.d	3.57	n.d
	n.d	b.d.l.	1501.18	841.95	58.58	210727.60	1224.41	13609.74	2.38	99300.90	n.d	n.d	b.d.l.	n.d	18.17	n.d
	n.d	b.d.l.	1638.94	935.76	19.78	210142.12	1368.70	15052.75	b.d.l.	111542.50	n.d	n.d	b.d.l.	n.d	7.25	n.d
	n.d	b.d.l.	1381.88	765.79	145.87	214253.97	1122.51	12443.42	b.d.l.	92448.34	n.d	n.d	b.d.l.	n.d	11.23	n.d
	n.d	b.d.l.	1709.04	1006.78	120.03	210264.84	1454.26	16253.30	5.06	116978.57	n.d	n.d	b.d.l.	n.d	2.71	n.d
	n.d	b.d.l.	1495.51	860.24	181.83	210727.60	1234.64	14144.38	3.10	100983.55	n.d	n.d	b.d.l.	n.d	12.83	n.d
	n.d	b.d.l.	1431.21	804.19	4120.08	210727.60	1220.20	13408.72	2.95	93874.41	n.d	b.d.l.	b.d.l.	n.d	10.23	n.d
	n.d	b.d.l.	1620.47	869.28	265.02	210727.60	1340.49	15699.32	17.63	101328.84	n.d	n.d	b.d.l.	n.d	27.95	n.d
	n.d	b.d.l.	1263.96	653.02	811.06	210727.60	1112.68	12551.22	b.d.l.	76088.97	n.d	n.d	b.d.l.	n.d	15.20	n.d